Simulation and Measurement of Optical Background in the Deep Sea Using a Multi-PMT Optical Module

Simulation und Messung des optischen Untergrunds im Meer mit einem Multi-PMT-Modul

Der Naturwissenschaftlichen Fakultät
der Friedrich-Alexander-Universität Erlangen-Nürnberg
zur Erlangung des Doktorgrades
Dr. rer. nat.

vorgelegt von
Björn Herold

aus Nürnberg

Als Dissertation genehmigt von der Naturwissenschaftlichen Fakultät
der Friedrich-Alexander-Universität Erlangen-Nürnberg

Tag der mündlichen Prüfung:	13.10.2017
Vorsitzender der Promotionsorgans:	Prof. Dr. Georg Kreimer
Gutachter/in:	Prof. Dr. Ulrich F. Katz Prof. Dr. Gisela Anton

Contents

Kapitel 0

Zusammenfassung

0.1 Neutrinoteleskope

Neutrinoteleskope sind Teilchendetektoren, die Neutrinos außerirdischen Ursprungs messen sollen. Zu diesem Zweck müssen sie die Herkunftsrichtung und die kinetische Energie der registrierten Neutrinos ermitteln können.
Neutrinos entstehen, wenn Protonen oder Atomkerne mit Photonen oder Materie wechselwirken. Mögliche Quellen könnten Supernovaüberreste, aktive galaktische Kerne, oder der GZK-Effekt sein. Neutrinos haben eine geringe Wahrscheinlichkeit, mit Materie zu reagieren und legen daher ungehindert große Strecken zurück. Bei einer Wechselwirkung werden sie meistens zerstört (d.h. in ein anderes Teilchen umgewandelt). Das bedeutet, dass Neutrinos, die die Erde erreichen, auch tatsächlich aus der Richtung ihres Entstehungsortes ankommen. Wenn die kinetische Energie eines Neutrinos groß genug ist und es nah genug beim Detektor wechselwirkt, kann es registriert und seine Herkunftsrichtung ermittelt werden. Die Energie des Neutrinos kann ebenfalls abgeschätzt werden.
Registrierte Neutrinos kann man als Punkte auf einer Himmelskarte darstellen. Diese ist eine Projektion der Himmelskugel auf eine Karte, so dass jeder möglichen Blickrichtung ein Punkt auf der Karte zugeordnet ist. Nach einer ausreichend langen Messzeit erhalten die Experimentatoren (hoffentlich) eine Himmelskarte, in der Neutrinoquellen durch Anhäufungen von Neutrinos, die aus nahezu der gleichen Richtung ankamen, erkennbar sind. Außerdem erhält man ein Energiespektrum für die gemessenen Neutrinos, das man mit theoretischen Vorhersagen vergleichen kann.

Aufgrund der Messmethode müssen Neutrinoteleskope in ein transparentes Medium wie Wasser oder Eis gebaut werden. Diese müssen, wegen der geringen Wechselwirkungswahrscheinlichkeit (Wirkungsquerschnitt) von Neutrinos, ein sehr großes instrumentiertes Volumen aufweisen, wodurch man auf natürliche Gewässer oder Eisvorkommen angewiesen ist. Im Neutrinoteleskop muss es dunkel sein, also muss man tief genug im Meer oder Eis bauen, damit Tageslicht nicht hinunterreicht. Und außerdem ist es notwendig, den Detektor vor natürlicher Radioaktivität und vor kosmischer Strahlung zu schützen, was eine noch größere Tiefe erfordert, als nur die For-

derung nach Dunkelheit. Zusätzliche Teilchendetektoren als Veto gegen kosmische Strahlung haben sich ebenfalls bewährt.

In dieser Zusammenfassung werde ich mich auf auf Tiefsee-Neutrinoteleskope beschränken, da ich in meiner Forschungszeit Mitglied der ANTARES-Kollaboration war, welche seit 2006 das weltweit erste Tiefsee-Neutrinoteleskop betreibt, und der KM3NeT-Kollaboration, welche den Nachfolger entwickelte und derzeit baut.

Tiefsee-Neutrinoteleskope sind im Wesentlichen ein auf dem Meeresgrund platziertes dreidimensionales Gitter hochempfindlicher optischer Sensoren. Dies erreicht man durch verankerte Kabel, die mit Bojen straff gehalten werden. Diese Kabel, in ANTARES/KM3NeT „line“ oder „detection unit“ (DU) genannt, sind mehrere hundert Meter hoch. Der Abstand zwischen den lines beträgt in ANTARES etwa 60 m, in KM3NeT wird er bei mehr als 100 m liegen.
An den Kabeln sind ab einer gewissen Mindesthöhe in regelmäßigen Abständen die Sensoren in Form von „optischen Modulen“ (OM) angebracht, die somit die Stockwerke (floor oder storey) des Detektors bilden. Die optischen Module bestehen aus Photomultipliern (PMT, Sensoren, die einzelne Photonen registrieren können) in einer druckfesten Glaskugel. Die zugehörige Hilfselektronik kann mit in der Kugel oder in einem eigenen Gehäuse untergebracht sein.

Wenn ein hochenergetisches Neutrino in der Nähe oder auch innerhalb des Neutrinoteleskops mit Materie wechselwirkt, entsteht ein geladenes Lepton (Elektron/Positron, Myon oder Tauon), das sich mit relativistischer Geschwindigkeit bewegt. Die Wechselwirkung kann auch am Entstehungsort eine elektromagnetischen Kaskade erzeugen. Dies alles führt zur Emission von Cherenkov-Licht am Wechselwirkungspunkt und/oder entlang der Flugbahn des Leptons. Die optischen Module registrieren dieses Licht, und anhand der Zeitunterschiede, wann das Licht an verschiedenen Stellen im Detektor gemessen wird, lässt sich die Position und/oder die Flugbahn der Lichtquelle berechnen („rekonstruieren“). Damit das klappt, muss die Datennahme die Zeit auf die Nanosekunde genau messen.

Neben dem gewünschten Licht aus Neutrinowechselwirkungen gibt es wesentlich mehr Untergrundlicht aus verschiedenen Quellen, selbst in der dunkelsten Tiefe des Meeres. Die hervorstechendste und variabelste Störlichtquelle ist die Biolumineszenz. Verschiedene Mikro- und Makroorganismen in der Tiefsee strahlen Licht aus. Je nach Umweltbedingungen und Jahreszeit variiert dieses: Von einem vergleichsweise geringen Untergrund aus einzelnen registrierten Photonen, der leicht herausgefiltert werden kann, bis hin zu verrückt springenden Photonenzählraten, die auch mal so hoch sein können, dass der Detektor zum Schutz der Photomultiplier heruntergefahren werden muss.
Ein vorhersehbarer und konstanter Untergrundanteil kommt vom Zerfall von langlebigen radioaktiven Isotopen der im Meerwasser gelösten Salze. Der wichtigste davon ist der β-Zerfall von ^{40}K mit einer Aktivität von etwa 13 Bq pro Liter. Die dabei emittierten Elektronen besitzen eine maximale kinetische Energie von 1,3 MeV, was deutlich über der Schwelle für die Emission von Cherenkov-Licht liegt.
Eine weitere Quelle von Cherenkov-Licht sind atmosphärische Myonen, die leicht mehrere Kilo-

meter tief in die Erde oder das Meer eindringen können. Diese Myonen hinterlassen im Prinzip die gleiche Spur im Detektor wie ein Myonneutrino, das in der Nähe wechselgewirkt hat. Dadurch kann man sie gut nutzen, um den Detektor zu kalibrieren und Rekonstruktionstechniken weiterzuentwickeln.
Das den PMTs innewohnende Rauschen ist weniger problematisch, da es sich aufgrund der Einzelphotoncharakteristik auch wieder leicht herausfiltern lässt, und weil die Photomultiplier auf geringes Eigenrauschen hin entwickelt und getestet wurden.

Das bestehende Neutrinoteleskop ANTARES, welches etwa 40 km südlich von Toulon in 2,4 km Tiefe liegt, benutzt optische Module mit einem einzelnen großen PMT. Jedes Stockwerk besitzt drei Module, die um einen Zylinder mit der Steuerelektronik angeordnet sind. Für KM3NeT wurde ein neues, schlankeres Design entwickelt. Jedes Stockwerk besteht nur noch aus einem OM, in dem auch die gesamte Elektronik untergebracht ist. Das Modul hat 31 kleine PMTs in einer Glaskugel mit einem Durchmesser von etwa 43 cm. Dieses Multi-PMT Modul hat mehrere Vorteile: Die sensitive Oberfläche ist mehr als doppelt so groß wie beim Vorgänger, und durch die Unterteilung ergeben sich neue Möglichkeiten für die Untergrundunterdrückung und die Rekonstruktion von Teilchenspuren und Punktlichtquellen.

0.2 Ziele meiner Arbeit

Simulation

Am Anfang meiner Arbeit stand ein Simulationsprojekt, das die Signatur von ^{40}K-Untergrund im neuen OM-Typ ermitteln sollte. Die durch ^{40}K-Zerfälle induzierte Einzelphotonrate in jedem PMT ließe sich noch berechnen. Interessanter und für den Betrieb des künftigen Neutrinoteleskops wichtiger sind die Korrelationen zwischen Photonen, die aus dem gleichen Zerfall stammen. Bei einem ^{40}K-Zerfall in der Nähe eines OM ist es sehr wahrscheinlich, dass mehrere Photonen (fast) gleichzeitig ankommen und in mehreren PMT registriert werden. Wenn diese Koinzidenzen einem typischen Muster folgen, eignen sie sich vielleicht zur Untergrundunterdrückung und Eichung des Detektors im Betrieb.

Um diese Informationen zu gewinnen, erstellte ich erst ein vereinfachtes, später ein sehr detailliertes Computermodell des optischen Moduls. Hierfür nutzte ich das Softwarepaket GEANT 4, mit dem sich teilchenphysikalische Simulationen programmieren lassen. Alle verfügbaren Daten über die optischen Eigenschaften von Meerwasser (unter anderem aus Messungen bei ANTARES) und von den verwendeten Baumaterialien im OM (Glas, Kontaktgel) wurden in die Simulation übernommen.
Je nach Simulationseinstellung war es möglich, die gesamte, durch ^{40}K erzeugte, Hintergrundrate zu simulieren, oder die Signatur von nahen Zerfällen genauer zu untersuchen.
Eine Variante meiner Software diente der genauen Untersuchung der zu erwartenden Empfindlichkeit des fertigen optischen Moduls.

Datennahme und -analyse

Im April 2013 wurde das erste Vorserienmodell des „Multi-PMT digital optical module“ (PPM-DOM) in ANTARES integriert. Es befindet sich auf der „Instrumentation Line“, die hauptsächlich Sensoren zur Untersuchung der Meeresbedingungen trägt.
Bis Oktober war ich Teil der kleinen Gruppe, die das PPMDOM in Betrieb hielt, damit die ersten Messungen durchführte und die umfangreiche Datenanalyse in Angriff nahm. Meine Hauptziele waren dabei die Entwicklung eines Schemas für die interne Zeitkalibration, wobei fast automatisch ein Vergleich meiner Simulationsprognosen mit echten Daten stattfand. Außerdem wagte ich mich an daran, die Unterteilung der Sensorfläche zu nutzen, um die Herkunftsrichtung eines Lichtblitzes abzuschätzen.

0.3 Simulationsergebnisse

Schließlich ergaben die Simulationen zwei Datensätze. Einer der Datensätze enthält Messergebnisse für die Endfassung des optischen Moduls, so dass die gewonnenen Informationen in anderen Simulationen, welche die Empfindlichkeit des gesamten Detektors untersuchen, verwendet werden können. Der andere Datensatz bezieht sich speziell auf das Vorserienmodell, um die Zuverlässigkeit meiner Prognose am echten Objekt messen zu können.

Zählraten

Die erwartete Einzelphoton-Hintergrundzählrate durch ^{40}K-Zerfälle liegt bei 128 kHz für die Endfassung des OM, also etwa 4,1 kHz pro PMT. Im PPMDOM mit der etwas kleineren Sensorfläche erwartet man insgesamt 97 kHz, also 3,1 kHz pro PMT.

Treffermuster und Koinzidenzraten

Aus den Simulationsdaten lassen sich die Koinzidenzraten für jedes PMT-Paar leicht gewinnen. Kurz gefasst ist die Anzahl an Koinzidenzen durch nahe ^{40}K-Zerfälle zwischen zwei PMT umso höher, je näher diese im OM beieinander liegen.
Da das Elektron aus dem β-Zerfall nur eine kurze Strecke im Wasser zurücklegt, kommen alle Photonen, die durch einen nahen Zerfall erzeugt werden, vom gleichen Ort. Aufgrund der Maße des Moduls ist auch klar, dass die Photonen fast gleichzeitig ankommen, weniger als 1 ns getrennt. Der häufigste Koinzidenzfall besteht aus zwei einzelnen Photonen, die in zwei direkt benachbarten PMT registriert werden. Je weiter das PMT-Paar auseinander liegt, desto weniger Koinzidenzen werden gemessen. Koinzidenzen mit drei oder mehr PMTs sind mindestens um den Faktor 10 weniger wahrscheinlich und wurden in der Analyse wie Zweifach-Koinzidenzen behandelt, wobei die zuerst getroffenen PMTs das „Paar“ festlegten.
Für die Endfassung des OM erwarte ich eine Koinzidenzrate von etwa 564 Hz aus nahen Zerfällen, deren Signatur sich für die Kalibrierung eignet. Im Vorserienmodell sollte die Rate ca. 347 Hz betragen.

Empfindlichkeit der optischen Module

Aufgrund der genauen Modellierung eignete sich meine Simulation zur Vorhersage der Empfindlichkeit jedes PMT im OM abhängig von der Einfallsrichtung des Lichts. Diese Daten waren für meine Richtungsbestimmung notwendig.

0.4 Messergebnisse

Zählraten

Die im Meer gemessene Einzelphotonrate enthält neben den ^{40}K-Treffern das interne Rauschen der PMT und den Einfluss durch Biolumineszenz, so dass die Gesamtrate zwischen 240 kHz an einem ruhigen Tag und über einem MHz bei schlechten Meeresbedingungen liegt. Es ist daher nicht möglich, die ^{40}K-Einzelphotonrate zu ermitteln.

Treffermuster und Koinzidenzraten

Das PPMDOM hatte keine vollständige Zeitsynchronisation, weshalb jeder PMT einen bestimmten, festen Zeitversatz zur Referenzuhr hatte. Zwischen zwei PMTs lag dieser Versatz bei bis zu 15 ns, was für viele Messungen bereits länger ist als das erwünschte Koinzidenzfenster. Nutzt man aber die Kenntnis, dass ^{40}K-Photonen zeitgleich ankommen, lässt sich der relative Zeitversatz zwischen je zwei PMT ermitteln. Indem man dies der Reihe nach auf alle benachbarten PMT anwendet, erhält man für alle PMT eine Zeitkorrektur. Dabei lässt sich auch die ^{40}K-Koinzidenzrate ermitteln.
Die Zeitkalibration wurde nur mit Daten durchgeführt, die zwischen April und Oktober 2013 bei guten Meeresbedingungen genommen worden waren. Diese wurden gesammelt und in Summe analysiert. Daraus ergab sich eine Koinzidenzrate, erzeugt durch nahe ^{40}K-Zerfälle, von 353 Hz, welche sehr gut mit meiner Vorhersage von 347 Hz übereinstimmt. Ebenso ließ sich die Verteilung der Koinzidenzen auf die PMT-Paare darstellen und mit der Vorhersage vergleichen. Auch hier war die Übereinstimmung sehr gut, so dass ich die Qualität meines Simulationsmodells bestätigt sah und mich der letzten Analyse zuwandte.

Richtungsbestimmung

Mithilfe der aus der Simulation bekannten richtungsabhängigen Empfindlichkeit jedes PMTs entwickelte ich einen Algorithmus, der die Herkunftsrichtung eines Lichtblitzes abschätzt. Wenn eine ausreichende Zahl an Photonen (idealerweise mehr Photonen als bei Zufallskoinzidenzen) innerhalb weniger Nanosekunden eintrifft, lässt sich anhand der getroffenen PMT eine Wahrscheinlichkeitsverteilung für die möglichen Herkunftsrichtungen berechnen. Diese Methode sollte gut bei kurzen Lichtblitzen, wie z.B. dem Cherenkov-Kegel eines Myons, funktionieren.

Aus Zeitgründen konnte ich die Richtungsbestimmung nur sehr kurz entwickeln und testen. Mit Hilfe der ANTARES-Kalibrierungsblitzer konnte ich zeigen, dass es auch mit der Hardware des

Vorserienmodell schon möglich ist, die ungefähre Richtung einer Lichtquelle zu ermitteln. Falls es mit den Serienmodellen möglich ist, die Anzahl der auftreffenden Photonen in einem PMT zu messen, könnte die Richtungsbestimmung noch deutlich verbessert werden. Auf jeden Fall kann sie für die klassischen Spurrekonstruktionsalgorithmen sinnvolle Startwerte liefern, wodurch die Geschwindigkeit und Qualität jener Analysen gesteigert werden kann.

Chapter 1

Introduction

1.1 Neutrino Astronomy

One hundred years ago Victor Hess' discovery of charged cosmic rays started the field now known as astroparticle physics. However, the charged cosmic radiation Hess and others detected is merely the tip of the iceberg.

Apart from protons and heavier nuclei of varying origin, earth's atmosphere is continuously bombarded by high energy electromagnetic radiation. Both of these types lend themselves to detection using various methods, thanks to their large cross sections. But there is another, more elusive and potentially more informative particle that not only bombards, but also penetrates the earth in huge numbers.

With its small cross section, the neutrino is utterly unimpressed by obstacles like dust clouds or the dense parts of its sources. Thanks to its neutrality, no electromagnetic field forces it off course. Thus it tells us exactly where it came from, and promises a look deep into the heart of its source.

Of course, the downside of this is that neutrinos are notoriously hard to detect. We can only see them indirectly, via charged particles created in the rare neutrino interactions. Therefore, creativity, large detection volumes, and ingenuity are required to catch these bastards. Neutrino telescopes, pioneered as early as the late 1970s, are basically a three-dimensional grid of optical sensors (usually photomultiplier tubes, PMTs). They detect light emitted by the products of neutrino reactions in transparent media like water or ice.

ANTARES in the Mediterranean Sea and ICECUBE at the South Pole are the largest neutrino telescopes currently in continuous operation. They span volumes of 0.03 and 1 km^3 respectively. Both have been running for several years and amassed an impressive amount of data.

1.2 Go Big or Go Home

Experience has shown that even the huge IceCube detector is not yet large enough to detect the sources of galactic or cosmic neutrinos, even though growing evidence for neutrinos of extraterrestrial origin has been reported by the IceCube collaboration in several papers (e.g. [24], [25] and [26]).

The KM3NeT collaboration therefore strives to add to the existing global efforts in neutrino astronomy by building a neutrino telescope with an instrumented volume of several cubic kilometres at the bottom of the Mediterranean, making it the largest and most sensitive one in the world. A lot of research has been dedicated to finding the best technical solutions using both proven and newly developed technology, and extensive simulation work was employed to find the most sensitive detector configuration, and to test new detector solutions.

1.3 Contents of this Thesis

The work presented here is about the computer simulation of a new type of optical module which has been developed for the KM3NeT detector currently under construction.

I have modeled this sensor and predicted its sensitivity and typical response to background light and other signals. The results of these simulations went into large-scale detector simulations performed by the KM3NeT collaboration. I also compare my simulation results to first data from a prototype optical module deployed within the Antares neutrino telescope in 2013. The predictions derived from the simulation are used for an in-situ calibration of the module.

Chapter 2

The Physics of Neutrino Telescopes

The following chapter will outline the most important physical background and technical aspects needed to understand how a neutrino telescope works.

2.1 Charged Leptons

A neutrino telescope can detect neutrinos only indirectly by observing the secondary particles released in neutrino interactions. The neutrinos that are useful for the purposes of neutrino astronomy have kinetic energies sufficient to create highly relativistic charged leptons, which can be detected relatively easily. Charged leptons can interact weakly and electromagnetically.

In the Standard Model of particle physics, charged leptons belong to one of the three particle families:
Electrons and positrons (e^- and e^+) form the first family (or generation) with the up and down (anti)quarks. The rest mass of an electron is 511 keV.
Muons and antimuons (μ^- and μ^+) form a family with the charm and strange quarks and antiquarks. Muons have a rest mass of 105.7 MeV. Their mean lifetime is 2.2 µs. They can decay to an electron and two neutrinos.
The third family comprises tauons (τ^- and τ^+) and the top and bottom (anti)quarks. The tauon's rest mass is 1777 MeV. It has a very short lifetime (2.9×10^{-13} s) and numerous decay channels, among them the decay to a lighter lepton plus two neutrinos.

2.2 Neutrinos

Neutrinos were first postulated by Wolfgang Pauli in 1930 to explain the continuous energy spectrum of the electrons emitted in β decays. They are the uncharged partners of the charged leptons, electrons, muons and tauons ($e^{+/-}$, $\mu^{+/-}$, $\tau^{+/-}$), and are named after these. The first direct measurement of electron antineutrinos was achieved in 1956 by Cowan and Reines [35].

Neutrinos accompany nuclear or subatomic reactions where charged leptons are created or destroyed to account for lepton number conservation. Example reactions are the β decay

$$n \rightarrow p + e^- + \overline{\nu}_e$$

or the reactions of hadronic cosmic radiation (usually protons) with nuclei of the atmosphere, which generates atmospheric muons and neutrinos (after [37]):

$$\begin{aligned} p + \text{nucleus} \quad &\rightarrow \quad \pi^{+/-/0} + X \\ &\qquad \pi^{+/-} \rightarrow \mu^{+/-} + \nu_\mu/\overline{\nu}_\mu \end{aligned}$$

Neutral pions decay to two gamma photons and are of no interest to neutrino astronomers. The muon (antimuon) may subsequently decay into an electron (positron), a muon (anti)neutrino and an electron antineutrino (neutrino):

$$\begin{aligned} \mu^- &\rightarrow e^- + \overline{\nu}_e + \nu_\mu \\ \mu^+ &\rightarrow e^+ + \nu_e + \overline{\nu}_\mu \end{aligned}$$

Originally introduced into the Standard Model as massless particles, the solar neutrino problem and its resolution led to the finding that neutrinos do have a very small mass (of less than 2 eV [36]), which is necessary for them to be able to oscillate between the three flavours. Numerous experiments have worked and are still working on determining the exact masses of the three neutrino flavours.
As uncharged leptons, neutrinos can only interact via the weak interaction. Therefore their cross section is small, requiring large detectors and long exposition. Neutrinos can interact by exchanging a neutral Z vector boson (neutral current interaction), which will keep the neutrino but transfer momentum to the interaction partner, or by exchanging a $W^\pm$ boson (charged current interaction), which will change the neutrino to a charged lepton of the same family.

2.3 Cherenkov Radiation

If a charged particle travelling through a (transparent) medium moves faster than the local phase velocity of light, it causes the emission of photons along its trajectory. This is called Cherenkov effect or Cherenkov radiation.
A common example of this is the blue glow associated with nuclear fuel rods submerged in water. Cherenkov radiation is an important effect for particle detection in many experiments.

2.3.1 Cherenkov Cone

The emission occurs at an angle θ to the direction of travel which satisfies the condition

$$\cos\theta = \frac{1}{n\beta} \quad , \tag{2.1}$$

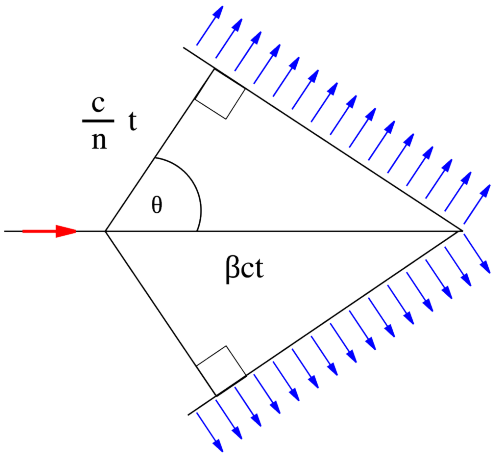

Figure 2.1: Illustration of the emission direction of Cherenkov photons with respect to the direction of motion of the charged particle causing the emission.
Image created by Arpad Horvath [3].

where n is the index of refraction of the surrounding medium, and β is the fraction of the (vacuum) speed of light at which the particle is moving: $\beta = \frac{v}{c}$. The emission of Cherenkov light happens in a rotationally symmetric way, thus creating a cone of light expanding along and around the path of the "speeding" particle.
One can see that at particle speeds below $\frac{c}{n}$ the result of the cosine function would be greater than one and therefore no valid angle can be calculated, whereas at speeds above the Cherenkov threshold an emission direction, and therefore the opening angle of the Cherenkov cone, can be calculated.

2.3.2 Photon Energy Spectrum

The photon spectrum, that is, the number of emitted photons per wavelength interval, can by derived from a formula formulated by Ilya M. Frank and Igor Y. Tamm in 1937. The Tamm-Frank formula [4] describes the energy $\mathrm{d}E$ emitted via Cherenkov radiation per distance $\mathrm{d}x$ that the "emitting" particle of charge e travels through the medium as a function of the photon frequency ω:

$$\frac{\mathrm{d}E}{\mathrm{d}x} = \frac{e^2}{c^2} \int \left(1 - \frac{1}{\beta^2 n^2}\right) \omega \mathrm{d}\omega \tag{2.2}$$

This can easily be reshaped to

$$\frac{\mathrm{d}^2 N}{\mathrm{d}x \mathrm{d}\lambda} = 2\pi\alpha \left(1 - \frac{1}{\beta^2 n^2}\right) \frac{1}{\lambda^2} \tag{2.3}$$

where α is the fine structure constant. For a detailed derivation, see appendix B.1.

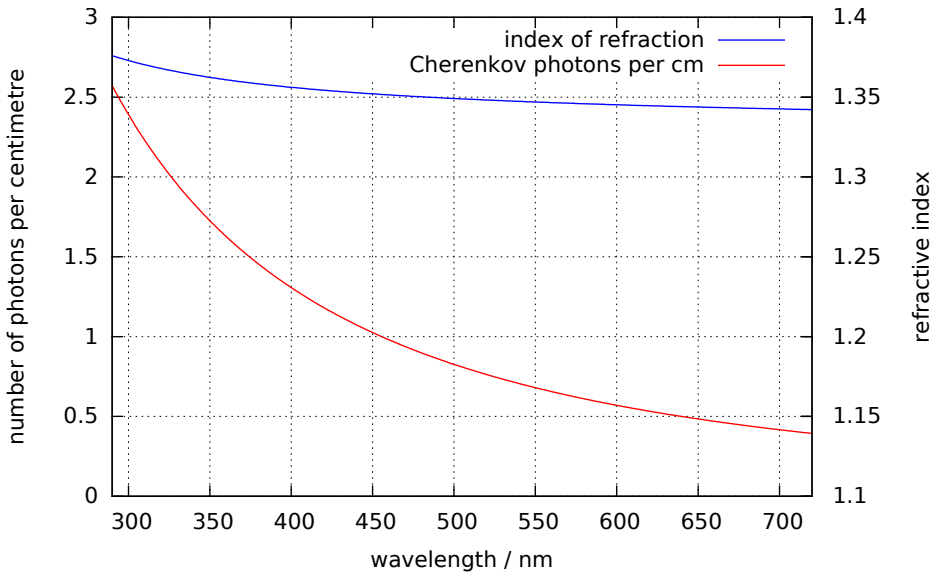

Figure 2.2: Example Cherenkov spectrum of a particle with one elementary charge travelling through sea water at a constant speed of 0.9999 c. The abscissa reads the number of photons emitted per centimetre travelled within a wavelength interval of one nanometre. 432 photons are emitted within the wavelength interval of 290 – 720 nm along a distance of 1 cm.

Figure 2.2 shows the Cherenkov spectrum of a singly charged particle travelling at a constant velocity of $\beta = 0.9999$. The index of refraction and dispersion correspond to the deep sea. See appendix A.1 for details.

2.3.3 Example from the deep sea

Cherenkov cone opening angle

For optical wavelengths and a depth of 3,500 meters, formula 6 from [5] yields refractive indices ranging from 1.37 at the violet end to 1.34 at the red end of the spectrum. Detailed values can be found in the appendix in table A.1.
A neutrino telescope primarily detects highly relativistic muons that pass through the instrumented volume. With β approaching 1, the cosine of the emission angle will be one over the refractive index. In the spectral range mentioned above, this leads to an angle of about 42°. The Cherenkov cone therefore has an opening angle of 84–85°.

Cherenkov threshold

The kinetic energy threshold above which a particle causes Cherenkov emission is given by the condition

$$\frac{1}{n\beta} \leq 1 \Rightarrow \beta n \geq 1 \Rightarrow \beta \geq \frac{1}{n} \,. \tag{2.4}$$

With the definition that γ is the total energy E of a particle divided by its rest mass E_0, we reach

$$\gamma = \frac{E}{E_0} = \frac{E_0 + E_{kin}}{E_0} = 1 + \frac{E_{kin}}{E_0} . \tag{2.5}$$

We can use this to solve the equation

$$\gamma = \frac{1}{\sqrt{1-\beta^2}} = 1 + \frac{E_{kin}}{E_0} \tag{2.6}$$

for E_{kin} using equation 2.4:

$$E_{kin} = E_0 \left(\frac{1}{\sqrt{1-\frac{1}{n^2}}} - 1 \right) . \tag{2.7}$$

In the case of electrons in a medium with a refractive index of 1.36, this equation yields a Cherenkov threshold of 243 keV.

2.4 ^{40}K

Potassium 40, which in general accounts for a large fraction of the natural background radiation, has a long half-life of about 1.28×10^9 years. It can decay via the β^- decay channel (89 %) to ^{40}Ca, or via various electron capture processes (summing up to about 11 %) and β^+ (10 ppm) to ^{40}Ar. The decay modes are listed in table 2.1.

Potassium is part of many natural salts and minerals. As such it is found virtually everywhere in the environment. It is also a vital electrolyte for the human body. Elementary potassium consists of 0.012 % of the isotope ^{40}K. Due to its ubiquitousness, ^{40}K accounts for a large fraction of the natural background radiation in general. And since it is part of the natural composition of sea water, with a mass percentage of about 0.038 [40], it contributes significantly to the radioactive background in the deep sea. An activity of about 31 Bq per gram of natural potassium [39] leads to an activity of 12 Bq in a litre of sea water.

The β decay modes can create light "directly" via Cherenkov emission. The Cherenkov threshold for an electron or positron in water is about 240 keV. The maximum kinetic energy of the e^- is 1311 keV. The spectrum is shown in figure 2.3.
Electron capture processes lead to the emission of a photon of 1461 keV, which can then produce fast electrons via photoelectric effect or Compton scattering.

The simulation toolkit I used for the simulations described in chapter 5 is GEANT 4 [1]. The toolkit handles the correct implementation of the ^{40}K decay and the reactions of the secondary particles, including the creation of Cherenkov light. A detailed treatise on the ^{40}K-decay in GEANT 4 can be found in [11]. The authors especially discuss a bug in earlier GEANT 4 versions that created a wrong energy spectrum for the β decay. The proposed fix has since been

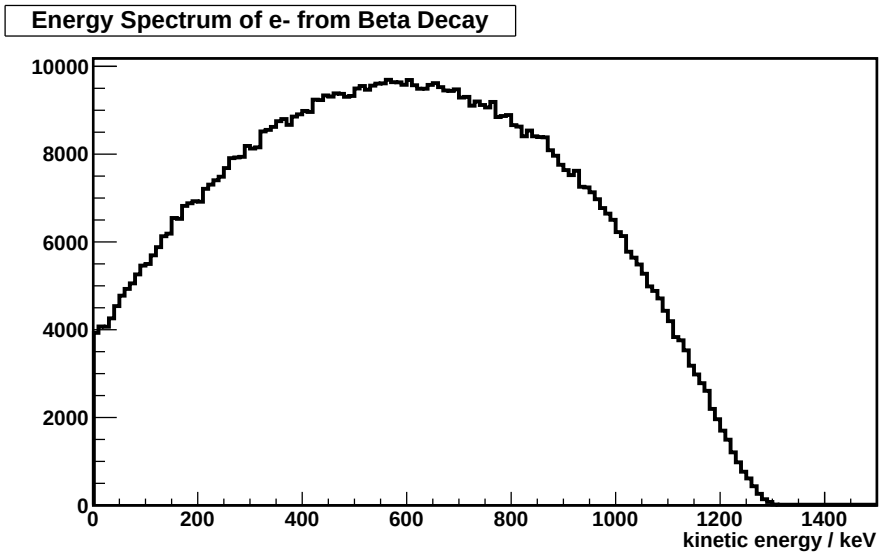

Figure 2.3: Energy spectrum of the β decay of ^{40}K, produced with GEANT 4 based simulation.

included in published versions of GEANT 4.

The branching ratios used in my simulation are shown in table 2.1 and can be found in a human-readable format within the GEANT 4 source code files. GEANT 4 takes its data from the Evaluated Nuclear Structure Data File [2].

Mode	Ratio	Energy	Product
β^-	89.280 %	1.311 MeV	^{40}Ca
ϵ	10.719 %	1.461 MeV	^{40}Ar
β^+	0.001 %	1.505 MeV	^{40}Ar

Table 2.1: Decay modes, branching ratios, (maximum) energy of the emitted secondary particle and resulting daughter product for the radioactive decay of ^{40}K.

2.5 Photomultiplier Tubes

A photomultiplier tube, in short photomultiplier or PMT, is an optical sensor used to detect very low light fluxes down to single photons. Its working principle is the creation of photoelectrons followed by the multiplication of same to a number sufficient to produce a measureable electrical signal. Typically, several 10^6 electrons per primary photoelectron are created.

2.5.1 Construction

A PMT consists of a vacuum tube with an input window which is optically transparent to light of the spectral range to be detected. Behind this window lies the photocathode, which emits electrons via the photoelectric effect. Focussing electrodes direct the emitted photoelectrons to the dynode structure, which acts as an electron multiplier. The anode lies at the end of this chain and receives the electrons emitted by the dynode stages. The internal parts are supported and connected to the outside by solid wire leads protruding from one end of tube.

Photocathode

The photocathode is an alloy of metals and/or semiconductors which emits photoelectrons when illuminated. Constructively, there are two major types of photocathode: Transmission mode photocathodes, which are coated onto the inside of the input window by vapor deposition, or reflection mode photocathodes, which are coated onto a carrier structure inside the tube.
The photocathode lies on the lowest electrical potential of all metallic parts inside the PMT, thus causing photoelectrons to be accelerated toward the dynode structure.

Focussing Electrodes

The focussing electrodes shape the electric field between photocathode and first dynode in a way that maximises the number of photoelectrons that can reach the active area of the first dynode, and minimises the transit time spread of the electrons.

Dynode Structure

The dynodes are electrodes coated with a material that enhances stimulated electron emission. An impinging primary electron with a kinetic energy of around 100 eV will cause the emission of typically four to five secondary electrons. Each dynode is shaped such that the secondary electrons are directed towards the next dynode, where each secondary electron will cause the emission of more electrons. The electrical potential difference between the dynodes is such that each following dynode is at a higher potential, so that the emitted electrons at each dynode are accelerated towards the next one.

Anode

The anode is the final electrode in the multiplier chain. It is shaped such as to gather the maximum number of secondary electrons, and has to withstand the tear and wear of the constant electron bombardment. The anode lies at the highest electrical potential of the PMT parts.

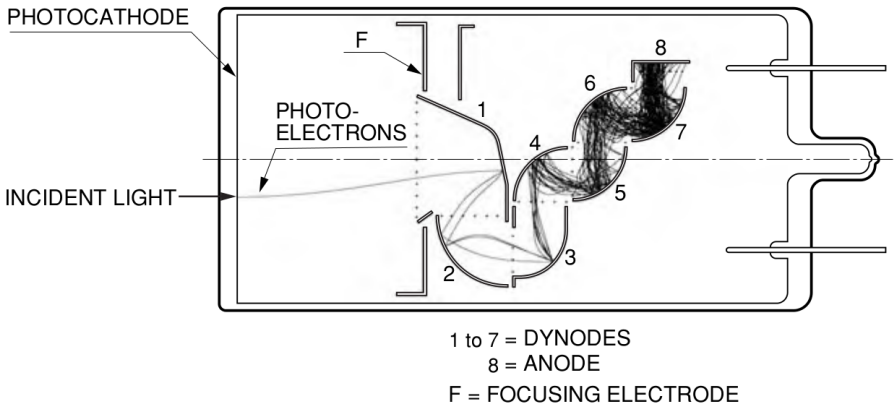

Figure 2.4: Example dynode structure, box and grid type. Adapted from the PMT Handbook [27]

2.5.2 Power Supply

The total potential difference between the photocathode (usually negative potential) and the anode (usually ground potential) typically lies between 1000 and 1500 Volts.

The usual method to provide this voltage is by using a single power supply in connection with a voltage divider, as can be seen in figure 2.5. The voltage divider provides the appropriate voltage staging between the photocathode, focussing electrodes, dynodes and anode. In its most basic form, it is a series of resistors (MΩ range) connected to the HV supply. The advantage of this approach is that it is cheap and simple and that a single high voltage supply can power several PMTs. The disadvantage lies in its power usage, as it is not possible to choose arbitrarily high resistor values. Due to the space charge building up within the dynode structure and the current drawn by emitting millions of electrons within nanoseconds, the accelerating voltage at the latter dynode stages would collapse. Adding some capacitance to the latter stages also helps to reduce the effect of the space charge and to improve the gain of the PMT.

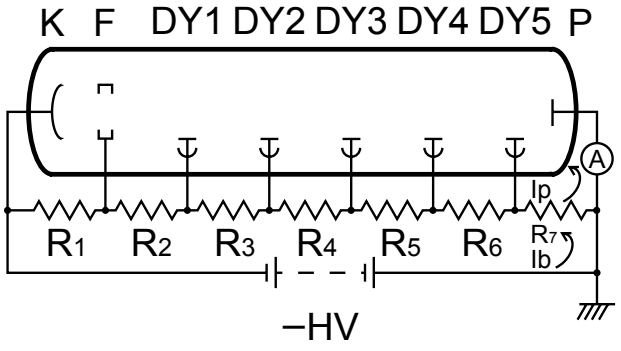

Figure 2.5: Most basic voltage divider circuit. Adapted from the PMT Handbook [27]

A more modern solution has been adopted for KM3NeT in the shape of an active PMT base, which is a compact circuit board soldered directly onto the PMT leads. Cockroft-Walton-circuits on the board provide each contact of the PMT with its own stabilised high voltage. Read-out electronics are integrated on-board. The power consumption and space requirements of this elegant solution are much smaller than those of a voltage-divider base.

2.5.3 Characteristics

Among the most important characteristics describing a PMT are the quantum efficiency, the collection efficiency, the gain, the dark rate, and the transit time spread.

Quantum Efficiency

The quantum efficiency is defined as the number of photoelectrons emitted by the photocathode divided by the number of incident photons, and is usually expressed as a percentage. The quantum efficiency is highly dependent on the photon energy/wavelength. Each photocathode material has its own characteristic efficiency curve. A bialkali photocathode, a type commonly used in experiments that are based on detecting Cherenkov light, has a peak quantum efficiency of around 25 %, with recent developments reaching more than 30 % peak.

Figure 2.6 shows quantum efficiency curves of a batch of PMTs evaluated at ECAP using the test bench developed by O. Kalekin and B. Herold [29]. These PMTs made by Hamamatsu [1] have a high quality bialkali photocathode.

Collection Efficiency

The collection efficiency is the probability that an emitted photoelectron will reach the active area of the first dynode, thus triggering the avalanche which will lead to an electrical signal at the anode. It depends slightly on where and under which angle the incoming photon hit the photocathode, and greatly on the acceleration voltage between the photocathode and the first dynode. Averaged over the complete sensitive area of the PMT, the collection efficiency is typically better than 90 %.
The product of quantum efficiency and collection efficiency is called the detection efficiency of a PMT.

Gain

The gain is the electron multiplication factor, which is the number of electrons reaching the anode per emitted photoelectron. It lies in the range of 10^6 to 10^7. The lower the voltage required to achieve a given gain, the better and more efficient the dynode structure works. Achieving the desired gain within a given voltage range is a selection criterium for KM3NeT

[1] Hamamatsu Photonics, http://www.hamamatsu.com

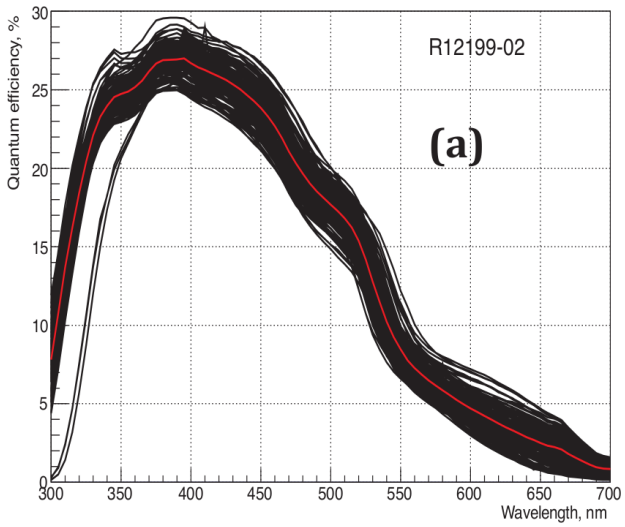

Figure 2.6: Recent results from quantum efficiency measurements of PMTs for KM3NeT. Taken from [22]. Note the two curves cutting off earlier towards short wavelengths: Presumably, these tubes were made from a different type of glass with a cut-off at longer wavelengths.

PMTs.

Due to the statistical nature of the electron multiplication process, the charge reaching the anode for each photoelectron can vary greatly. Therefore, the gain is the average multiplication factor, while the shape and width of the charge distribution is another quality of the PMT.

Transit Time Spread

The time between the creation of the photoelectron and the arrival of the electron cloud at the anode is called the transit time. Depending on where the photoelectron was created, and influenced by the randomness of the electron multiplication, this transit time varies from event to event, and may systematically differ from PMT to PMT. The width of the transit time distribution is called the transit time spread (TTS). It is an important property that defines the best possible time resolution. Especially in coincidence measurements it is desirable to have a small TTS in order to keep the coincidence window as short as possible.

2.5.4 Signal and Noise

The electrical signal of a detected photon is a voltage drop at the anode, caused by the electron cloud arriving from the dynode structure. An example of such a signal is given in figure 2.7 as voltage over time, obtained with a digital oscilloscope. Knowing the resistance of the power supply circuit, one can obtain the charge from the voltage-over-time diagram.

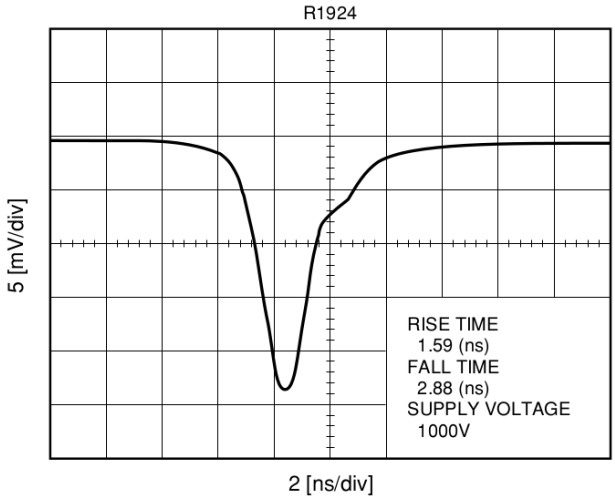

Figure 2.7: Typical electrical signal of a photoelectron event at the anode of a PMT, displayed as voltage over time. Figure adapted from [27]. The PMT that was measured in this example seems to be an R 1924, a small, one inch diameter, PMT with a bialkali photocathode and lower amplification than that of the KM3NeT PMTs.

A common application for a PMT is to count the number of detected photons. Towards this end, it is first necessary to determine the charge distribution for single (double, triple ...) photoelectron signals. (Note: If two photons simultaneously create one photoelectron each, they will both cause "their own" electron cascade in the multiplier part. Therefore, the signal measured at the anode will be a superposition of two single photoelectron signals.)
This can be done by illuminating a PMT in a dark box using very low level light pulses. The measured charge per light pulse can be entered into a histogram. This charge distribution can be analysed and the charge interval most likely corresponding to single (double, triple ...) photoelectron events can be extracted.

There are many electrical and electronic effects that can introduce noise into the signal; however, due to the relatively high magnitude of a real photoelectron signal, most of these are of little concern. The most important intrinsic noise of a PMT in many applications, and certainly in the use case of KM3NeT, is the dark rate. This is the rate at which the photocathode emits electrons by thermal excitation. These electrons will cause signals of the same qualities as those of real photoelectrons. They can therefore not be distinguished from true signal events. The dark rate can be reduced by cooling the PMT (which is not possible in KM3NeT, as opposed to the IceCube neutrino telescope, where plenty of cooling comes for free).
Other photoelectron-like signal events may come from electrons thermally emitted by the dynodes. These are smaller than photoelectron events, as they pass at least one less multiplication step, and are therefore easy to filter out by setting the lower charge threshold to a safe value. Usually, a value of 0.3 pe, meaning a 30 % of the typical charge of a single photoelectron events, is chosen as the trigger threshold.

Chapter 3

Neutrino Telescopes in a Coconutshell

3.1 Principle and Physics Goals

Neutrino telescopes aim to detect neutrinos originating from extra-solar and extra-galactic sources. Within our galaxy, possible point sources (sources that have a size below the angular resolution of the telescope, therefore looking point-like) may be supernova remnants. Other neutrino sources like reactions of high energy cosmic rays with the interstellar medium apear as a diffuse background. Extragalactic sources of interest include active galactic nuclei (AGN) and gamma ray bursts (GRB). A diffuse neutrino flux may be caused by the GZK effect (Greisen-Zatsepin-Kuzmin), which is the reaction of very high energy cosmic ray protons with photons from the cosmic microwave background.
The advantages of viewing these sources in "neutrino light" are that neutrinos point back directly at their source, and that they provide a look into the depths of their source, deeper than where gamma photons and protons can escape from.

A neutrino telescope is built deep in a transparent medium like water or ice. Neutrinos are detected via the Cherenkov light emitted by charged particles originating from neutrino interactions. Cherenkov photons are registered in a three-dimensional array of sensors. These sensors are usually one or several photomultiplier(s) enclosed in a glass sphere, forming an optical module (OM). Precise timing of arriving photons allows reconstruction of the events, which can be tracks, local showers, or a combination of both.

At the targeted kinetic energies of the neutrino of at least 10 GeV, an interaction will lead to a charged secondary particle which carries most of the energy and momentum of the primary. Its speed will be close to c and its direction of travel will be (within less than one degree) that of the neutrino. This leads to the emission of Cherenkov light at an angle of about 42° with respect to the direction of motion.

3.1.1 KM3NeT terminology

In KM3NeT, the sensor grid will consists of a number of "detection units" (DUs) anchored to the seafloor, forming the horizontal component of the detector grid.
Each DU will have a certain number of "storeys". A storey can have one or more optical modules. The vertical distance between storeys and the starting height above the seafloor make up the vertical component of the detector grid.

A DU consists of a structural element, which connects the storeys physically to the anchor and each other. As each storey has a certain buoyancy, added to by the top buoy, nothing more than rope of sufficient strength is needed.
A electro-optical cable (VEOC) runs vertically from the anchor to the top of the line, with a break-out at each storey.

For the storeys, several competing designs exists as of the writing of this thesis. The elegant and simple multi-PMT OM (DOM for digital optical module) design consists of a single OM per storey, eliminating the need for any additional structural elements. The DU is held together by a rope ladder, into which the VEOC is woven.
The bar or tower design has several single-PMT OMs per storey, mounted on a metallic structure which provides a horizontal separation of several metres between the OMs. This necessitates a more complicated rope structure and VEOC integration.

3.1.2 Signatures

Depending on the flavour of the incoming neutrino, the secondary can be an electron (both created or scattered), muon or tauon, or the corresponding antiparticles. These behave very differently when interacting with the surrounding medium and therefore leave different signatures in the detector. The possible secondaries of neutrino interactions are described below, with table 3.1 providing a quick reference. In many cases, a hadronic or electromagnetic shower can be observed at the creation vertex, if it lies within the detector itself or very close to it.

Electrons ($e^{+/-}$)

High energy electrons can be created by an electron neutrino interacting via a charged current reaction, in which case there is a hadronic shower near the vertex, or by elastic scattering off an existing electron, without producing a hadronic shower at the vertex. In both cases, the end result is a high energy electron.
Electrons scatter easily and cause electromagnetic showers by bremsstrahlung, pair production and ionisation. They therefore do not travel in a straight line, but are subject to frequent small direction changes when interacting. Their Cherenkov cone is fuzzy, reducing the achievable angular resulution, and their track is short. The electromagnetic shower products also emit Cherenkov photons and cause fluorescence. An electron-neutrino event is therefore an elongated bright spot with only fair directional information, but allows to estimate the neutrino energy

from the amount of light generated, if the interaction vertex is inside the detector.

Muons ($\mu^{+/-}$)

Muons can only be created in CC interactions, leading to a vertex shower. But due to their high mass, muons are only negligibly deflected, and relativistic time dilation allows them to travel several kilometers before decaying. The muons' long range allows to detect neutrino interactions far outside the boundaries of the detector, and their long and undeflected track makes it possible to reconstruct the direction of the neutrino. The Cherenkov cone of a passing muon sweeps over a number of OMs, and from the arrival times of the photons in the individual OMs, the track can be reconstructed. The energy information is limited. The energy loss of the muon can only be estimated along the visible part of the track. In water, a high energy muon loses about $2\frac{\text{MeV}}{\text{cm}}$ of kinectic energy [13] via bremsstrahlung, pair production, ionisation, and, to a very small fraction, Cherenkov emission.

Tauons ($\tau^{+/-}$)

Relativistic Tauons also travel in a straight line, but, due to their short proper lifetime of 2.9×10^{-13} s, they decay soon, even in the high energy regime. A large detector can therefore observe a creation and a decay shower connected by a track, if the kinetic energy is high enough to produce a discernible spatial separation of the two showers. This is called a double-bang event. Highly energetic tauons are therefore well suited for the reconstruction of the neutrino direction, but a large fraction of the decay energy goes into secondary neutrinos (see table 3.1 for the different decay channels and their signatures).

Figure 3.1, taken from [38], shows the mean range of each charged lepton, respectively the mean length of possible cascades, depending on the kinetic energy initially transferred from the neutrino.

Neutral Current Interaction

Neutral current interactions of all neutrino flavors result in a hadronic shower. Because the scattered neutrino retains most of its momentum, the energy information is limited, and the directional information gathered from a shower is only fair at best.

Event Examples from IceCube

The IceCube collaboration has published a plethora of beautiful event images. Figure 3.2 shows one event of each of the three types mentioned above. The images show a schematic view of the detector strings with their OMs. Coloured orbs depict how many photons were detected by each OM, and when they arrived. The size of each orb corresponds to the number of photons, whereas the colour scale translates into arrival time, with red being the start of the event, green being around 3 µs later, and blue being 5 µs after event start.

Reaction	charged current reactions			neutral current reactions, $x = e, \mu, \tau$
	$\nu_e + N \rightarrow e + X$	$\nu_\mu + N \rightarrow \mu + X$	$\nu_\tau + N \rightarrow \tau + X$	$\nu_x + N \rightarrow \nu_x + X$
Signature(s)	Electromagnetic + hadronic shower (superimposed)	Muon (+ hadronic shower if reaction inside detector)	(1) If $\tau \rightarrow \nu\bar{\nu}\mu$: Like $\nu_\mu N \rightarrow \mu X$ (2) If $\tau \rightarrow \nu\bar{\nu}e$: Like $\nu_e N \rightarrow eX$ (3) If $\tau \rightarrow \nu + \text{hadrons}$: Hadronic shower For decays (2) and (3) and τ energies above some TeV the showers from primary reaction and τ decay are separated in space and can be resolved ("double-bang signature")	Hadronic shower
Detectability	If reaction is inside detector light acceptance	If muon crosses detector light acceptance	If reaction is inside detector light acceptance, except for decay (1)	If reaction is inside detector light acceptance
Measurement precision	Energy: good. Direction: fair (a few degrees at best).	Energy: fair (factor 2 at best at muon energies above 1 TeV). Direction: very good (0.1° at high muon energies).	Energy: fair (large fraction of the ν_τ energy goes to secondary neutrinos). Direction: Good for decay (1), fair otherwise.	Energy: poor (largest fraction of the ν_τ energy goes to secondary neutrino). Direction: Fair.
Remarks	Important for diffuse flux measurements and flavour studies. Not distinguishable from other shower signatures	The golden channel for point source searches (neutrino astronomy). Muons of far-away events lose their energy before reaching the detector and may be of limited use for some analyses.	Like $\nu_e + N \rightarrow e + X$, except that energy measurement is less precise. Double-bang signatures might be very distinctive; otherwise not distinguishable from other shower signatures.	Like $\nu_e + N \rightarrow e + X$, except that energy measurement is much less precise. Not distinguishable from other shower signatures

Table 3.1: List of neutrino interactions and their signatures. The reactions are simplified, with N denoting a nucleon, X symbolising a system of hadronic particles, and the charged (anti)leptons shown as e, μ, and τ, without their respective charge. Hadronic and electromagnetic showers are particle cascades extending less than 10 m that appear as bright point sources of Cherenkov light in the detector. Muons have a range of more than 1 km for a kinetic energy above 1 TeV and are therefore line sources of Cherenkov light crossing the detector. Taken from [17].

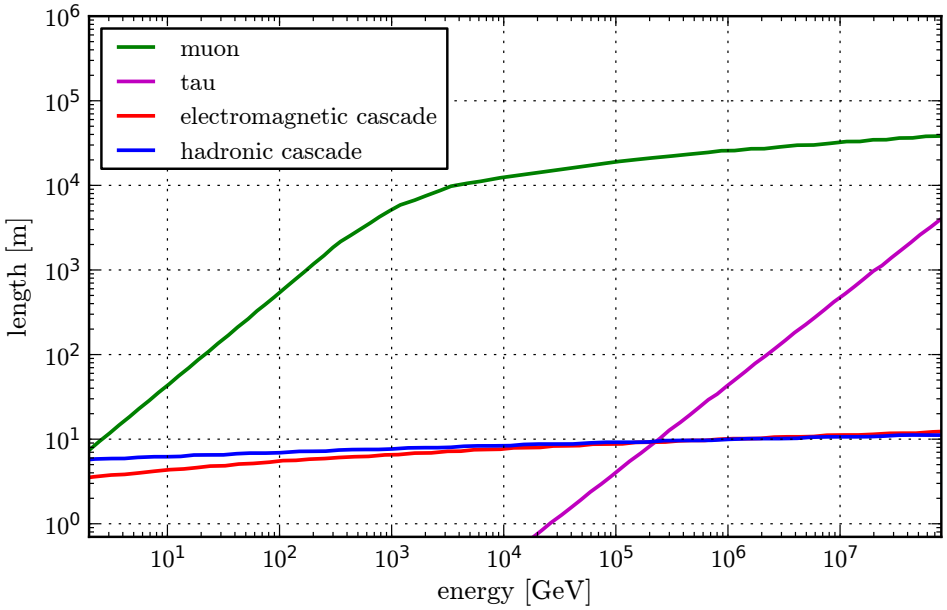

Figure 3.1: Mean path lengths for muons and tauons and cascade lengths for electromagnetic and hadronic cascades, depending on the energy transferred by the neutrino. Taken from [38].

3.2 Background and Challenges

Even the deepest sea is far from dark, at least from the perspective of a photomultiplier. More or less random background light causes variable hit rates in the PMTs. And even under perfect conditions, atmospheric muons and wrongly reconstructed tracks would add to the challenge of discovering genuine cosmic neutrinos.

3.2.1 Optical Background

The optical background originates from radioactive decays, both in the water and in the glass sphere itself, and bioluminescence. These two types have very different characteristics.
Surface light does not reach into the depths where neutrino telescopes are deployed.

^{40}K

Decays of ^{40}K are a large and constant source of background light in the deep sea. The upside is that the properties of the emitted light makes it possible to use ^{40}K as a calibration tool. These properties will be detailed in the analysis of the simulation data and compared to first measurements with the KM3NeT pre-production model optical module (PPMDOM).

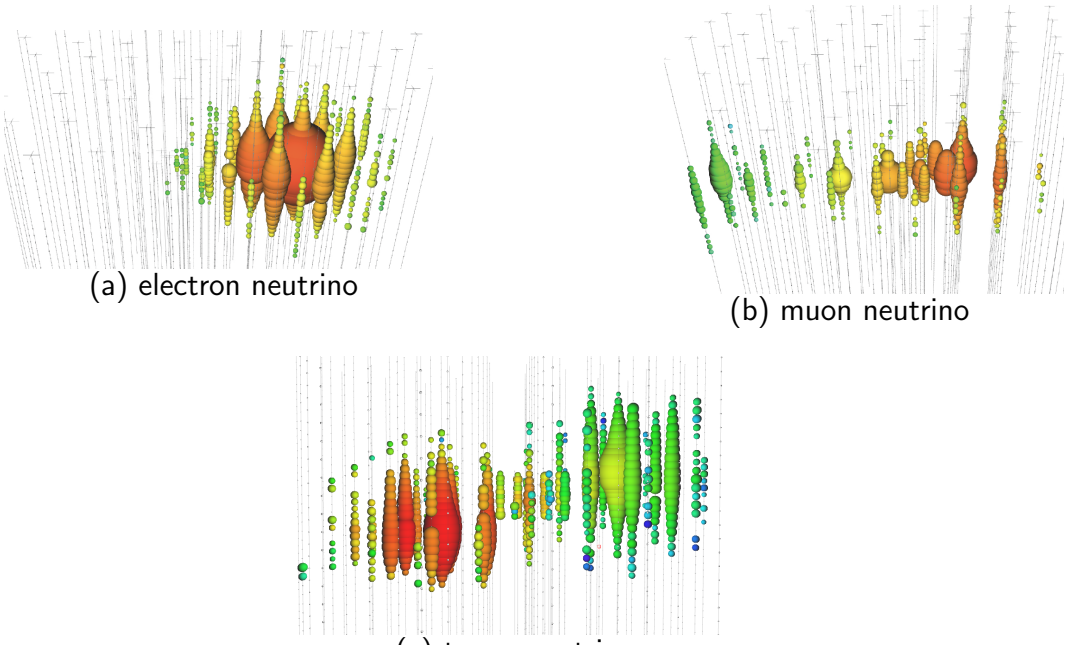

(a) electron neutrino

(b) muon neutrino

(c) tauon neutrino

Figure 3.2: Signatures of different neutrino events. Electrons created or scattered by (electron) neutrinos cause an electromagnetic shower, which causes light emission in more or less random directions, as seen in 3.2(a). Muons can travel for kilometers and often cross the whole detector 3.2(b). Tauons are so short-lived that the cascades from their creation and decay are close together or often merged, but at the highest energies create the typical double-bang event signature shown in 3.2(c). Coloured orbs show the photon arrival time in spectral colours, from red being at the start of the event to blue equalling $> 5\,\mu s$ later. Orb size corresponds to the number of photons at each OM or group of OMs.

Bioluminescence

The background light that one observes can be differentiated into two components.
One is a, on short time-scales, constant contribution which is thought to originate from luminous bacteria. The concentration of these varies with season and origin of the undersea current, which leads to a slowly changing background light level.
The other contribution are short bursts, usually a few seconds to tens of seconds long, of high rates that usually affects only one OM, and as data from the PPMDOM shows, only a few PMTs of an OM. This is believed to be caused by small organisms colliding with the glass and flashing in anger. This effectively blinds the affected PMT, making filtering this type of noise relatively easy.

Dark Rate

The dark rate of each PMT adds to the total measured photon rate. Compared to the other noise factors, this is a relatively small effect. The specified dark rate of the KM3NeT PMTs will be below 2 kHz, whereas the background rates observed with the PPMDOM PMTs lie between 9 and 11 kHz in periods of low bioluminescence.

3.2.2 Signal Background

Even without optical background, a neutrino telescope would more aptly be called an atmospheric muon detector. Highly energetic muons from hadronic showers caused by cosmic radiation (protons or nuclei) in the atmosphere easily reach several kilometers deep into the water.

To distinguish atmospheric muons from those created in neutrino interactions, one can simply look downward: Only neutrinos can travel through the earth, therefore a muon coming from underneath can only have been created in a neutrino interaction. Another possibility, at least in a large detector, is to use part of the detector as a veto: A muon track that starts somewhere within the detector must originate from a neutrino.

Still, things are not quite so simple: In hadronic air showers, pions are created, which in nearly 100 % of the cases decay to a (anti)muon and a corresponding neutrino. These atmospheric neutrinos are as likely to be detected as cosmic neutrinos, which has to be taken into account when analysing data.

3.2.3 Challenges

Some key technical challenges of building and operating a detector in a corrosive and dynamic environment will be detailed in th following.

All parts of the detector have to be watertight up to 500 bar of pressure, under which the glass spheres shrink in diameter by up to 1 cm from a normal diameter of about 43 cm. Cables and connectors are filled with oil to withstand the water pressure. Some connections have to be made under water, necessitating the use of wet-mateable connectors certified for these depths, and a remote-controlled submarine to perform these tasks. Metal parts have to resist corrosion, which is why in ANTARES the storey structures are made from titanium. Safeguards against leakages are needed, so that a flooded module or electronics box does not affect a significant part of the detector.

Apart from the engineering challenges posed by the high pressure and the corrosive environment, the dynamic nature of the sea necessitates additional means to extract useful data from the neutrino telescope.
The optical modules, or in the case of ANTARES, the storey structures, are mounted on a cable anchored to the seafloor and held upright by a buoy and by the buoyancy of the OMs. This

structure is called a line in ANTARES, a string in ICECUBE, or a detection unit in KM3NET. Subjected to the sea current, the line deforms and the storeys can rotate. Therefore, a number of instruments to measure the shape of the line and the orientation of the storeys are necessary to determine the position of each OM at all times.
In ANTARES, each storey has a central electronics canister which contains a compass card to measure the rotation and tilt of the storey. From this information it is already possible to determine the line shape with high precision. Additionally, a number of storeys per line carry hydrophones. Acoustic emitters on the sea floor allow for triangulation of the storey positions. The KM3NET OMs will have similar equipment. Instead of sporting external hydrophones, they will be equipped with piezo sensors glued to the inside of the sphere (visible in picture 4.2 a).

3.3 History

The basic idea of a neutrino telescope was formulated by M. A. Markov as early as 1960 [12]. The first steps towards the construction of a deep sea (or ice) neutrino telescope were taken in 1976. The DUMAND Project (Deep Underwater Muon And Neutrino Detector) was even then aimed at building a cubic kilometer sized neutrino detector in the Pacific, which was to employ both optical and acoustic detection methods, and would have reached as deep as 5 km below sea level [7].

It then took two decades until the first neutrino telescope was completed: AMANDA, the Antarctic Muon And Neutrino Detector Array. It was built into the eternal ice at the south pole. AMANDA took data starting from 1997 [19] and was shut down in 2009, having been made obsolete by ICECUBE. It provided the first flux limits on high energy cosmic neutrinos. In its final version, AMANDA had 19 strings with 677 optical modules and formed a circle of 200 m in diameter, at a depth of 1.5 to 1.9 km. This corresponds to a volume of less than 0.02 km^3. The optical modules comprised one 10-inch PMT looking straight down, housed in a 13-inch glass sphere.

Of similar size as AMANDA is ANTARES [8] (Astronomy with a Neutrino Telescope and Abyss RESearch), located in the mediterranean sea about 40 km south of Toulon at a depth of almost 2.5 km. ANTARES was constructed from 2005 to 2007 and consists of 12 strings in an octagonal arrangement. Each string has 25 storeys of 3 optical modules around a central electronics canister. The vertical separation between storey is 14.5 m, with the bottom-most storey positioned 100 m above the sea floor. The distance between strings is between 60 and 70 m. ANTARES has an instrumented volume of about 0.03 km^3.
The optical modules consist of a 10-inch PMT in a 17-inch glass sphere. The three OMs of a storey are arranged as an equilateral triangle, with the PMTs facing downward at an angle of 45°.

The largest neutrino telescope in operation today is Icecube. It was constructed around and throughout AMANDA starting from 2004. The detector was finished in December 2010 with 86

of the originally planned 90 strings deployed. Since then, further, more densely instrumented strings were deployed, in order to form a more sensitive core in the centre of the detector. The standard strings are instrumented along the bottom 1000 m of their 2450 m length. The string spacing is 125 m forming a hexagon. Each string carries 60 OMs made up of a 13-inch sphere housing a 10-inch PMT. IceTop, a detector for cosmic ray cascades consisting of ice tanks with photomultipliers, serves as supplement and veto for the main in-ice part of the system.

Often overlooked are the efforts of the Baikal experiment located in the Baikal lake in Siberia. Experimenting with various neutrino detectors of increasing size since the early 1980s, Baikal have run their completed 8 string detector NT-200 since 1998 and presented plans for a km^3 scale detector dubbed GVD (Gigaton Volume Detector).

3.4 KM3NeT

Part of the information given below was gained from various sources while working in the collaboration (personal notes from presentations and discussions, text documents now unavailable, private communication). It is therefore not possible for the author to cite sources in all cases. As far as possible, claims were backed up by information given in the proceedings of the VLVνT 2013 [20]. For current information about KM3NeT, feel free to visit its homepage [15].

KM3NeT started out in 2006 [17] as an effort to build a km^3-scale neutrino telescope in the Mediterranean, to compete with Icecube. Involved were and are many ANTARES veteran institutes, enabling the KM3NeT collaboration to directly benefit from the experience gained from building and running the first deep sea neutrino telescope. Apart from technical research and development to cope with this challenge, a lot of effort was invested into finding the detector makeup and geometry that would yield the highest sensitivity in the desired neutrino energy range. Handicapped by changing physics goals and the uncertain financial situation, the final design agreed upon now is a number of smaller "building blocks". The first two blocks will be built and deployed concurrently near Capo Passero (Sicily), the site of the Nemo project, and near Toulon (France) at the ANTARES site, the infrastructure of which will be upgraded thanks to funding from the local development project MEUST. As of November 2015, the second detection unit has been completed and delivered to Sicily for deployment.

Due to existing funding agreements, the first detection units at the Italian site will be Nemo towers. The storeys of the tower are 6 m long horizontal bars instrumented with an optical module at each end. The bars of adjacent storeys are rotated by 90°with respect to each other. Buoys on top and on each storey provide the necessary buoyancy. The cable and rope routing is designed such that the whole tower, compacted into a container of standard oversea container measures, can be unfurled from the seabottom without damaging the cable.

The regular KM3NeT detection units (DU) resemble rope ladders with single OMs spaced vertically, making up the 18 storeys of each "line". A DU is wound onto a kind of spool, dubbed

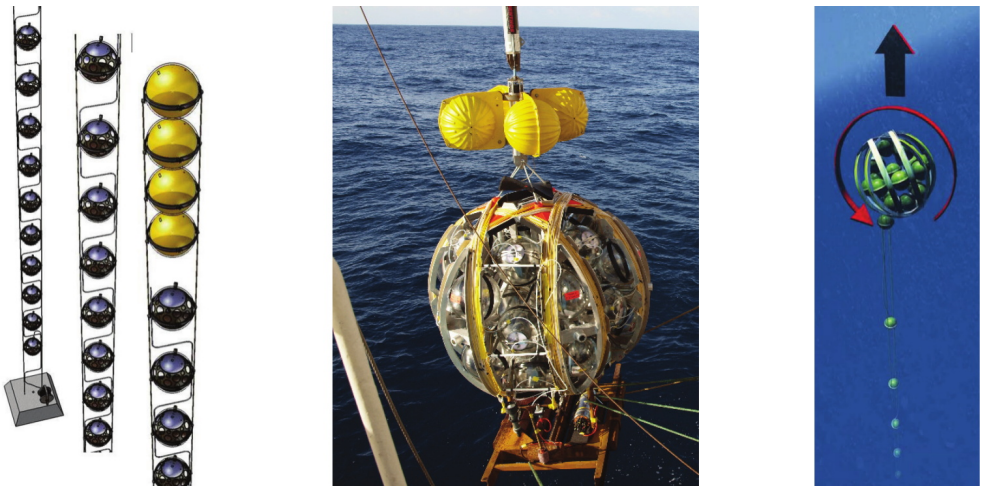

Figure 3.3: Illustration of a detection unit (left), deployment method using the LOM (right), and photograph of the deployment of the pre-production model detection unit (centre), taken from [23].

the LOM (launcher of optical modules), which can be lowered to the seafloor and released by remote control. The LOM will then rise and unwind the line with minimal stress on the ropes and cables; it can then be recovered and reused for the next line. The time to wind a line onto a LOM will be less than a day once massive deployment starts. See figure 3.3 for an illustration of the DU and the launcher.

During the years of KM3NeT preparation, the preferred design has changed quite a few times. New results of IceCube and other cosmic ray experiments, which were published in the meantime, led to rethinking and re-rethinking of the physics goals. In the end, it is open which design will be the best, but what seems certain is that there will be new discoveries from a multiple cubic kilometre neutrino telescope.

3.5 Alternative Methods and Future Projects

3.5.1 Acoustic Neutrino Detection

The showers created by neutrino interactions deposit a certain amount of energy in the water, which leads to a short local increase in temperature. This causes a pressure wave which can be detected with hydrophones or even with piezo sensors within an OM. The range of this sound wave is longer than that of photons in water, but the emission is confined to a rather flat disc, the so-called "pancake". A pilot project dubbed AMADEUS (ANTARES Modules for Acoustic Detection Under the Sea) exists within ANTARES as a feasibility study for this detection method.

3.5.2 Radio Detection

In certain media, like ice or lunar rock, a charged particle travelling faster than the spped of light in that medium causes an electromagnetic shower which produces a cone of coherent radio emission. This is called the Askaryan effect, predicted in 1962 and first observed in 2000 at the SLAC [6]. Upward going neutrinos interacting close to the surface could therefore be detected by antennas. The ANITA balloon experiment (Antarctic Impulse Transient Antenna), which had several polar flights so far, is looking for these signals. Using radio telescopes to scan the moon for neutrino induced radio signals has also been proposed.

3.5.3 Oscillation studies

Both the Icecube and the KM3NeT collaborations currently run feasibility studies about using atmospheric neutrinos for neutrino oscillation studies. To this end, one would need to deploy a rather dense detector array, due to the low energy range one would need to observe. In KM3NeT, this effort has been named ORCA (Oscillation Research with Cosmics in the Abyss), as a friendly jest to Icecube's PINGU project (Precision IceCube Next Generation Upgrade).

Chapter 4

The KM3NeT Multi-PMT Digital Optical Module

4.1 Concept and Advantages

The multi-PMT digital optical module (DOM) is a radically new concept in neutrino astronomy. It was developed at NIKHEF in Amsterdam. The concept was presented at the 2nd International Workshop on Very Large Volume Neutrino Telescopes (VLVνT2).

Instead of a single large photomultiplier, an array of 31 small tubes is built into a standard 17-inch pressure resistant glass sphere. This offers a number of advantages compared to the classic way.

Firstly, the PMT array covers a larger solid angle, providing a wider field of view. With this comes a larger photocathode area, which means that more photons are collected, which means that each multi-PMT OM gathers more information than a classical single-PMT OM.
Secondly, the segmentation of the sensitive area of the OM allows for better charge resolution: Two photons that hit a large PMT in a classical OM create a charge at the anode that may or may not be significantly larger than the average single photo electron (spe) charge, whereas in a multi-PMT OM these two photons are likely to land in two distinct PMTs, creating a clear single photon event in both.
Thirdly, the spatial separation of the PMTs within the sphere allows to suppress random background photons arriving from a different direction from the photons of a real event, and offers ways to better reconstruct and reject atmospheric muons, whose Cherenkov photons arrive from above.
And finally, for events of a certain minimum brightness, a crude direction from the OM to the source of the detected photons can be derived from the positions of the PMTs that were triggered, which can serve as a starting point for reconstructing particle tracks or shower vertices. This can improve and speed up the reconstruction and analysis processes.

Figure 4.1: Picture of an 80 mm photomultiplier tube tested at ECAP. Taken by the author on 22 July 2013 during the assembly of the lower half of a DOM.

4.2 Photomultipliers

The photomultipliers for the DOM are a special development for KM3NeT and delivered by competing suppliers. The specifications, both in terms of physical shape as well as concerning technical characteristics, are listed in table 4.1.

The PMTs under development are mushroom-shaped tubes with a diameter of 80 mm or slightly more. There are strict requirements on quantum efficiency, dark rate and signal characteristics imposed on the suppliers. As one limiting factor on how many PMTs fit into an OM is the depth of the PMT and the space needed by the PMT bases in the centre of the sphere, the tubes have to be shorter than what would be usual, adding to the manufacturers' challenge.

To further increase the effective area, the PMTs will be fitted with reflective collars of some sort that reflect photons narrowly missing a photomultiplier onto the side of that PMT's photocathode. This is an inexpensive way of increasing the sensitivity of the DOM by minimising the unused area between neighbouring PMT faces. Picture 4.2(f) in figure 4.2 nicely shows how little of the surface area of the DOM remains unused.

Tube shape	mushroom
Diameter	80 mm
Photocathode diameter	>72 mm
Quantum efficiency	>23 % at 404 nm
	>18 % at 470 nm
Nominal Voltage for a gain of 3×10^6	900 ... 1300 V
Dark count rate	<2 kHz
Transit time spread	<5 ns

Table 4.1: Excerpt from the design specifications of KM3NeT photomultiplier tubes, as presented at the VLVnT 2013 [20], [21], [22].

4.3 Layout, Components and Construction

The basic layout of the multi-PMT OM is one PMT pointing straight down, and 30 more arranged in layers, or "crowns", of six evenly spaced PMTs each.
The lower hemisphere of an OM contains 19 PMTs: The one pointing downwards, and 18 more arranged evenly in three crowns of 6 PMTs each. The crowns are rotated by 30 degrees with respect to their upper or lowers neighbours to achieve the most compact spacing.
The glass spheres are assembled from two hemispheres, which are coupled by evacuation and sealing tape around the equator. Therefore it is convenient to assemble the halves of the OM independently. When closing the sphere, one only needs to connect the cables leading from the lower half to the upper.
The upper hemisphere contains 12 more PMTs arranged in two crowns, as well as the electronics and heatsink. The mushroom shaped aluminum heatsink occupies the upper portion of the OM, with its stem reaching down into the OM to allow thermal coupling to the electronics boards. Figure 4.3 shows a photograph of the prototype OM deployed in the ANTARES instrumentation line. The exact position of each PMT, in spherical coordinates, is listed in table A.9 in the appendix. These values were used to create the simulated OM.

During assembly, the prepared PMTs (with their bases soldered on) are inserted into a support structure, which can then be put into the glass hemisphere in its entirety. The optical coupling to the glass is achieved with a layer of optical gel of approximately 2 mm thickness. The initially liquid gel is poured into the space between the PMT support structure and the glass shell. During curing, which takes about a day, the gel solidifies.
The best way to mass-produce the support structure is still under investigation. At the time of this writing, a hybrid of simple and cheap moulded plastic hemispheres with slightly oversized cut-outs for the PMTs, combined with 3D-printed PMT holders, to accommodate different PMT types and reflecting collars, seems to be the most promising idea in terms of flexibility, speed and cost efficiency.

The PMTs are driven and read out by active bases developed at Nikhef in Amsterdam. These provide the high voltages to the photocathode and dynodes using highly efficient DC-DC step-up

converters, which in their first production version were claimed to consume only about 30 mW of electrical power. They also digitize the PMT signal and transfer it to the central logic board.

Further instrumentation in the DOM include a compass, tilt meters and a piezo sensor. In the completed detector, the piezos will be used for "acoustic positioning" of the OMs. This means that the exact position of an OM can be triangulated by measuring sound pulses emitted by beacons located on the sea floor. Due to the sea current, the position of the top of the line can vary be several tens of meters, therefore the exact location of each optical module is a vital piece of information for data analysis. Additionally, the piezo sensors could be used as an additional, and inexpensive, means of detecting neutrinos, as has been pioneered by the AMADEUS group.

Figure 4.2 shows some impressions of the first integration of a DOM at the ECAP.

4.4 Data Sampling

In KM3NeT, the same philosophy of "all data to shore" as in ANTARES will be employed. This means that the raw data, mainly the hits registered in the numerous PMTs, is transferred to the shore station. All processing, filtering and analysing is done at the computer farm at the Institute Michel Pacha, the control station of ANTARES. This strategy defines the necessary speed of the network connection from the detector to shore.

While in ANTARES the analogue waveforms of the PMT signals are sampled, for KM3NeT, with its staggeringly huge amount of PMTs, a scheme had to be found that would create less network traffic. The solution was the time-over-threshold scheme (ToT). For each PMT signal event, the time difference between when the anode voltage drops below a certain threshold until when it again rises above that threshold, is recorded. Therefore a PMT hit only consists of this time difference and the time when the first crossing of the threshold occurred, which marks the beginning of the event. Using charge calibration measurements of every PMT that goes into a DOM, one can relate each recorded ToT to a charge in spe equivalents. Thus, the data that needs to be transferred from the experiment to the shore station is drastically reduced to a timestamp (high precision floating point number) and a time difference (integer of byte size), for each hit registered by a PMT.

4.5 The Pre-Production Model Digital Optical Module

The so-called PPMDOM was integrated into the ANTARES instrumentation line (IL) that had previously been recovered from the sea. The IL has been redeployed on 16th April 2013.

The PPMDOM is built mostly from intermediate hardware: The PMT support structure is a shaped foam plastic, the PMTs are of a different and smaller type compared to the final version

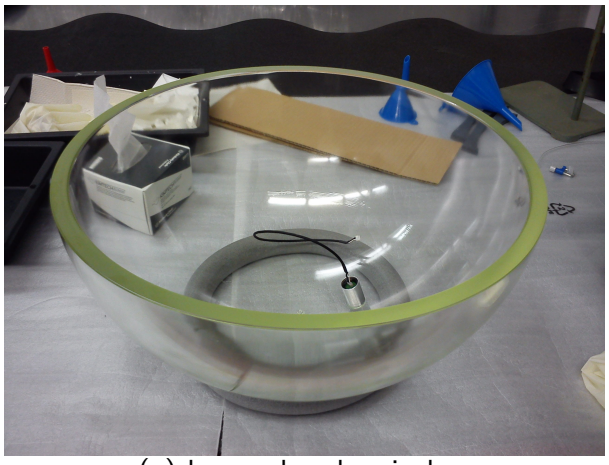

(a) lower glass hemisphere

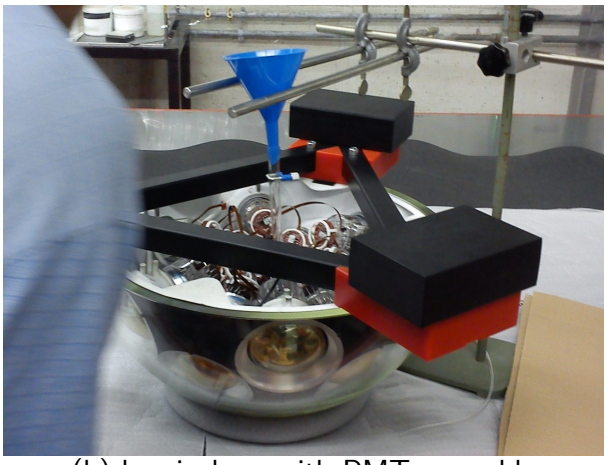

(b) hemisphere with PMT assembly

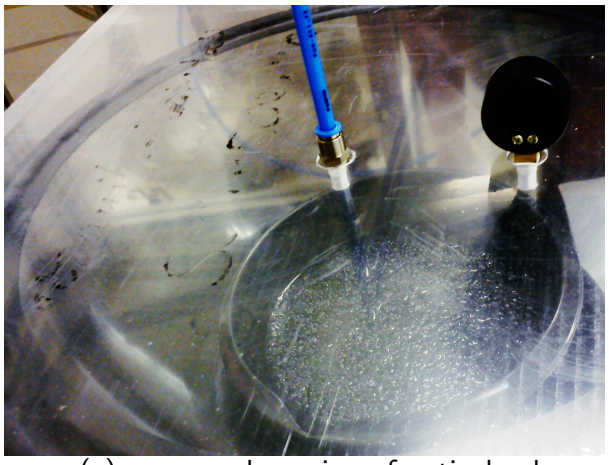

(c) vacuum degassing of optical gel

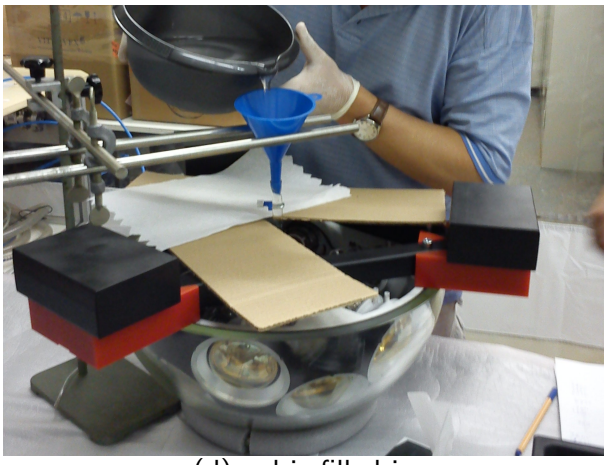

(d) gel is filled in

(e) gel level rising

(f) lower half completed

Figure 4.2: The first integration of a DOM (half) at the Erlangen Centre for Astroparticle Physics. The bottom hemisphere has been prepared with the piezo for acoustic positioning and signal detection (a); the holding structure with 19 PMTs is placed in the hemisphere (b) – note the tube which will direct the liquid gel to the bottom; the two-compound gel has to be degassed in several vacuum cycles (c); gel is filled into the gap between PMTs and glass wall via the funnel and tube (d); as the gel level rises, one can see the effect of the optical coupling of the PMT and light collection rings to the glass (e); completed lower DOM half (f) – isn't she a beauty?

Figure 4.3: Picture of the PPMDOM, taken during deployment at the ANTARES site. Note the customised holding structure and the proximity of the local control module. The shadow cast onto the PMTs by these obstacles will be visible in the data.

of the DOM, the reflecting collars are narrower, and without going into too much detail, most of the electronics have since been replaced by different solutions (e.g. in the optical network) or newer revisions.
Nevertheless, the PPMDOM has worked well with only minor problems, and has delivered a large amount of data since its deployment, analyses of which are detailed in chapter 7.

4.6 Technical Specifications

Tables 4.1 and 4.2 include the most important specifications of the DOM and PMTs that were used in the simulations performed in the context of this theses. Some more details can be found in appendix A.1.

Diameter	17"
	432 mm
Wall thickness	14 mm
Pressure resistance	>5000 m of sea water
Gel layer	2 mm
PMTs	31 of 80 mm ⌀
Light collector in simulation	reflecting ring, 12 mm width
Light collector in DOM	integrated lens assembly
	of similar dimensions
Photocathode area	>140,000 mm^2

Table 4.2: Excerpt from the design specifications for the KM3NeTDOM, used as input for the final simulations. Only details relevant to the simulation are listed.

Chapter 5

Simulation of the DOM

The main purpose of the simulation I developed in the context of my thesis was to predict the typical optical background caused by ^{40}K decays. This included the rates of single photon hits in the PMTs, as well as coincidence rates and typical patterns.

Previous efforts in this area simulated ANTARES modules and storeys. The existing programmes of which I had access to the source code ([30], [31]) were not easily adaptable to the multi-PMT OM, or more detailed than was necessary. In many cases, parameters describing the OM and its properties were hard-coded in the source code.

My goal therefore was to create a simulation that could easily be adapted to keep up with the ongoing development of the KM3NeT OM and detector geometry. I wanted the simulation to be just detailed enough to accurately simulate the passage of photons from the creation vertex up to the impact on the photocathode. Furthermore, I wanted to strictly separate the simulation and analysis steps of the chain, so that parameters that only affect the latter could be changed and evaluated without having to rerun the CPU intensive particle physics simulation. Finally, it had to be easily possible to combine the output of different simulation runs, thus enabling distributed computing on the local cluster.

Another application that could be derived from the ^{40}K software was the simulation of the OM acceptance. This describes the sensitivity of the OM as a function of the arrival direction of a uniform light front. The information gained from those simulations was used to create a pointing algorithm that can help in event reconstruction once KM3NeT starts taking data. In the earlier development phase of the DOM, this simulation was used for realistic sensitivity studies of the evolving DOM designs, or to test the geometry of a proposed design change.

Finally, the simulation was experimentally extended to simulate the passage of muons in the vicinity of the optical module. The idea was to simulate the signature of muons passing the DOM in a given distance. It turned out that at the level of detail of my simulation, the CPU cost was rather high for the computing cluster available at that time. As there were other simulations available that were better suited to that task, I did not pursue this direction.

5.1 GEANT 4

GEANT 4 (from GEometry ANd Tracking) is an object oriented toolkit written in C++ for creating particle physics simulations [1], freely available under the GNU GPL and widely used in the field of particle physics and beyond.
It provides C++ classes to construct a detector geometry, to define materials, to create primary particles, and to simulate the propagation of particles through matter and the interactions occuring thereby. The interactions that can be simulated range from simple optical to electromagnetic to the most complex baryonic processes. Furthermore, radioactive decays and decay chains can be simulated.
As Geant takes care of all the selected physics processes, the application developer can concentrate on designing the virtual detector and extracting the desired data.
The downside is that the level of detail with which particle interactions are simulated in GEANT leads to high demands in CPU time.

5.1.1 Detector Geometry

The virtual detector in GEANT 4 is constructed by first defining the geometric building blocks, called "solid volumes" or "solids", made from elementary geometric shapes like cuboids, spheroids, ellipsoids or cylinders. The primitives each have a number of parameters, from the basic dimensions to for example (and where applicable) inner and outer radius, starting and ending angles in ϕ and θ direction, or even twists. This already provides a high degree of flexibility. Furthermore, solids can be combined using unions, intersections or subtractions.
Should these capabilities be insufficient, one can import shapes created with CAD software using boundary represented solids. For the accurate representation of the optical module, the primitives proved sufficient.

From a solid, which is the template of a shape, one can derive one or several logical volumes. These can individually be assigned material properties like atomic composition, mass density and thermodynamic state, and optical properties like index of refraction, absorption length and scattering length.

To finally build the detector, logical volumes are physically placed inside other logical volumes to build more complex detector elements, or into the "world volume". As a general restriction, a logical volume placed inside another one may not protrude from that; this also means that every volume has to be contained withing the world. A visual example of the building process of an optical module is given in 5.2.1 in figure 5.2.

5.1.2 Event Generation, Particle Tracking and Physics Processes

A GEANT 4 simulation is event-based. In GEANT 4 terminology, an event is everything that happens from the creation of the primary particle(s) to the destruction of the last secondary

particle. Each event gets a unique identifying number, counting up from 0. A run is a sequence of events. The application programmer can introduce code for accessing, processing and storing data on all particles created during the event.

At the beginning of each event, the primary particle(s) is (are) created and inserted into the virtual world. To this end, a "particle source" C++ class has to be defined and registered. It can emit or create the desired primary particles, one at a time or in groups, in a wide range of preprogrammed or customised distributions that can be applied to the particle's position, energy and direction. The particle source definition for a GEANT 4 simulation can be hard-coded in the C++ class, or the class can be left empty and the source configuration can be entered using a text file.

The primary particles are propagated and subjected to appropriate interactions, generating secondary particles and triggering detector response along their way. The interactions that each particle type can undergo are chosen by the application programmer. The physics list C++ class contains these selections, while the underlying GEANT 4 framework already contains the physics processes, i.e. the programme code that defines and calculates the actual interactions. It is also possible to program custom processes. For use in KM3NeT simulations, Claudio Kopper wrote a custom optical scattering process [34] that implements the scattering formula and parameters defined in the WPD simulation document [5].

When all primary and secondary particles have been destroyed, dropped or left the world volume, the event ends. GEANT 4 keeps track of the elapsed time since the start of an event and puts a timestamp on every interaction. At the end of an event, the data gathered during that event can be stored by the application programmer.

The destruction of a particle automatically happens when it leaves the world. Particles can also be destroyed in an interaction, or taken out of the simulation when their kinetic energy crosses a threshold below which the particles become uninteresting. Optical photons are immediately absorbed by materials with undefined optical properties. If a material has optical properties, photons can be reflected, refracted, scattered, or absorbed according to the specified properties like refractive index, absorption length and scattering length.

The information on every particle is stored in the track object, which can be accessed at the beginning (the creation) and the end (the destruction) of a particle's trajectory. The track is made up of steps of variable length. At the beginning of each step, a free path length is requested from each physics process that can affect the particle. The process with the lowest bid "wins": The particle moves the appropriate distance and interacts at the end-point of this step.
In the case of optical photons, steps always end at optical border surfaces, to allow for the simulation of refraction and reflection.

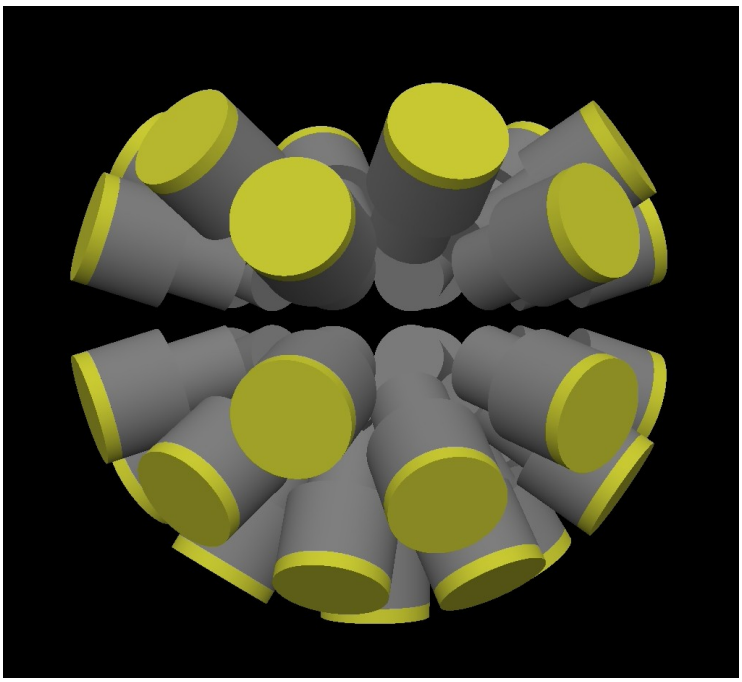

Figure 5.1: Raytrace of the first implementation of a DOM in a GEANT 4 simulation. The simulation crudely recreated standard cylindrical 3-inch PMTs with flat input windows. The glass shell and gel layers had not been included, the PMT positions differ slightly from the final DOM version.

5.1.3 Data Extraction

The application programmer can write routines to extract information before and after each run, each event, each track and even each step. At the step level, this can be done manually or by defining certain elements of the detector as sensitive, which leads to the creation of a hit object if a particle interacts with those. In all cases, the programmer has to implement methods to extract and store the available information in the desired fashion.

At the step level, one can even manipulate particles in flight. In the example presented here, this approach was used (instead of sensitive detector elements) in order to register those photons that impinge on a photocathode and eliminate them from the simulation.

5.2 Description of my Simulation

My simulation consists of a detailed model of an OM, or a group of OMs, in a world volume with the properties of sea water. Most simulation parameters can be changed by specifying the desired configuration files at programme start. Configuration and position of the optical module(s) are specified in a detector configuration file. Sea water parameters are split into refraction, absorption, and scattering tables, each in one file. Having all these settings ex-

ternalised allowed to quickly run batches of simulations in different configurations in parallel, without having to change and recompile the programme after each batch.

During a simulation run, at the start of each event, one ^{40}K atom is placed randomly inside the water, with a kinetic energy of 0. After a certain virtual timespan has passed, randomly chosen by GEANT 4 under consideration of the half-life of the isotope, a radioactive decay takes place. As the potassium atom is at rest and there are no other processes that may influence it, the decay is the first physics process that happens in each event. The half-life of ^{40}K has been set to an extremely short time (10^{-15} seconds, so that the time span between event start and the decay will be much shorter than one nanosecond and therefore negligible. This is necessary because otherwise, the needed sub-nanosecond time resolution will be lost due to the limited number of digits representable by double precision floating point variables.
GEANT 4 will randomly choose a decay channel and create secondary particles according to it, and with appropriate (randomised) (kinetic) energies. The interactions of the secondary particles (electrons and positrons, gamma and optical photons) on their way through the water are simulated, most importantly the creation of Cherenkov photons. The latter are tracked until they leave the boundaries of the world, get absorbed in water or reach a PMT of the OM. When all secondaries are destroyed by either leaving the world or crossing the energy threshold beneath which they cease to be tracked, the event ends.
All photons that impinge on the photocathode of a PMT during the event are registered at the step level, and their information (impact time, photon energy, exact position and direction) is stored and written to disk at the end of the event.

The simulation output is a text file. It contains a header with the relevant parameters of the simulation run, followed by the list of photons that hit a photocathode and their associated information.
The text file format was chosen because the amount of data produced by the simulation is relatively small, it was easy to combine data from different program runs can, and because text files are robust against sudden program termination. In a computing cluster environment, a running instance of the simulation program can easily run into time limits, or the machine on which it runs may be rebooted, which means that the program gets terminated without warning. If that happens, a more space-efficient binary file format like a ROOT tree will be corrupt and contain no data. By using text files and writing out the simulation data in regular intervals, the data loss in case of program termination is minimal.

In the separate analysis process, data files from the many parallel programme runs of the same virtual detector configuration are combined in the first step. This data is then used to create a timeline of PMT hits using random factors like quantum efficiency. The timeline can then be analysed in the same way as data from the real detector.

5.2.1 Optical Module

The initial goal of the simulation software I developed was to simulate the ^{40}K background in multi-PMT optical modules. In the early design study phase of KM3NeT, several options for optical modules and their arrangement were being considered. Therefore it was obvious that my simulation had to be kept adaptable and easily configurable.

As a first step to get quick results however, a crude model was created by adapting an existing GEANT 4 simulation written by D. Goering [31]. This model reproduced only the PMTs of the DOM arranged at their appropriate positions, without the glass sphere. It therefore neglected the optical effects occurring at the media boundaries. The PMTs were approximated as cylinders, with the photocathode as sensitive area attached to one side. A depiction of this early simulation model is shown in figure 5.1.

After that version had produced first results, I started programming a new simulation from scratch. It had to reproduce the DOM so accurately that it would not only be possible to estimate the ^{40}K background rates, but also to predict the acceptance function of the module, which means its sensitivity as a function of the direction of incoming light. This meant that the geometric shapes of the real components had to be faithfully reproduced in the simulation, the dimensions of the optically active parts of the OM had to be exact, and the optical properties of the different materials had to be researched and included.

As the OM and detector designs were still in flux when the new simulation was developed, the OM simulation had to be kept flexible. At that time, three different detector designs were under investigation: The slim and elegant SeaWiet design, which consisted of multi-PMT OMs spaced on a string; the unwieldy Nemo Towers, with up to 10 m long bar structures serving as storeys, each bar being equipped with a number of OMs; and the Medusa design, which was a compromise back-up solution mirroring the ANTARES design, with three OMs per storey, each containing one 10-inch PMT.

To accomodate all design variants, it had to be possible to arrange several (even different) OMs in arbitrary configurations, and to use different types of photomultipliers in any configuration within the simulated OMs. Therefore, a large number of different PMT types was implemented over the years. Initially, the Hamamatsu R6233 flat window 3-inch PMT, as well as the 8- and 10-inch hemispherical types R5912 and R7081, were modelled using the schematics available on the manufacturer's website [28]. The latter was the PMT model used in the ANTARES detector and proposed to be used in the Medusa design, while the 8-inch tube was favoured for a time for use in the Nemo Tower.
Later, after the multi-PMT OM had become the preferred solution, and custom PMTs were being developed to optimally fit the DOM, the simulation was updated with each new variant. The last PMT type implemented was the Hamamatsu R12199, a mushroom-shaped PMT with a diameter of 80 mm.
The exact geometric descriptions of each PMT type had to be hard-coded in the simulation

code due to their complexity. Which OM configuration and composition will be used in a simulation run is selected via configuration files. It is possible to define an arbitrary number of different OM types and place them in the simulated sea water in any position and orientation. This flexibility has been used to simulate ANTARES storeys, Nemo Tower bars, and tightly spaced DOM storeys to simulate inter-OM correlations from ^{40}K decays

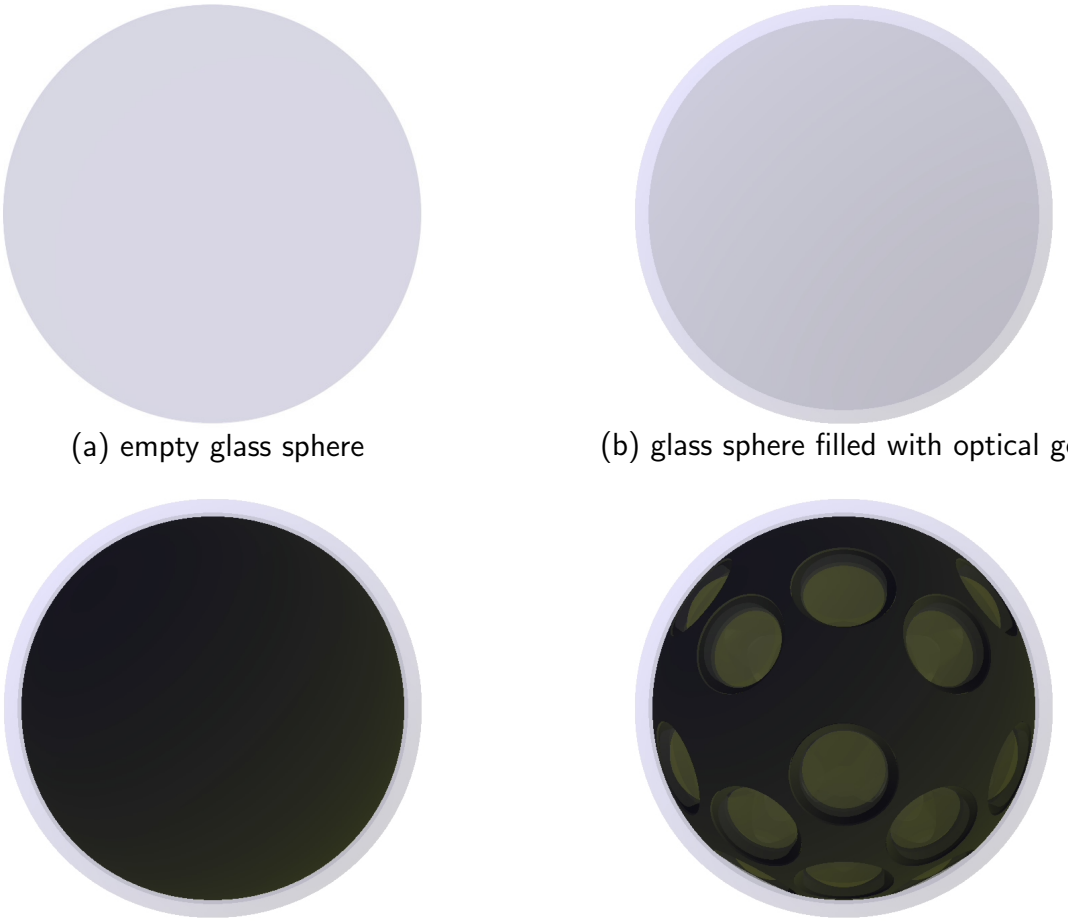

(a) empty glass sphere

(b) glass sphere filled with optical gel

(c) sphere of absorber material within gel

(d) completed module with PMTs

Figure 5.2: Construction steps of a simulated OM: Generate a solid spherical volume of material "glass" and with defined optical properties (a), which is then filled with a solid sphere of material "optical gel" with different optical properties (b), which in turn is filled with a solid sphere of material "foam" without optical properties (c). The final result is shown in (d): Cut-outs are made into the foam sphere, into which the PMTs (which are in themselves complex assemblies of different volumes and materials) are put. The PMTs are cointained within the gel volume and do not intersect the foam or protrude into the glass – should this happen by accident, it will be detected and reported by GEANT 4.

To reach the desired flexibility, I programmed the following algorithm to build optical modules with arbitrary PMTs.

First, the glass shell is modeled by defining a solid sphere of 17 inch or 432 mm diameter. This sphere gets the material and optical properties of the glass, which have been taken from the simulation of H. Constantini [30] and agree with openly available manufacturer's data. Inside the glass sphere, another solid sphere with a diameter of 404 mm is placed and assigned the properties of the gel. In combination, these spheres create a glass shell with a thickness of 14 mm, filled with optical gel.
The data on the optical properties of glass and gel was limited to a single wavelength each. Requests to get detailed, wavelength-dependent data from the respective manufacturers have not been answered.

The next construction step depends on the type of optical module. For a single PMT OM, the inside of the gel sphere is "filled" with a sphere of vacuum of smaller diameter. This effectively creates a glass shell, coated with a layer of optical gel in the inside. The PMT, which is a complex combination of primitive geometric shapes, can then be placed inside the vacuum.
In a multi-PMT OM, a support structure of virtual foam plastic is created by defining a sphere of a light-absorbing material. The diameter of this foam is chosen such that the desired gel layer thickness, defined in the configuration file, is reached. The desired photomultipliers, and, where applicable, their light collection rings, can be placed inside the foam sphere at a given distance from the glass shell, pointing into any direction. The foam sphere serves to isolate the photomultipliers from stray light that in the real world could not reach the photocathode. This greatly simplifies the modelling of the PMTs, as it allows the omission of details like the coating on the backside of the tube or the PMT base, without losing any realism when it comes to the optical effects between water, glass, gel and tube.

There is one caveat stemming from the way GEANT 4 handles logical volumes. The logical volumes of the PMTs have to be contained within a single surrounding logical volumes. If one were to place the PMT inside the foam sphere, the protruding front of the PMT, which in real life is embedded in the gel layer, would vanish. The solve this problem, the foam sphere actually has to be a complex construct: It is a sphere with cut-outs for each photomultiplier. This way, the PMTs are entirely located within the gel volume, as the gel fills the entire glass sphere, except for the space that the hollowed-out foam sphere occupies.
As a side note, the vacuum sphere in a single-PMT OM model has to be treated in the same way to avoid overlapping logical volumes.

The simulation of refraction, reflection and transmission at the border surfaces of the different optical media happens automatically, if the refractive indices of the involved materials have been defined. The default behaviour of GEANT 4 is to assume an interface between two dielectric materials and an optically smooth surface. This is the case for almost all of the border surfaces, namely the transitions from water to glass, from glass to gel and from gel to the glass of the PMT tubes.

The light collecting rings or collars that enhance the effective area of the small PMTs, described in chapter 4 and visible in figure 4.2, had to be implemented differently. They were still under development when the final version of my simulation was completed. In the months before that, shape, size, placement and construction of the collecting ring had been changing every so often. In all variants I implemented, the reflecting surface stood at a 45°angle to the PMT's longitudinal axis.

In the PPMDOM, the light collecting rings are conical rings made of PMMA, a transparent plastic, with one side coated with "something reflecting". Towards the end of development of the simulation, the preferred solution for the light collectors was "collars" cut out of thin aluminium sheets. Both versions, cones and collars, have been implemented in the simulation.

The collars are simple objects, modeled as solid aluminium cones with a polished surface and a reflectivity of 0.92 in the interesting wavelength range. This value has been measured in the photodetection lab at the ECAP on a piece of aluminium sheet from which reflecting collars could potentially be fabricated.

The cones are more complex, since they add another media boundary (gel to plastic) and need to have a single, manually defined smooth reflective side. Light enters the front of the cone (transition gel to PMMA), gets reflected at the angled, reflecting back surface, and exits through the inside surface towards the PMT (transition PMMA to PMT glass). For an accurate representation, the refractive index n(λ) of PMMA had to be implemented. A parametric formula has been obtained from [10]. The reflectivity was assumed to be equivalent to polished aluminium and fixed 0.92.

Apart from border surface effects, absorption and scattering are of importance for the simulation. The scattering lengths of the OM building materials are not known, but the absorption lengths of glass and gel have been implemented for the sake of completeness. Both effects are of little significance given the short optical path lengths within the OM.

5.3 Environment and Physics Processes

Every object in a GEANT 4 simulation has to be contained within the "world volume", which can be any shape and size. To simulate the ^{40}K background in a single optical module, the most suited shape of the world volume is spherical, so there can be no direction bias.
The world volume serves as the sea surrounding the OM. Given the physical and optical properties of sea water, GEANT 4 can simulate the applicable interactions for every particle traveling through it.

Firstly, a table of the atomic composition of sea water, including its most important trace

elements, is defined, and assigned to the world volume. This allows GEANT 4 to calculate the reactions of the secondaries created in ^{40}K decays. In the case of an electron capture, the emitted γ creates secondary electrons by photo effect and Compton scattering. These electrons and those from β decays lose energy by ionization and bremsstrahlung. The mass percentages of the elements can be found in the appendix in table A.2.

Optical photons in sea water are subject to scattering and absorption. GEANT 4 provides an absorption physics process and several scattering processes for optical photons. They both require that a table of absorption/scattering lengths is defined and assigned to a logical volume in the simulation. These tables are supplied in the simulation reference document [5] and assigned to the simulation's world volume. The reference document also defines a custom scattering function, which has been gained empirically from a number of measurements in the Mediterranean. This custom function has been implemented as an includable module for GEANT 4 by Claudio Kopper [34].

Necessary for the creation of Cherenkov photons in GEANT 4 are specified refractive indeces for the optical medium. For this simulation, the refractive index has been taken from the simulation working group reference document [5], where it is defined by formula 6, which allows to calculate the refractive index n(λ, p) of the sea water, in dependence of the wavelength λ and the ambient pressure p.
A table of the refractive indeces for a wavelength range of 290 to 720 nm has been created as input for the simulation. Outside of this spectrum, both the assumed absorption length of sea water and the quantum efficiency of the PMTs reach zero, so the simulation does not need to produce photons outside this range.
The ambient pressure used to calculate the refractive indices is equivalent to 3500 m of depth. This has been chosen in the reference document due to the depth of the Sicilian Capo Passero KM3NeT site. As the dependence of n on the ambient pressure is small, the error made in assuming a constant pressure over the simulated volume is negligible.
Both the formula and the table used as input for the simulation can be found in the appendix in chapter A.1.
The Cherenkov process in GEANT 4 is handled differently from the other processes that are implemented in the simulation. While most processes are discrete interactions taking place at a vertex, the emission of Cherenkov photons happens continuously along a particle's trajectory as it travels through an optical medium. Still, the Cherenkov process has to fit into the step-by-step propagation scheme implemented in GEANT 4. The Cherenkov emission is therefore calculated at the end of each propagation step, but the emission depends on the average velocity of the particle along the step. The amount of photons created per step can be chosen and is one factor limiting the step length, just as any other physics process that can influence a particle.
In other words, the electron travels a bit until it interacts, or until the maximum step length is reached. Then the new velocity is calculated, after which Cherenkov photons are created, based on the average of the old and new velocity. If the step length is too long, this may introduce errors in the amount of emitted photons and the opening angle of the Cherenkov cone.

Another oddity of the implementation of the Cherenkov process in GEANT 4 is that the creation of optical photons does not cost kinetic energy. This only leads to a negligible error of a few keV at most, compared to a typical inital energy of around one MeV for the β decay electron, but is something an application developer should keep in mind.

Table A.6 in the appendix lists all physics processes enabled in the ^{40}K simulation, and shows which particle types are affected by each process.

5.4 OM Acceptance Simulation

The sensitivity of the optical modules is an important input parameter for the large scale sensitivity studies that are a big part of the design process of a neutrino telescope. From the ^{40}K simulation software it was easily possible to derive a dedicated acceptance simulation with only minimal changes.

The particle source now needed to emit a parallel beam of monochromatic light of the same diameter as the OM. This was achieved by changing the configuration file describing the particle source, without having to modify the programme's source code.
Photons had to cross the space between light source and DOM without losses, therefore absorption and scattering had to be disabled. Instead of changing the source code, the elegant solution was to create sea water configuration files with extremely long scattering and absorption lengths.
In the end, only a new main programme had to be written, while all includes of the main simulation could be used without change. This simplified version maintenance in light of the frequent changes required to keep up with OM development.

To obtain the acceptance function of an optical module in a real experiment, it would be necessary to illuminate the module from one side and in a defined way, measure its response, then rotate the OM by a certain amount, and repeat. The main routine of the acceptance simulation had to do just that. Instead of rotating the OM, it was easier to reposition and rotate the light source. The simulation loops over the desired angles, varying the position of the light source in azimuth and elevation. At each position, it starts a run, emitting N photons distributed evenly over the cross-section of the virtual light beam. The number of impinging photons is stored for each PMT and written to disk.
All simulation parameters like number of number of photons per run, starting and ending angles, etc. are handed over via the programme call from the command line.

Figure 5.3 shows a visualisation of an early development stage, with only one PMT in the OM. The image shows the traces of one hundred photons that have been emitted in the depicted test run.

Later versions of the acceptance simulation were designed for batch processing. To get mean-

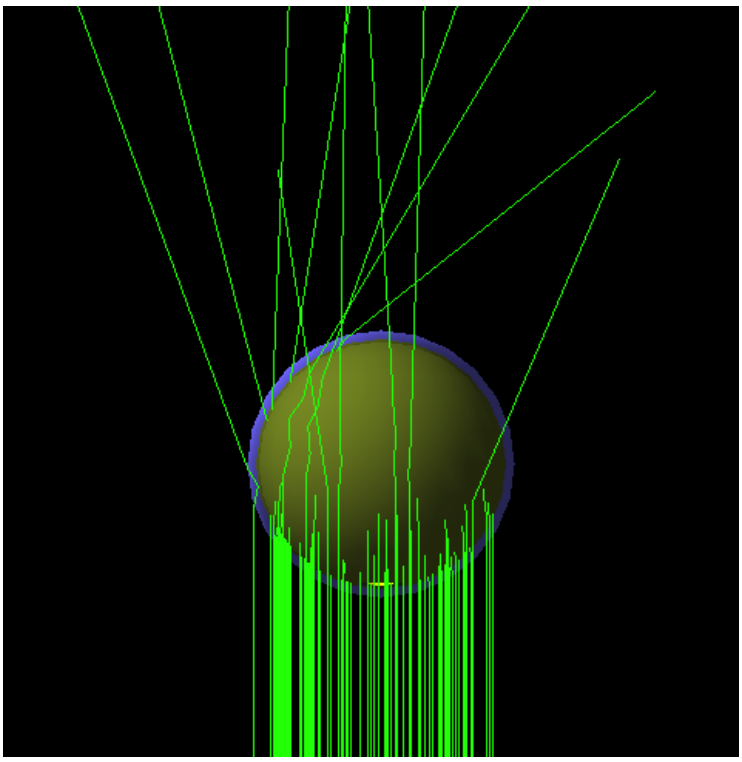

Figure 5.3: Visualisation of the acceptance simulation, showing how the virtual OM is illuminated by a parallel beam of light. The effect of the optical media boundaries is evident, with some photons being guided around inside the glass shell. As this depiction originates from a special test run, the OM only has a single photomultiplier.

ingful statistics, a data production run comprised at least 10^7 photons. Scanning the virtual OM in two dimensions therefore had to be done on one of the available computing clusters. As most simulation parameters were already handed over via the programme call, the only adaptation necessary for using the batch system was to write out the result of each orientation to its own file. The combination of the result files and the necessary calculations were done with Python scripts.

The results of the acceptance studies are detailed in section 6.1.

Chapter 6

Analysis of Simulation Data

As mentioned before, due to the ongoing development of the KM3NeT multi-PMT digital optical module, or DOM, my simulation software was constantly being updated to represent the newest hardware specifications. With each new version, the previous simulation results became more or less obsolete. Therefore, every change of the DOM design required that both ^{40}K and acceptance simulations be rerun.

From the numerous iterations, only the simulation results for the following two OM variants, called DOM and PPMDOM, are still of interest.
DOM stands for the version of the multi-PMT optical module foreseen for mass production, as of mid 2013. Three DOMs of this specification have been deployed in the first pre-production model of a detection unit (DU) in 2014.
The PPMDOM was the first deployed pre-production model of the DOM with slightly different hardware. It was operated at the ANTARES site starting April 2013 and took data until becoming obsolete by the PPM DU. Compared to the final DOM, it has smaller PMTs and different, narrower light collectors. The internal hardware differs more significantly, but those differences are irrelevant to my simulation. Table 6.1 compares those two OM versions in the simulation-relevant areas.

6.1 Results of the Acceptance Simulation

An important input parameter for detector efficiency studies at a larger scale is the sensitivity of the basic building block, the optical module. The acceptance function of the OM describes its sensitivity to light arriving from a given direction. The sensitivity is expressed as an effective area and has been calculated for each of the 31 PMTs of the OM and for the complete module.

In the simulation, photons are emitted perpendicularly from a plane, disc-shaped light source. The disc has a diameter of 432 mm, equal to the diameter of the OM sphere. The photons' starting points are homogeneously distributed over the disc's surface. In a nutshell, this creates a parallel beam of light with which the OM can be illuminated.

Simulated model	DOM	PPMDOM
Shell	17-inch glass sphere	17-inch glass sphere
PMT type	80 mm ⌀ mushroom	78 mm ⌀ cylindrical
Lens	none (shape fits sphere)	glued-on convex-concave lens
Photocathode ⌀	76 mm	74 mm
Number of PMTs	31	31
Light collector	simple Aluminium collar	PMMA (acrylic glass) with Al coating
Reflector width	12 mm	8 mm
Reflector angle	45°	45°
Model usage	PPM DU, KM3NET	prototype deployed in ANTARES

Table 6.1: Overview of the final two simulated OM versions.

The light source is placed at the desired elevation angle θ and azimuth ϕ from the point of view of the OM and oriented towards it. The number of emitted photons at each position can be chosen according to the desired statistical certainty and the available computing time.
The medium between the light source and the OM is set to unlimited transmittivity so that only absorption effects within the OM itself, i.e. within its glass and gel layers, are taken into account. The index of refraction of the medium between light source and OM is set according to the simulation reference document [5] to correspond to sea water at a depth of 3500 m (see chapter 5.3 for details).

For most acceptance studies, the simulated light was monochromatic at 2.6 eV / 477 nm. This photon energy was chosen because the Cherenkov spectrum, modified by absorption in water, has its maximum near this wavelength at around 450 nm, and the LED beacons used for the in-situ calibration of the detector emit light around 470–480 nm.

During a simulation run, every photon that reaches the photocathode of a PMT is counted. The effective area A_{eff} can then be calculated as the ratio of the number of registered photons $N_{registered}$ to the number of photons that arrived at the OM surface $N_{emitted}$, multiplied by the 2D-projected surface area of the module $A_{OM,2D}$:

$$A_{eff} = A_{OM,2D} \times \frac{N_{registered}}{N_{emitted}}.$$

This can be applied to each PMT and to the OM as a whole, by taking the sum of all registered photons. As there can be no losses between the light source and the OM surface, the divisor is equal to the number of emitted photons.

For the final results presented here, the acceptance simulation was run very finely-grained. The light source was positioned at elevation angles from 0 to 180° in steps of only 2°, and at each

elevation it was moved to azimuth angles from 0 to 58° using the same stepping. Due to the symmetry of the OM, this is all the data needed to calculate the acceptance of each PMT.
At every step, 10 million randomly polarized photons were emitted by the light source, which corresponds to a flux of 68 photons per mm^2. Over the typical surface area of a PMT, this results in a relative statistical uncertainty of less than 0.2 %.

6.1.1 Acceptance as a Function of Incidence Angle

In large scale Monte Carlo simulations, an OM is often implemented as a number of sensitive surfaces at the same spot. When the concept of the multi-PMT OM was new, the PMT surfaces were implemented as flat discs as a first approximation. For a flat surface, the effective area is proportional to the cosine of the angle of incidence. The sensitivity of each ersatz PMT were therefore weighted according to the angle between the surface normal and the impulse vector of an incoming photon.
Refraction and reflection within the glass and gel layers of the OM, and the curve of the PMT front, extend the field of view further than 90°to the each side. Later in the development of the DOM, the light collectors increased the photocathode area, leading to an effective area that is larger by a certain, slightly angle-dependent, factor.
Therefore, the simple, "flat" approximation of the PMTs greatly underestimated the effective area of the OM, and thereby the sensitivity of the simulated detector. Precise information on the effective area of the PMTs and OM was required.

The large scale detector simulations needed the effective area of a generic "PMT within an OM", given as a function of the cosine of the angle of incidence, as an input parameter. The dependence on the cosine is usually chosen because the cosine is computationally cheaper (and has to be calculated anyway), while calculating the angle from the cosine is CPU-expensive (and not necessary).

Due to the symmetry of the DOM, the downward-looking PMT 1 is the most generic one. The acceptance function of PMT 1 was used to create a table of the effective area, depending on the cosine of the incidence angle, for a generic PMT. This table was entered into the KM3NeT simulation working group reference document [5] to be used as input for detector sensitivity studies. It is reproduced in appendix A.1 as table A.8.

Figure 6.1 shows the final results of my simulations. It depicts the effective area at different incidence angles for two types of PMTs: the 78 mm type used in the PPMDOM and the 80 mm type to be used in mass production. For the 78 mm type, three variants are shown: two for the different light collecting accessories that were investigated, and one variant without light collectors for comparison.

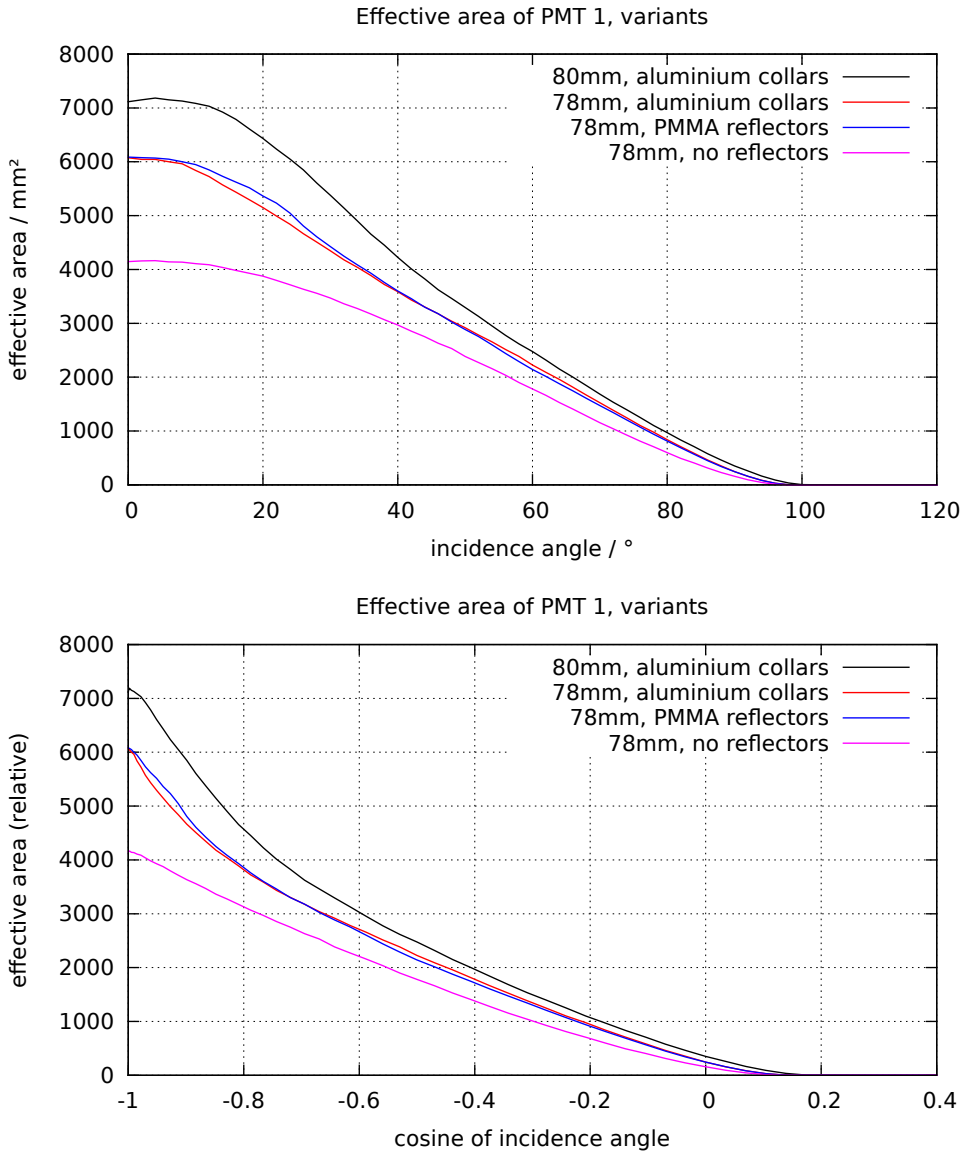

Figure 6.1: Effective area of PMT 1 for different OM configurations, given in mm^2. The projected area of the OM sphere is $r^2\pi = 146438\,mm^2$. 80 mm refers to the PMT with 80 mm diameter used in the production DOMs, where the PMTs will be equipped with aluminium collars. The other curves refer to the 78 mm PMT used in the PPMDOM, simulated with different forms of light collection rings: aluminium collars, conical rings made of PMMA with an aluminium coating, or no reflectors. The upper plot displays the effective area as a funtion of the incidence angle, where 0°means that the photon hits the PMT head on), the lower plot shows the dependence of the effective area on the cosine of the incidence angle.

6.1.2 Acceptance as a Function of Azimuth and Elevation

For my studies of the data taken with the PPMDOM, specifically the development of a probability-based direction reconstruction, I needed two-dimensional maps of the effective area of each PMT, as a function of azimuth and elevation in the frame of reference of the DOM. This information can be easily extracted from the simulation data as described above.

The resulting maps are shown in figure 6.2 as heat maps. The effective area of the OM or PMT for light coming from a given direction is color coded and displayed relative to the projected geometrical area of the OM of 146438 mm^2. Elevation runs from -180°, straight down, to 0°, straight up.

The effective area of the complete optical module is almost perfectly uniform along the azimuth, as figure 6.2(a) nicely shows. Furthermore, it is obvious how wide the field of view of the multi-PMT optical module is: The sensitivity to light coming from straight above only drops to about one third of the maximum sensitivity.

Figure 6.2 also shows the acceptance of single PMTs in the DOM. The acceptance of PMT 1 is presented in figure 6.2(c). As expected, it is uniform along the azimuth. Along the elevation angle, the dependence is the same as the dependence on the incidence angle for the single PMT shown above.
Illustration 6.2(d) is an enlargement of the "blind" area of PMT 1, showing that a minuscule fraction of photons arriving from the opposite side of the OM can reach a PMT. The pattern visible is caused by the different probability of successful multiple reflections, depending on the path of the photon. If a photon trapped within the glass and gel layers arrives at a photomultiplier, it is more likely to penetrate into the PMT glass than to be reflected again, because the difference between the refractive indices is verly low.

6.1.3 Acceptance as a Function of the Wavelength of the Photons

In order to compare the idealised aluminium reflector with the real one used in the PPMDOM, a number of sensitivity simulations were run with the light source at a fixed position at an elevation angle of $\theta = -180°$, below the OM. The wavelength of the incoming photons was varied from 290 to 720 nm in steps of 5 nm. 10^8 photons were emitted at each simulated wavelength.

PMMA becomes opaque at shorter wavelengths. Lacking information on the actual parts, data from a measurement by C. Joram [9] on a 2 mm thick piece of Plexiglass were used in the simulation. The absorption length was derived from the relative intensity according to $I(d) = I_0 e^{-\kappa d}$, where I(d) is the remaining light intensity after traversing the distance d of the absorbing medium, and κ is the coefficient of extinction. Taking into account the four times longer optical path in the PPMDOM reflectors compared to the measured sample, one expects the cut-off (half intensity) point at around 390 nm.

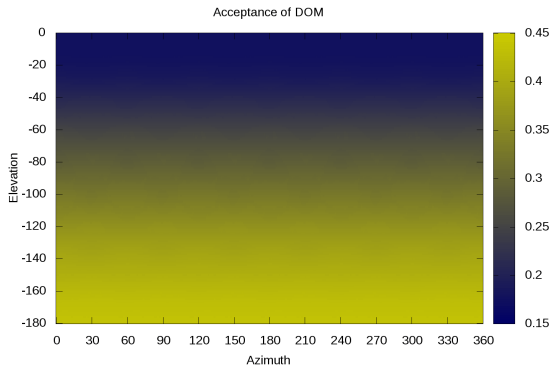

(a) acceptance of the DOM

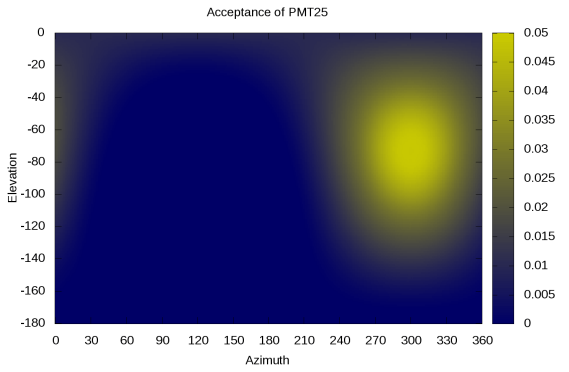

(b) acceptance of PMT 25

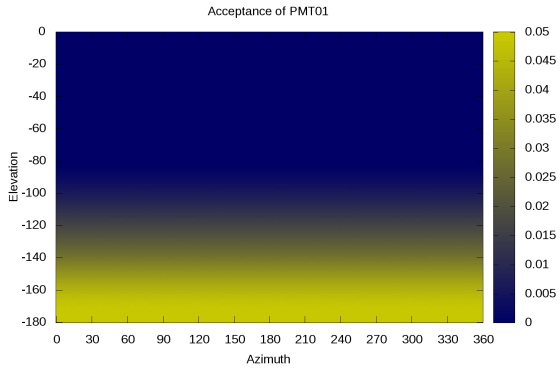

(c) acceptance of PMT 1

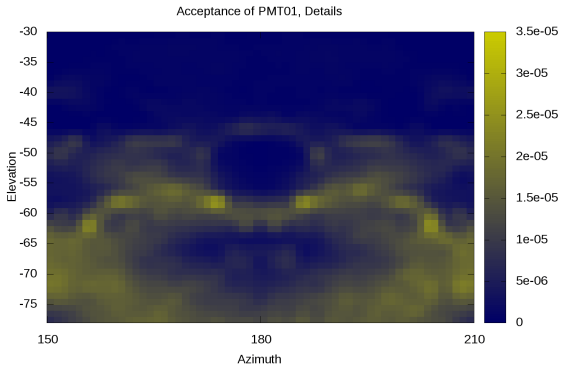

(d) details of acceptance, PMT 1

Figure 6.2: Acceptance functions of the DOM as a whole and a few example PMTs as heat-maps, displayed in spherical coordinates in the frame of reference of the optical module. The effective area at each incidence angle is color-coded in fractions of the geometrical area of the DOM of 146438 mm^2. Figure 6.2(d) shows that a minuscule fraction of photons arriving from the opposite side of the OM can reach a PMT. One can see some interesting "space invaders"-shaped structures that stem from photons that get reflected multiple times until they reach the photocathode on the opposite side of the module from PMT 1. Photons that encounter another PMT along the path within the glass and gel layers are likely to hit that PMT, while photons traveling along the gaps between PMTs are likely to be reflected.

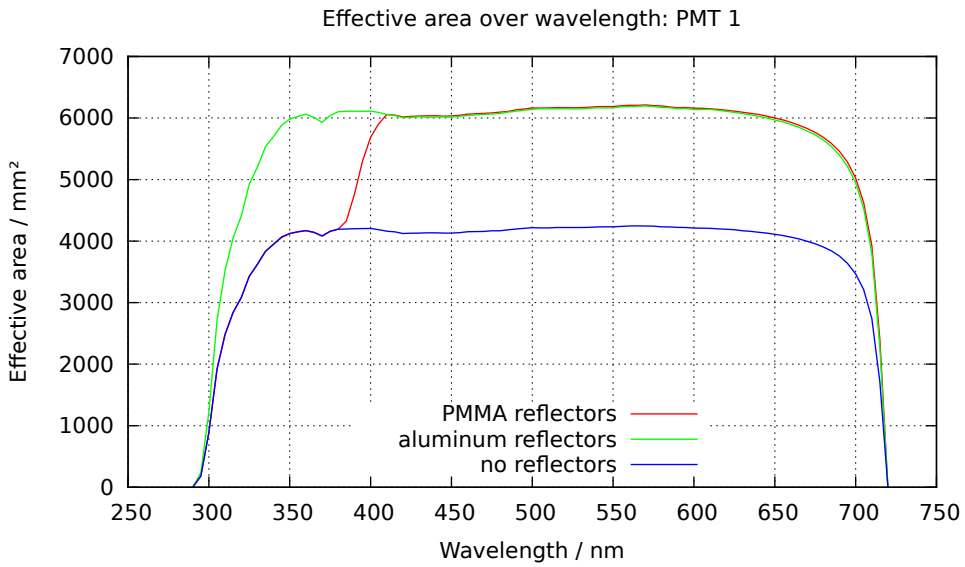

Figure 6.3: Wavelength dependence of the effective area of the PMT/reflector combination. The back-coated PMMA reflectors become ineffective in the short wavelength regime below 400 nm. The simulated reflecting collars made from aluminium sheet are therefore preferable.

The result is shown in figure 6.3. The expected cut-off at wavelengths below 400 nm is evident. This is bad for at least two reasons. The quantum efficiency of bialkali PMTs has its maximum between 350 and 400 nm (compare figure 6.6). And while the photon spectrum of Cherenkov light, modified by the absorption characteristics of the sea water, has its expected maximum at a wavelength 450 nm (see figure 6.8), about one quarter of the expected Cherenkov photos have a wavelength of shorter than 400 nm. For this fraction of incoming light, the effective area gain from the reflectors would be lost due to absorption within the PMMA.

At wavelengths longer than the cut-off, PMMA reflectors and solid aluminium reflectors perform equally well. Due to the simpler, cheaper construction, collars made from aluminium sheets should be the preferred solution for the production DOMs.

6.2 Results of the ^{40}K Simulation

The initial task of this thesis was the simulation of the background light caused by decays of ^{40}K nuclei in sea water. The simulation had two goals: To predict the total background rate, meaning the rate at which the PMTs of an OM get triggered by ^{40}K induced Cherenkov light, and to examine coincidence rates and hit patterns.
Single photons reaching the OM from ^{40}K-decays both near and far add to the dark rate of each PMT in a timely constant manner, and are by themselves indistinguishable from other background noise. Photons from near decays often coincide in several PMTs and create a hit pattern that can be distinguished from the constant background.

For a realistic simulation of the total background rate, it is imperative to choose a large enough size for the simulated environment. If the size of the world volume, the sea water, is too small, the background rate will be underestimated. On the other hand, picking too large a volume will greatly increase the processing time needed for a reasonable statistical sample, because only in a small fraction of the simulated events will photons reach the OM.
In a number of trial runs, a radius of the world volume of about three times the maximum absorption length (67.5 m at 440 nm) has been established as a reasonable compromise, as shown in figure 6.4. Therefore, the simulated environment for the determination of the total rate is a sphere with a radius of 200 m.
The rates shown in figure 6.4 stem from the first, crude, OM model and are obsolete as absolute values. However, the relative dependence of the total background rate on the world radius is of course valid, regardless of the exact shape of the simulated OM.

The rate of random coincidences caused by ^{40}K can also be extracted from this data, or deduced from the calculated total background rate. Let R_{OM} be the total hit rate of the OM caused by ^{40}K, $R_{PMT} = \frac{1}{31} \times R_{OM}$ the average hit rate of a single PMT, and Δt_c the length of the coincidence window. The rate of double coincidences $R_{2\times}$, meaning events where first one and then another PMT is triggered within the duration of the coincidence window, is then calculated by

$$R_{2\times} = R_{OM} \times 30\, R_{PMT} \times \Delta t_c.$$

Coincidences within the same PMT are excluded, because the recovery time, the time span until a PMT can register another photon after having been triggered, is longer than the usual coincidence window of ≤ 20 ns. Details can be found in chapter 7.

Similarly, the rate of three-fold coincidences from a random background can be expected to be

$$R_{3\times} = R_{OM} \times 30\, R_{PMT} \times 29\, R_{PMT} \times 0.5 \Delta t_c^2,$$

and so forth for higher levels of coincidence. These rate calculations and their error estimation for a random background hypothesis are detailed in the appendix B.2.

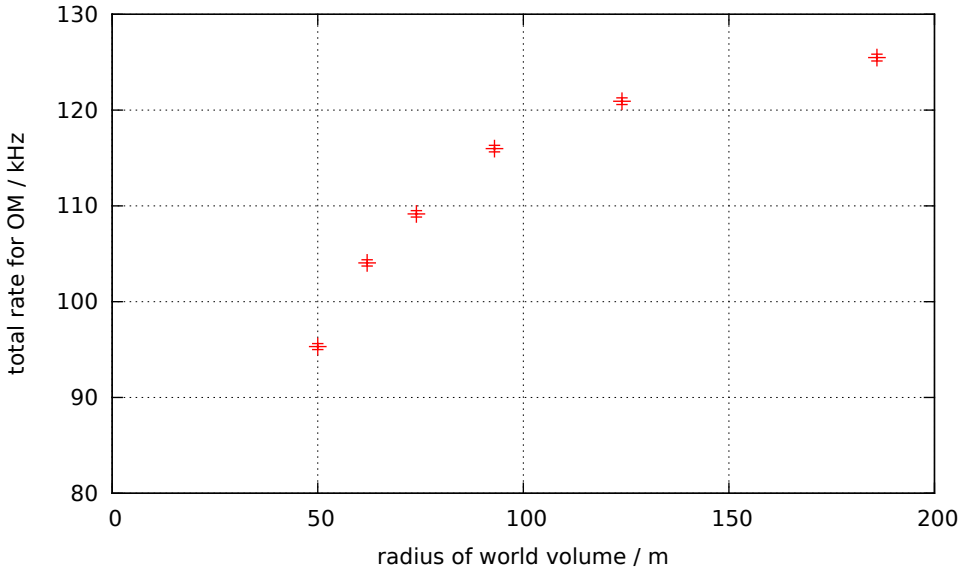

Figure 6.4: Depiction of the total background rate in the OM depending on the size of the world volume, created with the first version of the ^{40}K simulation. The data has been created with a series of simulation runs with the goal to find the best compromise between accuracy and CPU time. It is evident that an increase of the world size beyond a radius of 200 m would only marginally improve the quality of the prediction.

Coincidences from ^{40}K are far from purely random, however. Most ^{40}K coincidences are caused by decays close to the OM (closer than 6 m), so that several photons from a single ^{40}K decay reach the optical module at the same time. In order to get good statistics on these events, another set of simulations was run using a world size of 10 m. Of special interest are the typical spatial distribution incoming photons created in one decay, the number of photons and the relative arrival times. These pieces of information can only be established by a detailed simulation.

6.2.1 Parameters for Simulation and Analysis

Environment

The environmental parameters, absorption length, scattering length, and index of refraction, were taken from the simulation reference document and are reproduced in figure 6.5. A table of their exact values can be found in the appendix on page 120. These values have been used by the GEANT 4 simulation to calculate the creation and propagation of Cherenkov photons.

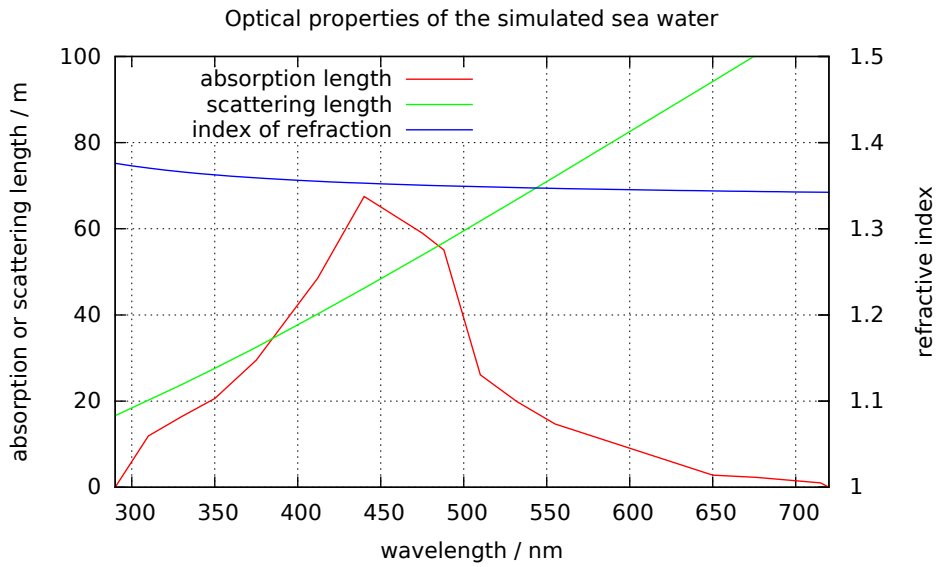

Figure 6.5: Absorption and scattering lengths and index of refraction of the simulated sea water, taken from [5].

Detection Efficiency

The detection efficiency of a PMT is the probability that a photon causes a measurable electrical signal, as described in 2.5. This characteristic is a wavelength-dependent combination of quantum efficiency and collection efficiency.

The collection efficiency varies with the impact position and angle of incidence of the photon. This is a small effect that also depends on the orientation of the PMT relative to the Earth's magnetic field (and with that, on the rotation of the PMT along its longitudinal axis within its mounting point in the OM), on the homogeneity of the photocathode, and on the voltage between photocathode and dynode. A constant value of 0.9 is used in the simulation, in accordance with KM3NeT design specifications for PMTs and the simulation reference document.

The quantum efficiency to be used in the analysis was also defined in the reference document and is based on numerous precision measurements at the ECAP. It is shown in figure 6.6 and tabulated on page 122 in the appendix.

6.2.2 Analysis Method

As described, the output of the GEANT 4 simulation is a sequence of events. If during an event, meaning a simulated ^{40}K decay and everything that happens related to it, one or more photons reached a PMT of the OM, these photons are listed, along with their properties and especially their arrival times relative to the event start. From this list, a timeline has to be generated, which has to contain a sequence of PMT hits and the time of each hit. This resembles the

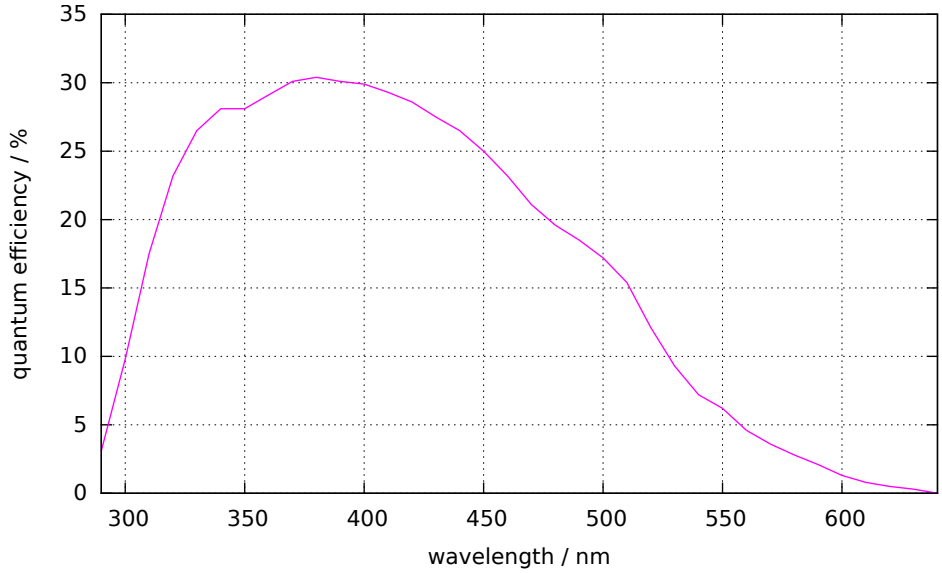

Figure 6.6: Quantum efficiency of the simulated PMTs as used in the analysis, taken from [5].

shape of the data delivered in real time by a neutrino telescope.

First, the elapsed time $T_{elapsed}$ that corresponds to the number of simulated events has to be calculated, which follows from the volume of the simulated sea water V_{world}, the number of events N_{events} and the activity of ^{40}K in sea water A_{K40}:

$$T_{elapsed} = \frac{N_{events}}{V_{world} \times A_{\mathrm{K40}}}.$$

The assumed activity of ^{40}K in sea water is 13 kBq per m^3. So if e. g. the simulated volume measured 10 m^3, a simulation run of 130,000 events would correspond to a real time of one seconds.

Next, the ^{40}K decay events are randomly distributed over this timespan. Each event gets a starting time between 0 and $T_{elapsed}$. The flight time of each photon is added to this starting time to get the arrival time of the photon at the PMT. The arrival time and the PMT that has been hit is then entered into the timeline.

The next step in the analysis is to go through that raw timeline. For each photon, the quantum efficiency (at the photon's energy) and collection efficiency are applied to randomly choose whether it is registered. If it is, the time and PMT number of that effective hit is added to another timeline, which only contains the effective hits. This finally produces a time sequence of triggered PMTs, similar to the data stream coming from a real detector.

Two things to note here: Firstly, as after applying quantum efficiency only a small fraction of the photon hits are used, the statistics can be "cheaply" (in terms of CPU time) improved by

reusing the simulated events. This is achieved by multiplying the real time with a factor n and assigning each event n random start times in the timeline.
Secondly, there are a number of additional PMT and electronics properties that could be included in the generation of effective hits, like transit time spread, directional effects of the collection efficiency, or creating a charge quantity as output. For the initial understanding of ^{40}K signals, adding these random events would only have blurred the results and added no information. In later simulation runs, when concrete technical data about the DOM hardware was available, adding these minute details might have lent a bit more realism to the simulation, but since the time blurring effect of the TTS is much smaller than the coincidence window, introducing a random time shift for each PMT hit would not change much, if anything, in the results.
One real life effect that had to be included in the analysis is the dead time of the PMT after it was triggered. Two independent photons registered in the same PMT within a few tens of nanoseconds of each other would create a longer signal, but could not easily be identified as two unique photons. Therefore, photons that arrive at a PMT within 32 ns after that PMT has last been triggered are discarded.

The timeline of effective hits is then analysed by applying a sliding coincidence window to the timeline, with the goal to extract coincidence rates and hit patterns. For this purpose, counting variables for all possible PMT pairs are prepared, as well as for the frequency of each coincidence level and for the number of photon hits in each PMT.
To find coincidences, the analysis programme iterates over all hits of the timeline. When the first PMT is hit, a coincidence search is triggered and the time of the hit that triggered the search is noted. The programme scans the following hits until the time difference to the first hit of the current search is longer than the coincidence window of 10 ns. This first photon that lies outside the coincidence window will be the starting point of the next coincidence search.
For every PMT that has been hit in the "coincidence" event, the counter of the number of hits of that PMT is increased. If more than one PMT has been hit in the investigated "coincidence" event, then the counter for the appropriate n-fold coincidence is also increased. From these counters, the average rate of each PMT is calculated and the frequencies of twofold, threefold and higher coincidences are calculated.
Furthermore, for each twofold or higher coincidence, the first two PMTs that have been hit are determined, and the counter for this PMT pair is increased. This allows to analyse typical hit patterns with regard to the distance between PMTs that are triggered in coincidence. As most coincidences are twofold, it is sufficient to consider only these in detail. The hit patterns of higher level coincidences have been studied with similar results as described below for twofold coincidences.

6.2.3 Quality Checks and Miscellaneous Information

Quality checks of the generated data are necessary to make sure that the results are not falsified by programming errors in the simulation or analysis software, or by peculiarities of the simulation framework.

For the acceptance simulations, sanity checks of the results were relatively easy. The expected shape and magnitude of the acceptance function is known beforehand as a good approximation, and the effects of changes in the OM design can also be estimated.

In contrast, the ^{40}K simulation has a large number of input parameters and simulated physical effects that influence the results. Lacking detailed calculations of the expected rates, the results of the simulation, as well as intermediary data, had to be checked for consistency and plausibility.

Intermediary data is data that is generated in one of the internal steps of the simulation, but does not appear in the end result. Among the data that can be extracted from the internals of the simulation are the relative frequency of the decay channels, the energy spectrum of the generated β-radiation, the distance travelled by the electrons, the number of emitted Cherenkov photons per decay, and the photon spectrum.
In each version of my simulation, these statistics have been extracted and thoroughly compared to theoretical predictions or other simulations, like those described in ANTARES Internal Note ANTARES-PHYS-2008-001 [11].

In the final data, one obvious criterium for a sanity check is the number of hits per PMT. This information can easily be summed up by scanning through the raw data file. As there are no shadowing effects (as opposed to the real-world PMDOM with its holding structure), every PMT should receive the same number of photon hits, within the expected statistical fluctuation.
Another quality check, which shows whether the chosen size of the world volume was sufficient, is to plot the number of arriving photons versus the distance of the associated ^{40}K decay from the OM. There should be not cut-off, meaning that from the distance corresponding to the world radius, only few photons should arrive at the OM.
Figure 6.7 contains example graphs of these two statistics that can be readily extracted from the raw simulation data.
Further information that may be of interest for the development of a neutrino telescope is the spectral composition of the Cherenkov light that arrives at the optical modules, especially in light of the custom PMT development taking place for KM3NeT. Figure 6.8 shows the spectrum of the arriving Cherenkov light for a simulation run with a world radius of 200 m. Compared to the quantum efficiency used for the analysis (cf. figure 6.6), it is obvious that the peak is at a longer wavelength than is ideal for standard bialkali PMTs. That is the reason why the PMT manufacturers have been imposed minimum requirements for the quantum efficiency of 18 % at a wavelength of 470 nm. A higher PMT sensitivity in the wavelength range of 400 to 450 nm will increase the photon yield and therefore improve the sensitivity of the detector.

6.2.4 Single Photon Rates

The obtained single photon rates from the final simulation runs are listed in table 6.2. The single rate over a simulation run is calculated from the number of registered photons hitting each PMT and the run length in real time. It can be obtained immediately from the timeline of effective hits, as described above.

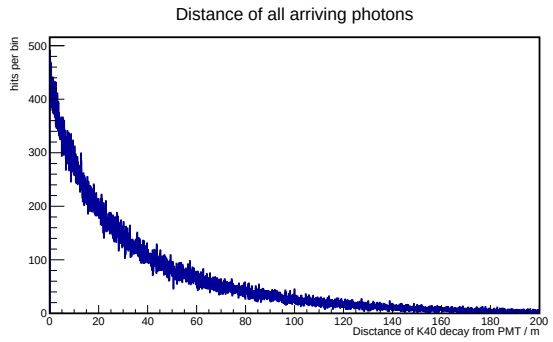

(a) photons over distance, PPMDOM

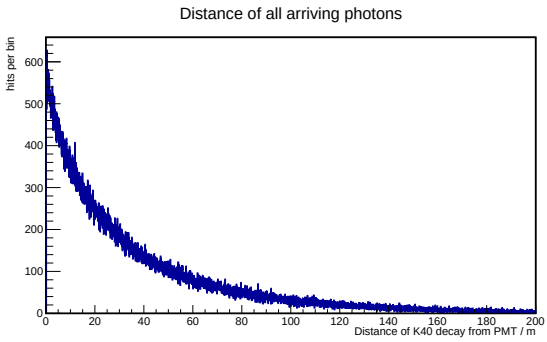

(b) photons over distance, DOM

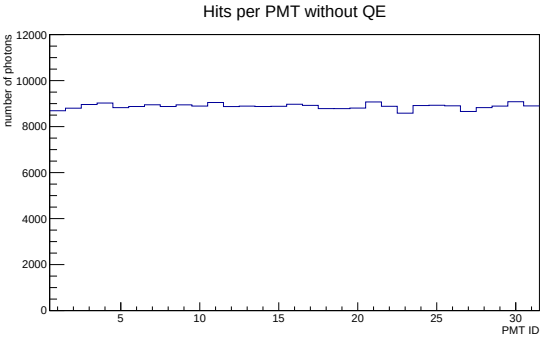

(c) photons per PMT, PPMDOM

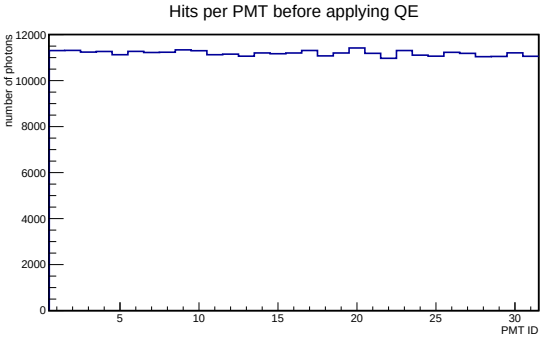

(d) photons per PMT, DOM

Figure 6.7: Data quality statistics for the final simulation runs using the PPMDOM and the DOM configurations, respectively, with a world size of 200 m. Graphs 6.7(a) and 6.7(b) show the number of photons that arrived at the OM depending on the distance of the associated ^{40}K decay. Figures 6.7(c) and 6.7(d) show the number of photons that hit each PMT. All values are raw photon counts in the unprocessed data, without applying quantum efficiency.

The single photon rates are proportional to the effective area of the OM. Therefore, the single photon rate registered by the DOM is expected to be about 20 % higher than the rate of the PPMDOM, judging by figure 6.1. The larger difference observed can be explained by the loss of sensitivity of the PMMA-based reflectors used in the PPMDOM, as shown in figure 6.3.

World size	DOM	PPMDOM
10 m	32.4 ± 0.01 kHz	23.8 ± 0.01 kHz
200 m	128.2 ± 0.1 kHz	97.1 ± 0.1 kHz

Table 6.2: Overview of the single photon rates from ^{40}K.

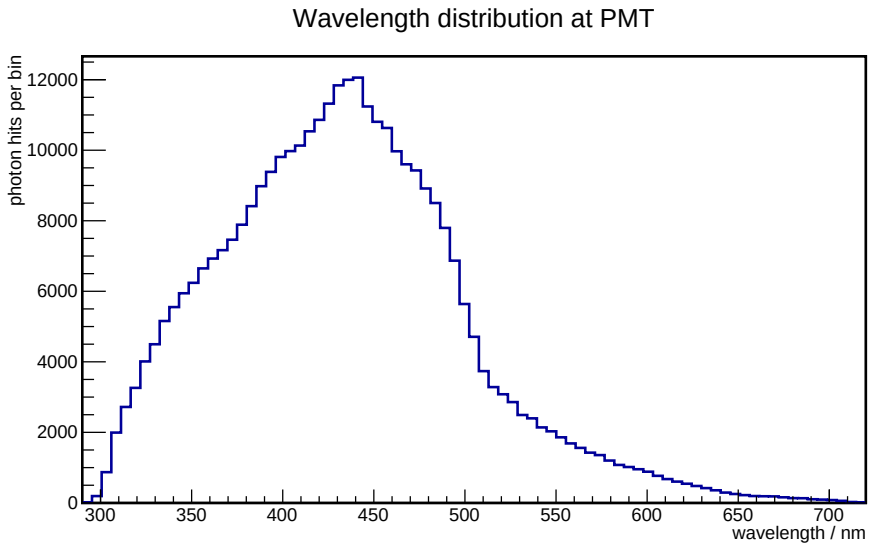

Figure 6.8: Wavelength spectrum of the Cherenkov light reaching the optical module, from the simulation run with DOM configuration and a world radius of 200 m.

6.2.5 Coincidences

Knowing the rate, multiplicity and hit pattern of coincidences caused by ^{40}K allows to better suppress this background signal in the future detector.

In the finalized neutrino telescope, real time data filters will decide, based on coincidences, whether an actual event has occurred, and try a reconstruction of the event (as a muon track or bright spot) if certain criteria are met. So the fewer "false alarms" the initial filters trigger, the better the quality of the resulting data will be, and the less CPU time and storage capacity will have been wasted on false signals. On the other hand, it is just as undesirable to discard actual neutrino events because they have been wrongly identified as background.

Exact knowledge of the ^{40}K signature allows to optimize the online data filtering, and therefore improve the overall efficiency of the detector. Additionally, ^{40}K background can be used for intra-OM time calibration, which I applied to PPMDOM data and describe in chapter 7.

Expected Rates for Random Background Hypothesis

The expected coincidence rates can be calculated for the hypothesis that the photon background from ^{40}K decays is completely random in space and time. Table 6.3 contains these calculated coincidence rates, based on the PMT hit rates gathered from the simulations of the DOM and the PPMDOM with a world radius of 200 m.
This clearly shows that purely random quadruple and higher coincidences are completely negligible. Within the simulated time span, only one triple coincidence would be expected, and no higher level coincidences. This result will be compared to the analysis of the timeline created

Event	DOM	PPMDOM
Number of hits	1098454	867002
Simulated time	8.563 s	8.917 s
Single photon rate	128.2 ± 0.1 kHz	97.2 ± 0.1 kHz
Double coincidence rate	159.2 ± 1.6 Hz	91.5 ± 1.1 Hz
Triple coincidence rate	95.5 ± 1.5 mHz	41.6 ± 0.7 mHz
Quadruple coincidence rate	27.7 ± 0.6 µHz	9.1 ± 0.2 µHz
Quintuple coincidence rate	3.87 ± 0.10 nHz	0.97 ± 0.03 nHz

Table 6.3: Overview of the hypothetical coincidence rates, calculated from the number of PMT hits in the final ^{40}K simulation runs with a world size of 200 m. The coincidence calculations are based on a random background hypothesis.

from the simulation data.

Definition of Local and Global Coincidences

Local coincidences are coincidences caused by a single ^{40}K decay. Global coincidences also include random coincidences that are caused by photons from several separate decays.

Result of my Simulations

The principal result is that most ^{40}K coincidences are caused by photons originating from the same decay. They photons registered in the PMTs of the OM therefore show strong correlation in space and time. From geometric consideration immediately follows that a large fraction of the detected coincidences has to be caused by decays in close proximity to the OM. The truly random component of the ^{40}K background only makes up a small fraction of the single photon background rate. Consequently, most coincident photons

- arrive within a time window of about 1 ns,
- originate from a small volume around the OM, and
- hit the same side of the OM, meaning that the distance between triggered PMTs is less than 90°.

Due to the short distance that the β radiation emitted by ^{40}K travels in the water (less than 1 mm), Cherenkov photons causing local coincidences originate from virtually the same point and are emitted at the same time. The arrival time difference between the individual photons is therefore mainly a function of the distance between the decay vertex and the impact point on the OM. The maximum difference between the distances that coinciding photons travel to their respective impact points is approximately equal to the radius of the OM. From the speed of light in water, about $22 \frac{\text{cm}}{\text{ns}}$, it is clear that the maximum time difference for a local coincidence

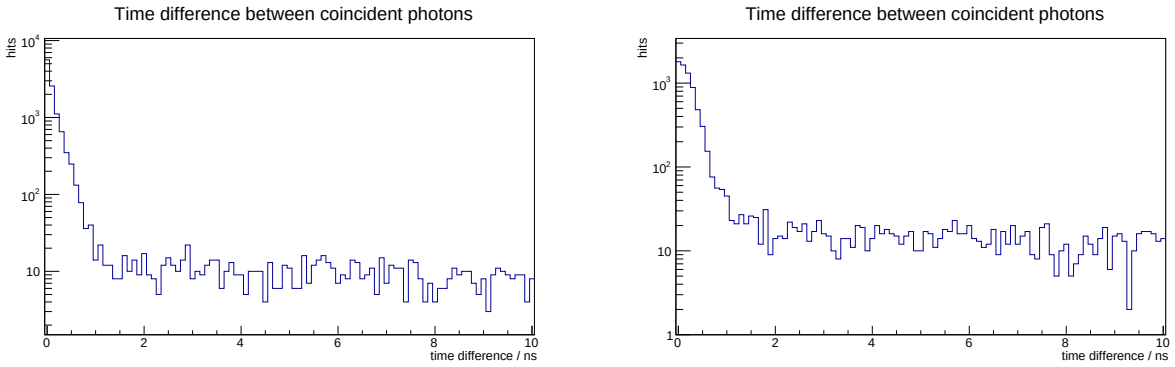

(a) PPMDOM (b) DOM

Figure 6.9: Time difference between the first photon and the second photon of each coincidence event and each further photon, for all events of the simulation runs with a world size of 200 m. The PPMDOM configuration is shown on the left, the DOM configuration on the right. Local coincidences cause the peak at 0 ns; the constant number of hits per bin for time differences greater than 1 ns originate from the purely random coincidences caused by non-local decays.

is about 1 ns.

The small random component of the coincident ^{40}K background consists of photons from multiple decays that arrive within the 10 ns coincidence time window. The photons of these random coincidences have no correlation and can therefore arrive at opposite sides of the OM, which will make them easy to filter out in the detector. The arrival time can differ by up to the length of the coincidence window, and will be distributed evenly within that window.

Figure 6.9 shows a histogram of the time difference between the first and the second photon of each coincidence for the final simulation runs of the PPMDOM and DOM configurations. It clearly shows the expected peak at 0 and a steep decline until 1 ns. During the remaining coincidence window, the distribution is flat (within statistical variations).

The distances travelled by coincident photons are analysed in figure 6.10. The histograms on the left-hand side show local coincidences only, the ones on the right show all coincidences. It is evident that the majority of locally coincident photons arrive from decays that happened within 5 m around the optical module. Including all coincidences does not noticably change the distribution for short distances, but only adds a smaller number of events that mostly originate from distances larger than 5 m.

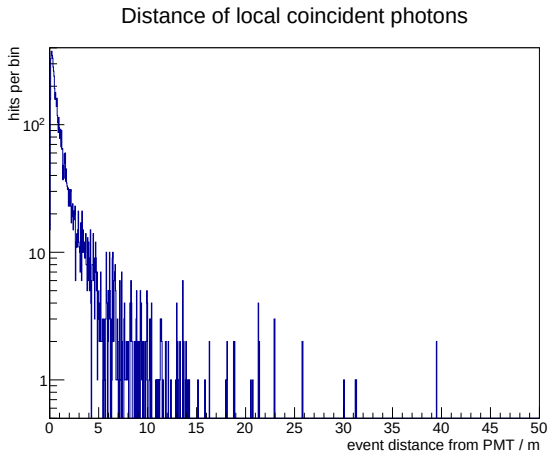

(a) PPMDOM, local coincidences

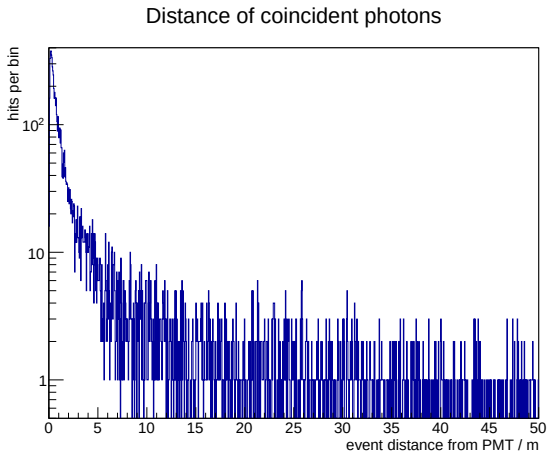

(b) PPMDOM, global coincidences

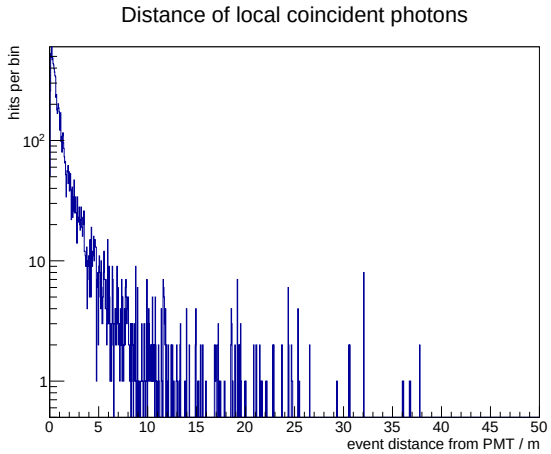

(c) DOM, local coincidences

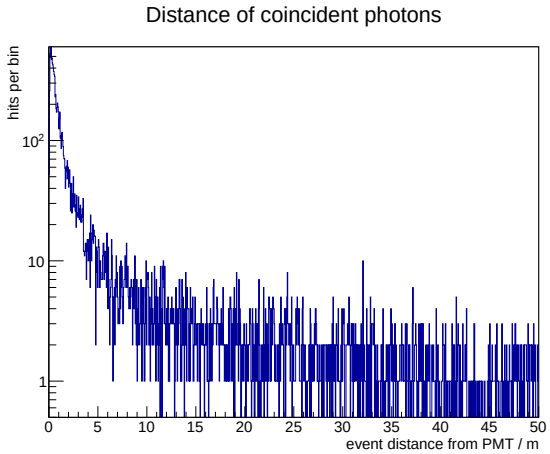

(d) DOM, global coincidences

Figure 6.10: Histograms of the distance travelled by each photon that was part of a coincidence event. The upper histograms show the results of the simulation of the PPMDOM, the lower ones show the DOM results. The figures on the left show local coincidences only, in the ones on the right all coincidences are included. The world radius was 200 m.
The results show that local coincidences are caused chiefly by decays within a 5 m radius around the OM, while random coincidences usually have their origins beyond this distance.

If most coincidences are caused by photons from the same decay, it is logical that their photons impinge on the same side of the OM. Those PMTs that face the decay the most directly have the highest probability to be hit by a photon. To show how the photons of a coincidence are spread over the OM surface, figure 6.11 contains histograms that depict the distance between the PMTs that were part of a coincidence. For each PMT that was triggered in an event, the distance to every other triggered PMT, in the shape of the angle between the two PMTs' axes,

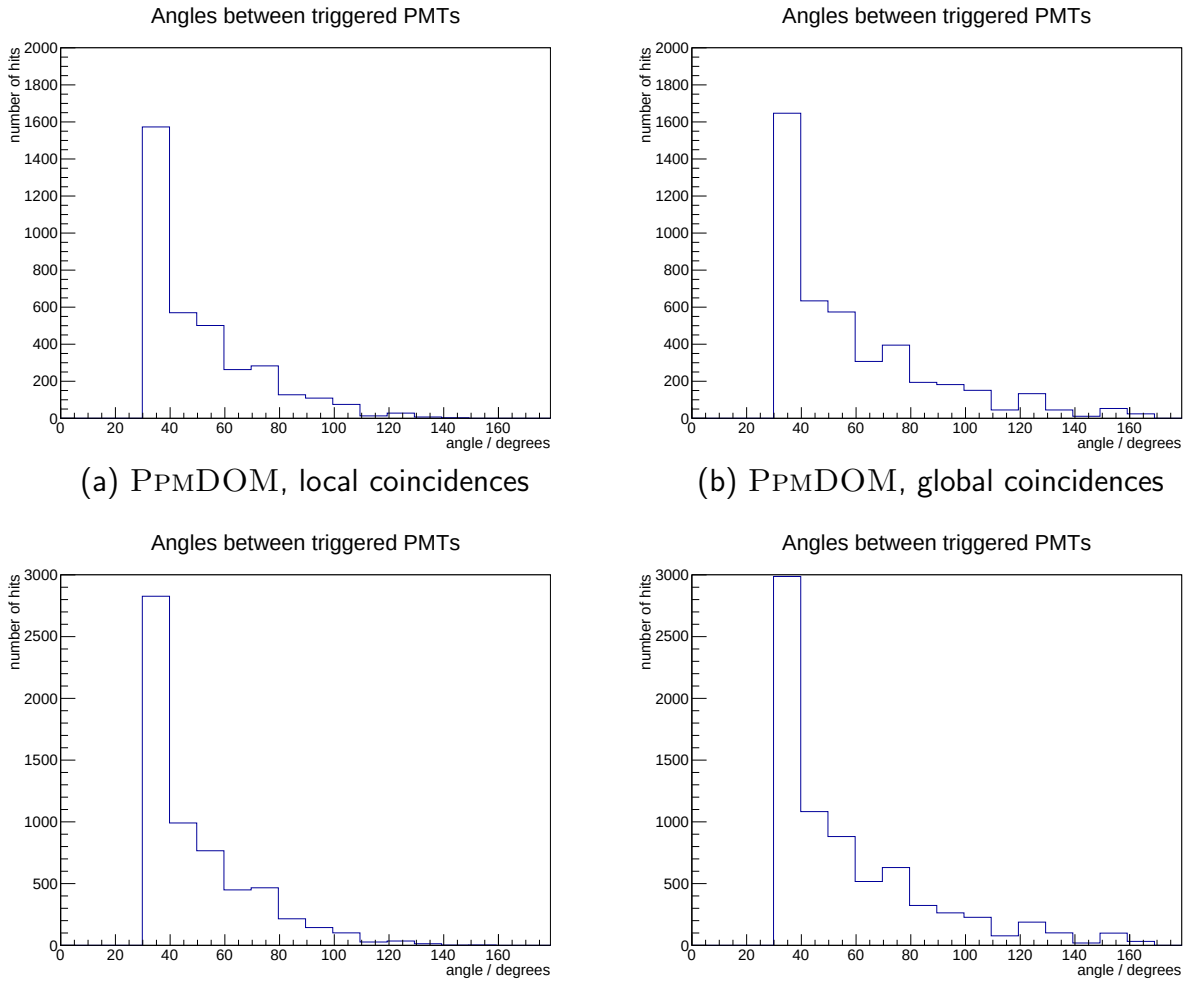

(a) PPMDOM, local coincidences

(b) PPMDOM, global coincidences

(c) DOM, local coincidences

(d) DOM, global coincidences

Figure 6.11: Histograms of the distances between the triggered PMTs of a coincidence event. The upper histograms show the results of the simulation of the PPMDOM, the lower ones show the DOM results. The figures on the left show local coincidences only, in the ones on the right all coincidences are included. The world radius was 200 m.
The distance is given as the angle between the axes of two PMTs. For each event, this angle is entered into the histogram for all possible pairings among the PMTs that were triggered. The smallest distance between two PMTs is 32°.

was calculated and entered into the histogram.

The distances between directly neighbouring PMTs fall into the 30 – 40° bin. The simulation result show that the majority of PMTs that are triggered in a local coincidence are direct neighbours. To complete the image, figure 6.12 shows that the vast majority of coincidences are twofold. The typical signature of ^{40}K decays can therefore be described as two neighbouring

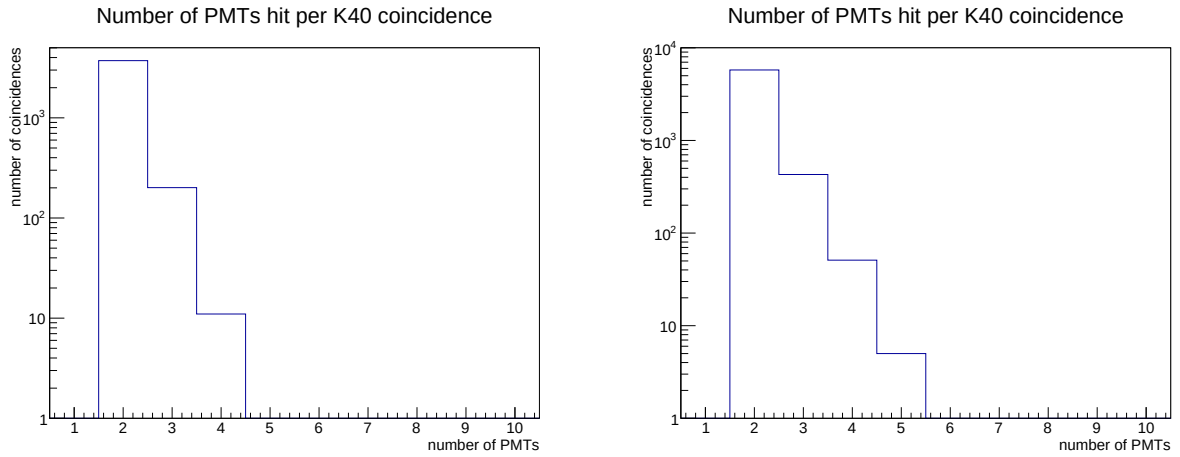

(a) PPMDOM (b) DOM

Figure 6.12: Number of triggered hits per ^{40}K coincidence. For both OM types, twofold coincidences dominate. Shown here are global coincidences from the 200 m data sets.

PMTs hit in coincidence within a time window of 1 ns.

A slightly different representation of the relationship between PMT distance and coincidence rate is shown in chapter 7 in figure 7.17. It compares data from the simulation with actual data from the PPMDOM.

Coincidence rates from the simulation

In analogy to table 6.3 above, table 6.4 lists the rates of the different coincidence levels, and the number of occurrences of each, gathered from the simulation data.

The information about the likelihood of each coincidence level will be important for the studies of the deep-sea data of the PPMDOM, concerning the differentiation of actual events (muons, neutrinos, calibration light sources) from the ^{40}K background.

During the development of KM3NET, a figure often requested as a result of my simulations was the L1 rate, meaning the rate of level 1 triggers. An L1 event in this context was defined as at least 2 L0 hits within 10 ns, and an L0 hit was defined as a PMT event with an anode charge of at least 0.3 times the typical single photoelectron charge. In other words, the L1 rate is the sum of the coincidence rates listed in table 6.4. The L1 rates for both OM variants are shown in table 6.5. As defined before, global coincidences are coincidences caused by photons from one single ^{40}K decay, while global coincidences additionally include random coincidences. The random component of the ^{40}K background is the difference between these two figures, and is consequently, in good approximation, equal to the coincidence rate calculated for the random background hypothesis (compare table 6.3).

Event	DOM	PPMDOM
Number of hits	1098454	867002
Simulated time	8.563 s	8.917 s
Single photon rate	128.2 kHz	97.2 kHz
Double coincidence rate	664 Hz	419 Hz
Number of double coincidences	5686	3734
Triple coincidence rate	49.5 Hz	22.5 Hz
Number of triple coincidences	424	200
Quadruple coincidence rate	5.8 Hz	1.7 Hz
Number of quadruple coincidences	50	15
Quintuple coincidence rate	0.6 Hz	0.1 Hz
Number of quintuple coincidences	5	1

Table 6.4: Overview of the coincidence numbers and rates gathered from the final ^{40}K simulation runs with a world size of 200 m. The top figures represent the total number of photons that have been registered, the simulated time is the equivalent real time duration of the respective data sets. As described and shown above, local coincidences vastly increase the coincidence rates above what would be expected from a random background. Coincidence levels higher than three, which one would not expect in a random data set of the simulated lengths of just under 9 s, are rather commonly caused by local ^{40}K decays. This has implications for real life data filtering and triggering schemes.

Event	DOM	PPMDOM
Single photon rate	128.2 ± 0.1 kHz	97.2 ± 0.1 kHz
Local coincidence rate	564 ± 6 Hz	347 ± 8 Hz
Global coincidence rate	720 ± 8 Hz	443 ± 8 Hz
Random coincidence rate	156 Hz	96 Hz
Calculated random rate	159 Hz	92 Hz

Table 6.5: Overview of the L1 coincidence rates caused by ^{40}K from the final simulation runs with a world size of 200 m. In the lower section, the random component (coincidences caused by different decays) from the simulation is compared to the calculated random background rates that results from the PMT hit rates and the coincidence window.

6.2.6 Summary

My simulations have predicted the PMT single photon trigger rates, as well as the rates and the typical signature of coincidences, caused by ^{40}K decays in the deep sea. Two types of multi-PMT OMs were investigated: the PPMDOM, whose real life data will be analysed in

the next chapter, and the DOM, which will be the OM type to be used in the final detector.

For the PPMDOM, the total trigger rate induced by photons created by ^{40}K decays will be around 97 kHz, or 3.1 kHz per PMT. Coincidences caused by a single decay ("local coincidences") will occur at a rate of around 350 per second. Another 96 Hz of coincidences from random coincidences will add to the background.
In the DOM, the total trigger rate will be higher at 128 kHz, equalling 4.1 kHz per PMT, due to the larger PMTs and light collectors. Consequently, the coincidence rates will be significantly higher, at 564 local coincidences and a further 156 random coincidences per second.
These trigger rates are listed in table 6.5.

The typical signature of ^{40}K decays in close proximity to the OM (less than about 5 m distant) is a twofold, rarely threefold coincidence in neighbouring PMTs within a time span of 1 ns. Higher coincidence levels will also occur, at a rate of a few Hertz.
Random coincidences are correlated neither in time nor in space. The triggered PMTs can be in any distance to each other, and the time span between the photon arrivals will be random between 0 and the length of the coincidence window. The expected rate for triple coincidences is already below 0.1 Hz, higher level random coincidences are increasingly less likely and will not play a role in data taking.
Table 6.4 lists the coincidence rates for the different levels. The spatial relationship of coincident photons is shown in figure 6.11.

Due to the described properties, the ^{40}K background offers an approach to calibrate the optical module in situ. The near-zero time difference between ^{40}K photons allows to measure the time offset between PMTs and compensate for it (see section 7.2.2). As most coincidences are caused by a single photon in two PMTs[1], a charge calibration using ^{40}K coincidences is possible.

[1]For comparability with the deep-sea data shown in the next chapter, the here presented analysis of the simulation data included some of the technical restrictions of the real-world OM, especially the dead-time that would make it impossible to distinguish two photons arriving shortly after each other. The simulation data has also been investigated ignoring these restrictions. Those studies have shown that in the vast majority of coincidence events, each triggered PMT has been hit by exactly one photon.

Chapter 7

Data from the Deep Sea

The redeployment of the ANTARES Instrumentation Line (IL13), with the PPMDOM integrated on floor 1 at about 100 m above the sea floor, occurred just in time for me to take part in the initial operation of the PPMDOM prior to leaving university. Performing and analysing measurements with the freshly deployed module allowed me to compare my simulation-based predictions with actual data from the deep sea.
Data of seven months of almost daily test runs has been analysed for hit rates and baseline rates of each PMT, bioluminescence events, ^{40}K double coincidences, and bright events with four or more triggered PMTs.
Using ^{40}K coincidences, I investigated several approaches to calibrate the internal timing of the OM. I attempted to count the number of photoelectrons per PMT hit using the ToT information. Based on the results of my acceptance simulations I developed a pointing algorithm, which creates a probability map for the origin of detected light flashes, I tested this algorithm using the ANTARES calibration LED beacons.
A thorough analysis of a long-term data stack, including a data-to-Monte-Carlo-comparison, concluded my work on this project.

7.1 Data Taking and Processing

7.1.1 Data Acquisition

The PPMDOM data taking was done by manually starting a measurement (or "run"), which started a recording of all PMT hits without triggering or filtering. When the data file reached the desired size, the run had to be stopped by hand. Depending on the background noise, the data rate could be on the order of one gigabyte per minute. Therefore, at that time only short snapshots of data could be taken. Usually, two runs of five to ten minutes were taken daily, but this duration increased due to evolving stability of the data taking. Furthermore, improving sea conditions with less noise due to bioluminescence, which at the ANTARES site is at its highest in spring, yielded more run time per disk space.
The raw data could then be analysed for single photon rates, coincidences, time correlations,

bright events, influence of PMT parameters and effects of calibration changes.

As there was neither time synchronisation with ANTARES nor even a proper reference clock within the DAQ system of the PPMDOM itself, it was not possible to correlate events recorded by ANTARES with bright signals in the PPMDOM. The exception were ANTARES calibration beacon runs, which could be observed with the PPMDOM when it took data ran during those. Several such runs were coordinated with the ANTARES shift crew.

The clock starts at zero at the beginning of each run. Each recorded hit contains the time since the start of the run and the charge information in the shape of the time over threshold (ToT). The time resolution of the data acquisition, at least from the side of the read-out software, is one nanosecond, as both the event time and the ToT are stored as integers. The typical ToT for a single photoelectron event is 31 ns. The data is divided into timeslices of about 0.134 s, or exactly 2^{27} ns.

7.1.2 Data Processing

The raw run data was transferred to the Centre de Calcul de Lyon (CCLyon) [16]. A filter tool to convert it to a more easily usable ROOT tree file[1] already existed.
The ROOT file could then be read and processed using common tools. Even though a comprehensive software package to analyse the PPMDOM data was being worked on by other members of the KM3NET collaboration at that time, due to time constraints it was necessary for me to write the data processing and analysis software for the specialised tasks for this thesis myself. Common analysis results produced by several members of KM3NET, like the time calibration, have been compared. The different implementations and approaches produced compatible results (even if it sometimes took some collaborative debugging efforts).

The computing power of the CCLyon allowed me to analyse a large part of the gathered data in an automated way. Certain more complex tasks, like the direction reconstruction, have been confined to a hand-picked selection of runs that were performed in good sea conditions. This was owed to the experimental nature of the methods and the limited time available, which prevented my from implementing advanced filtering algorithms that would have been able to suppress known background signal patterns occurring in high-bioluminescence sea states.

[1] ROOT [33] is a data analysis framework developed at CERN which sees widespread use in the particle physics community, and allows to process and visualise large amounts of data with relative ease.

7.2 Data Analysis

7.2.1 Single and Coincidence Rates, Bioluminescence, Baseline

Single and Coincidence Rate

The single rate of each PMT is simply the number of hits per second registered by the PMT base that exceed the defined threshold for a single photoelectron event. This information can be very easily extracted due to the way the data is stored: Inside the ROOT tree file, the number of hits registered by each PMT in a given timeslice is directly accessible. From this, the average hit rate during each timeslice can be calculated as

$$\frac{\text{number of hits in timeslice}}{\text{constant timeslice length}}.$$

All plots of PMT rate over time shown here therefore have a granularity of this timeslice length of 0.134 s (2^{27} ns).
Due to the difficulties in extracting a charge information from the ToT, all registered hits count as one single photon for the purpose of PMT and OM rates.

The total rate (of the OM) is the sum of all PMT single rates. Coincidence rates mentioned in the text usually refer to the whole OM, unless the coincidence rate of a certain PMT pair is considered. The double (or twofold) coincidence rate is the number of occurrences per second where two PMTs of the OM register a hit within the coincidence time window.

The PMT rate is generated by dark noise of the PMT (which should be less than 2 kHz in PMTs tested to comply with design specifications), ^{40}K background (about 3 kHz per PMT according to the results of my simulation), different types of bioluminescence contributions, and actual signal events caused by Cherenkov light from passing muons or neutrino interaction vertices. An example plot of the rate over time is shown in figure 7.1 and shows the typical deep-sea background during a reasonably "quiet" day.

Bioluminescence

Two types of bioluminescence are observed at the ANTARES site: A background of several kHz consisting of single photon events, which changes slowly during the course of the year, and short bursts of very high rates, usually in several PMTs, lasting several seconds.

The constant background is attributed to luminescent bacteria, whose concentration in the deep sea varies seasonally and usually peaks during springtime, when the Rhône carries high waters. This "bacterial background" is usually very evenly distributed in the water, even though sometimes bacteria-laden "clouds" moving through the ANTARES detector can be observed, which increase PMT rates in some parts of the ANTARES detector but not in others.

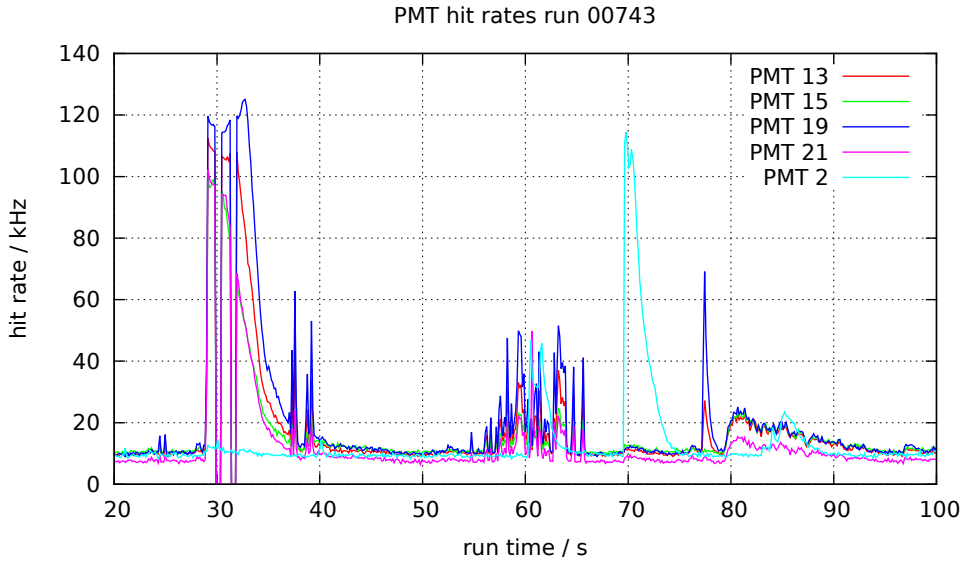

Figure 7.1: This graph shows the single photon rate over time for run number 00743 and PMTs 13, 15, 19, 21 and 2 (according to the DAQ numbering scheme, see table A.9 for details). The PMTs of the DOM have been calibrated to deliver roughly the same baseline rate. The bursts of bioluminescent activity are clearly visibe. As the first four of the selected PMTs are neighbours, their bursts of high rates correlate. PMT 2 is on the opposite side of the OM and "bursts" independently of the other PMTs shown here. The short periods of zero rate within bursts are artifacts caused by the excessively high rates overloading the DAQ.

The bursts of bioluminescence are assumed to occur when planktic lifeforms like pyrosoma, or bigger sea animals, are driven against the surface of an optical module or the miscellaneous structures of the detector by the sea current, which causes them to flare up. These outbursts can cause PMT rates up to 100 times the normal background rate in an ANTARES OM and last up to a few tens of seconds, during which the intensity slowly fades. The plankton theory is supported by the fact that the frequency and intensity with which bursts occur highly depend on the speed of the sea current. Further evidence is the tight localisation of the burst sources on a small area of the OM surface, which can be observed with the multi-PMT DOM. Finally, luminescent macro-organisms have been photographed with cameras integrated into the ANTARES instrumentation line. These may also contribute to longer bursts.

Figure 7.1 illustrates that these bursts occur localised on a small area of the OM, affecting anly a handful of PMTs. The hit rate of five PMTs, four of which are neighbours, is shown for a duration of 80 seconds. The background rate of all five PMTs is very similar, as a result of careful selection and calibration. The various outbursts usually happen either at the four neighbours (e.g. from 30 to 40 seconds), or at the fifth PMT (number 2, e.g. at 70 seconds), which is at the opposite side of the OM. Still, some burst events do not fit the scheme and seem to encompass the whole OM (from 55 to 65 seconds).

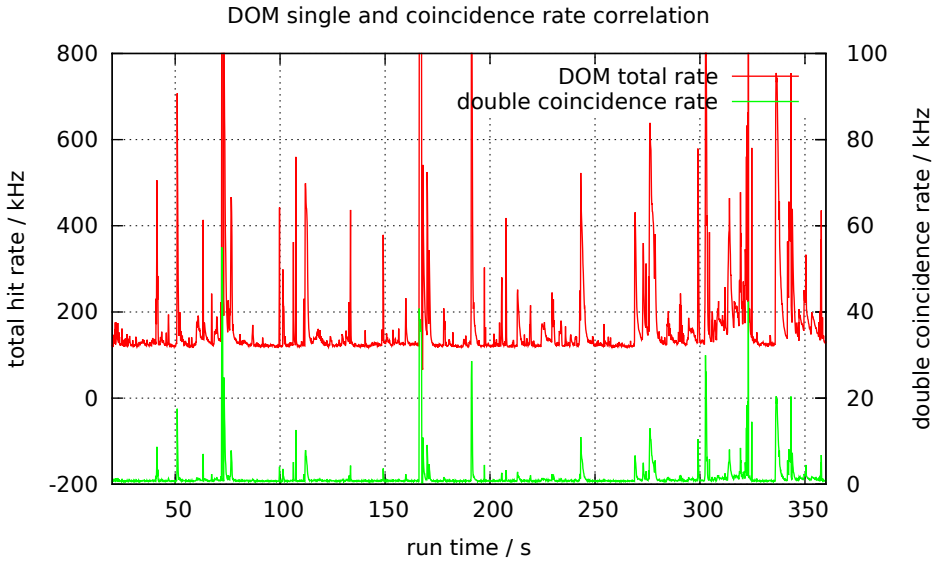

Figure 7.2: Correlation of double coincidences with bursts of bioluminescent activity during run 00951. The upper, red, curve shows the total hit rate of the OM (the sum of the rates of the 31 PMTs), the green curve below the rate of double coincidences. The increase in double coincidences during bioluminescence bursts is much larger than what would be expected if the photons were randomly distributed over the PMT surface.

Looking at figure 7.2, one can see the total event rate of the PPMDOM (the sum of the hit rates of all PMTs) and the rate of twofold coincidences for the complete duration of run 951. The bursts visible in the single event rate cause a large increase in the double coincidence rate. In the case of random coincidences uniformly distributed over the surface of the OM, the coincidence rate would be proportional to the square of the single rate. The increase of the double rate is obviously much higher, affirming that the bursts are indeed, for the most part, localised events.

Figures 7.3 finally show that quadruple (and higher order) coincidences remain virtually uninfluenced by these bursts. They display the rate, respectively the number of occurrences per timeslice, of twofold, threefold, fourfold and fivefold coincidences. Obviously, there is no correlation between the bursts of twofold coincidences and the number of fourfold coincidences, while double and triple coincidences correlate strongly. This is the reason why I chose a coincidence level of four or higher in the analyses of bright events, which I describe later in this chapter.

Baseline

The baseline rate is the average background event rate of a PMT in the absence of bursts of bioluminescence. It is a statistical value that can be gained from the data of a complete

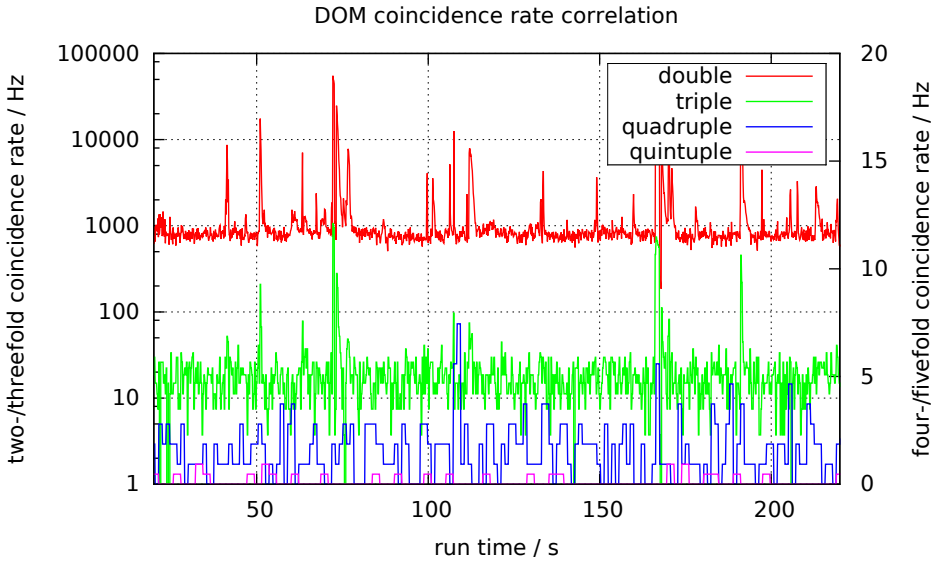

(a) coincidence rates

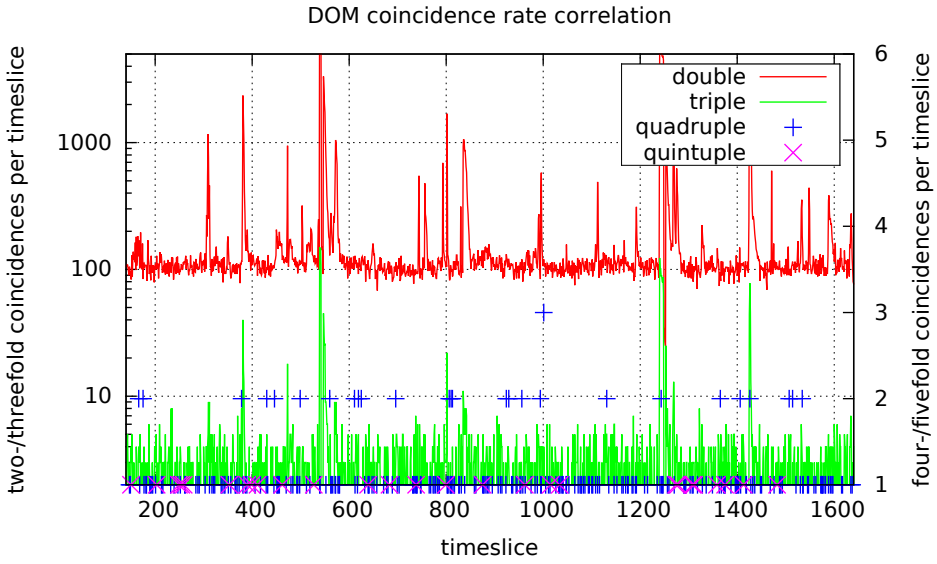

(b) coincidence hits per timeslice

Figure 7.3: Data run 951, correlation of double, triple, quadruple and quintuple coincidences. Figure 7.3(a) shows the average rate in Hz calculated on the basis of one timeslice for double, two timeslices for triple, eight timeslices for quadruple and 16 timeslices for quintuple coincidences (otherwise, the rate of the higher level coincidences would be zero in most timeslices).
Figure 7.3(b) shows the raw number of hits per timeslice for all coincidence levels. Fivefold coincidences never occur more than once per timeslice in this sample, and do not seem correlated with bursts of bioluminescence.

run, or from a sufficiently long time window in case of a longer data run, during which the sea conditions may have changed.

To obtain this baseline, a histogram of the number of PMT hits per timeslice, as can be seen in figure 7.4, is generated from the data file. It will show a roughly Poissonian distribution starting at a minimum value (the lowest number of hits observed in a timeslice), on which a tail of timeslices with higher hit counts is superimposed. The baseline rate is defined as the centre of the peak, in practice obtained by fitting a Gauss function to the distribution. The tail of timeslices with higher event counts originates from bioluminescence bursts.

In the completed neutrino telescope, finding coincidences, both within one OM and between several neighbouring OMs, is the main method of distinguishing signal from background events. Momentary high rates caused by bio bursts are therefore highly undesirable, as they lead to a high number of unwanted random coincidences. The baseline rate and the characteristic width of the associated distribution can be used to intelligently filter out single PMTs with a momentary high rate.

In my analysis, in analogy to ANTARES methodology, all timeslices with a hit count larger than the baseline plus three times the σ of the Gauss fit were tagged as noisy for that PMT. In a multi-PMT OM, several approaches to filtering noisy PMTs offer themselves:
It is possible to eliminate from the analysis either only those PMTs that exceeded were tagged as noisy in this timeslice.
A stricter approach would be to disregard noisy PMTs and their respective neighbours: Even if the neighbours have not been more than 3 σ above their baseline, their hit rate in the "suspect" timeline may still be higher than normal (in the absence of a burst) and lead to an increase in false coincidences.
The most radical approach would be to delete all events from that timeslice. This may be warranted during periods of extremely high bioluminescence activity, which are often observed at the ANTARES site during spring.

Which filtering method presents the best choice depends on the sea condition durings data taking and the purpose of the analysis. The more restrictive approaches possibly discard valid and valuable data, but may improve the purity of the desired signal. For high baseline rates and burst fractions (the fraction of timeslices under the influence of a bioluminescence burst), zealous filtering is necessary to avoid creating too many (false) coincidences, which may overload the DAQ.

7.2.2 Time Calibration

As has been established with the results of my simulations, close ^{40}K decays usually trigger two neighbouring PMTs simultaneously. This can be used to establish the systematic time difference between two PMTs of the DOM introduced by different signal delays in the PMT base and different wiring lengths.

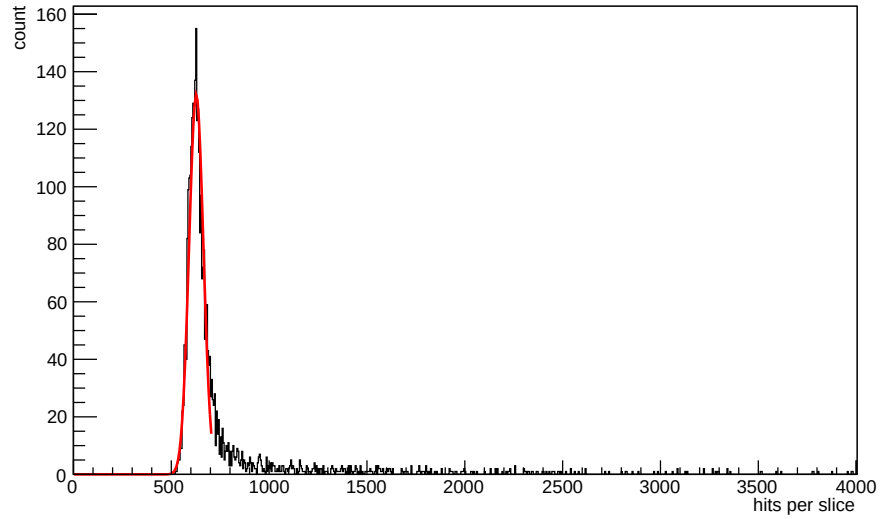

(a) Baseline fit for run 951

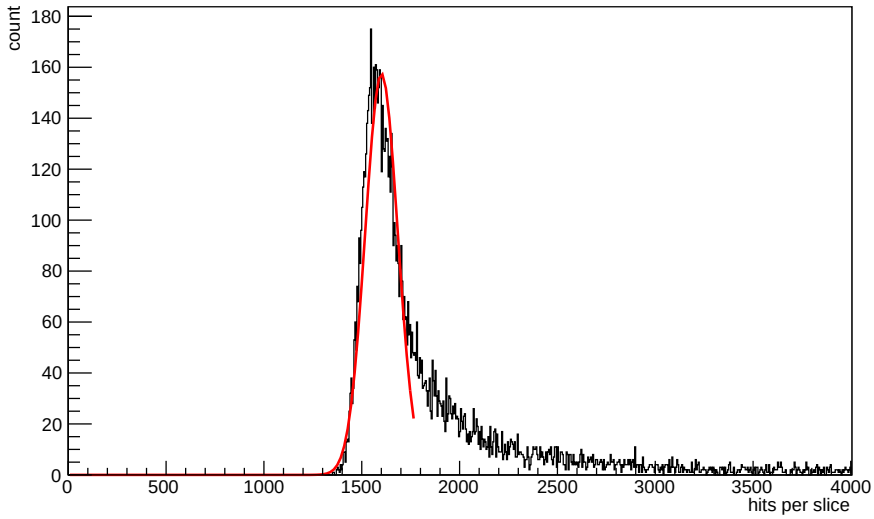

(b) Baseline fit for run 743

Figure 7.4: Determination of the baseline rates for the downward facing PMT. The histograms depict the number of timeslices that contained a certain number of hits. The binning is 5 hits. A timeslice equals to 2^{27} ns or about 0.134 seconds.
Histogram 7.4(a) on top was generated from run 951, a rather "quiet" run, where the baseline for this PMT was 4.7 kHz. The second histogram 7.4(b) was created from the much noisier run 743: The large number of bioluminescent outbursts is clearly visible as a pronounced tail to the right of the baseline peak, while the baseline for this run was 11.9 kHz.

To obtain this time difference, I applied a sliding coincidence window of 50 ns to the timeline of PMT hits, looking for twofold coincidences. A histogram was prepared for each possible PMT pairing (2 out of 31 equalling 465 pairings). Similarly to figure 6.9 these histograms contain the time difference between the time the first PMT of a pair was triggered and the time when the second PMT was triggered. In the example of figure 7.5(b), the time difference histogram for PMTs 22 and 13, whenever PMT 22 was hit first, the time difference was positive, and when PMT 13 was hit first, the time difference was negative. If there was no systematic time shift between the PMTs, the distribution would be Poissonian, centred at 0 ns.

A histogram of a PMT pair where the PMTs are on opposite sides of the OM will show constant background of purely random coincidences. For random coincidences, every time difference is equally like, so every bin of the histogram will receive roughly the same amount of hits, within normal variation.
A histogram of two neighbouring PMTs, and, to a lesser, but still recognizable extent, of two next-to-neighbouring PMTs, shows a Gauss-shaped peak over the flat background of random coincidences. After fitting a Gaussian function, the position of the centre directly yields the time offset between the PMTs; it would be zero if there was no systematic time delay between them. The width of the distribution mainly depends on the TTS values of both PMTs. Examples for both cases are shown in figure 7.5.

For many analyses it is imperative to keep the coincidence window as short as possible. This can only be achieved if the time offset between the PMTs is compensated. Therefore, the systematic time difference between each PMT and a common reference PMT has to be established.
As it is only possible to obtain the time difference between two PMTs at a time, one has to pick one PMT as a starting point and calculate the time difference of every other PMT to that via a kind of daisy chain. Due to the symmetry of the OM, the PMT pointing downwards lends itself to be the reference point. One can directly calculate the time difference of each the six PMTs in the first crown to this reference point. In the next layer up, every PMT has two equidistant neighbours below, whose time offsets to the reference PMT are already known. From those and from the time differences between the upper PMT and its lower neighbours, one can calculate the time offset of the upper PMT with respect to the reference PMT. One can do this for every crown to get the time offset between each PMT and the reference. A clarifying example is shown in figure 7.6.

The downside of this method is that the errors of the Gauss fits on the ^{40}K time difference peaks propagate, and that the total error grows from layer to layer. This is mitigated somewhat by the fact that there are always two time difference fits that contribute to each calculated offset. This can also be used to filter questionable fits: A bad Gauss fit can usually be detected via its large reduced χ^2. If that value is above a certain threshold, the calibration routine only uses the time offset value of the better fit. The threshold was empirically chosen and fixed at a value of 2.5 for the presented analyses.

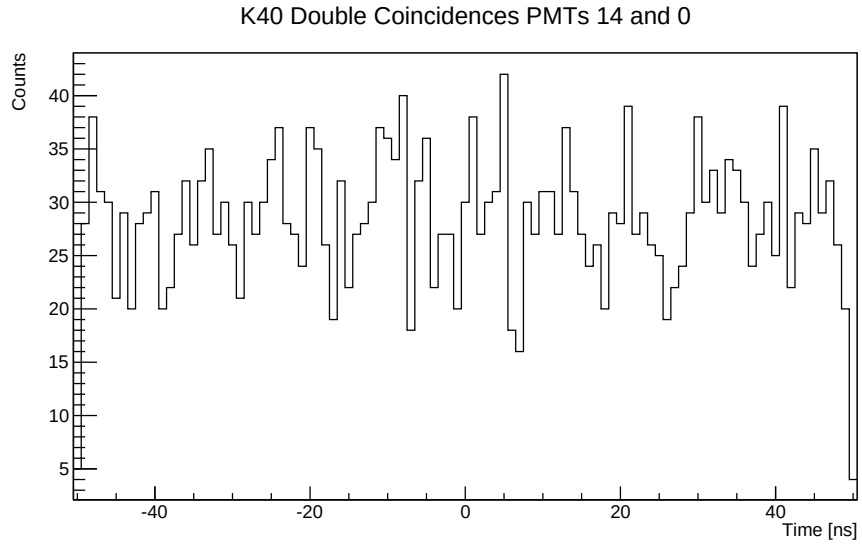

(a) time difference plot for PMTs on opposite sides

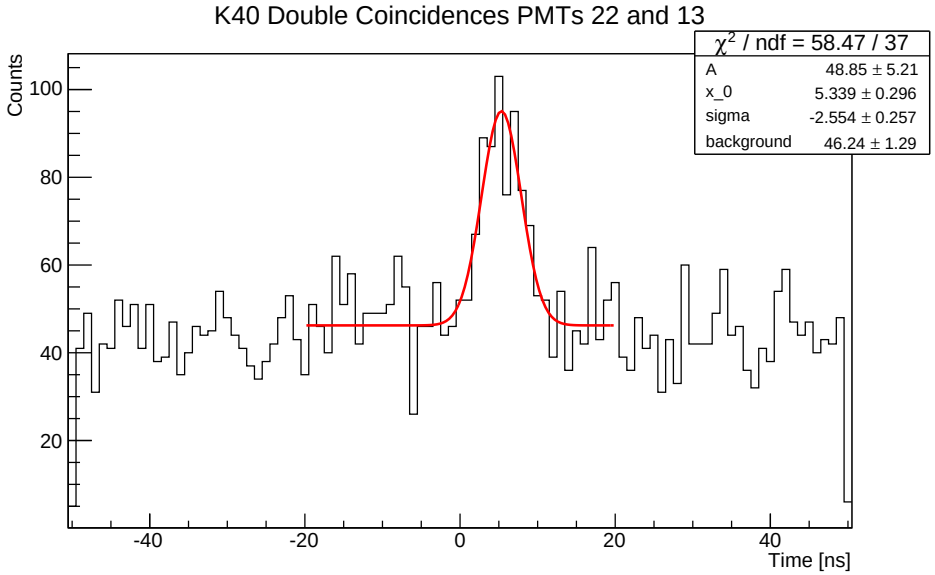

(b) time difference plot for neighbouring PMTs

Figure 7.5: Example time difference histograms of coincidence events for two PMT pairs. PMTs 14 and 0 are situated on opposite sides of the OM: The arrival times of the photons causing the coincidence events are randomly distributed, no correlation is apparent nor expected. PMTs 22 and 13 are direct neighbours: a clear Gauss-shaped peak is visible above the background of random coincidences, as would be expected from ^{40}K decays. The Gauss function fitted to the data has an offset of 5.339 ns: This is the time delay of signals in PMT 13 when compared to PMT 22. For a typical run duration of less than ten minutes, a time difference fit of sufficient quality is only possible for direct neighbours. Section 7.4 shows the possibilities offered by a large data sample.

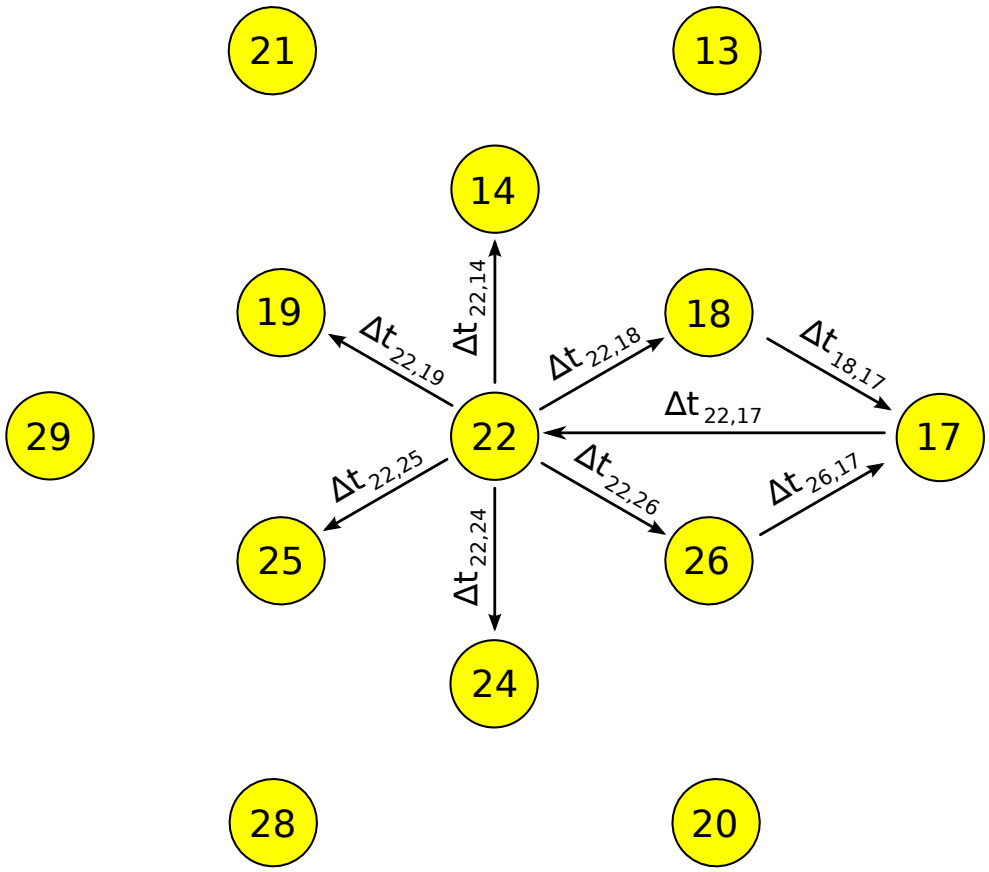

Figure 7.6: Illustration of the method for time calibration. The bottom PMT and the two lowermost PMT crowns are shown. Each PMT is numbered as in the PPMDOM DAQ. The time difference of the PMTs in the first crown is taken directly with the bottom PMT as the reference point. In the higher crowns, the time difference of each PMT to the reference PMT is calculated from the time differences to its two lower neighbours and their time difference to the reference PMT.

While this time calibration scheme works already reasonably well on a single data run of about ten minutes or longer, the errors can be vastly reduced by a longer measuring time. Due to the prototype nature of the data acquisition, most runs of 2013 were only from a few to a few tens of minutes long. Therefore, the time difference histograms of a large number of runs were stacked, and a time calibration was derived therefrom. The result is shown in table A.10 in the appendix. This time calibration was used in further analyses.

For this stacked time analysis, only runs with low bioluminescence rates were used, therefore the sum of all PMT baseline rates had to be below 300 kHz for a run to be included in the stack. Furthermore, as the timing characteristics of a PMT depend on the applied high voltage and the selected signal threshold, only the recent runs sharing the same high voltage tuning could be used. The stack finally included runs from run number 714 up to 943.

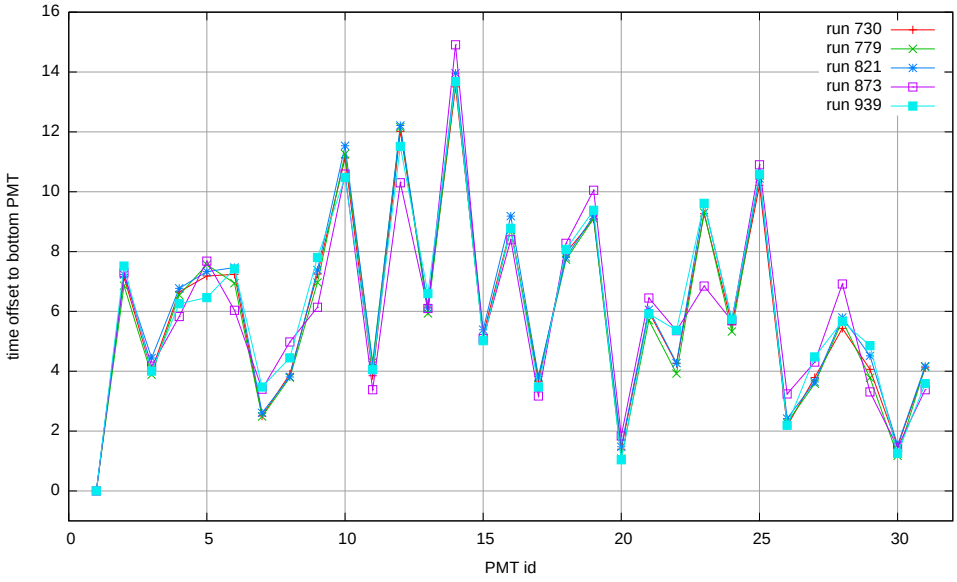

Figure 7.7: Stability of the time calibration demonstrated using five randomly selected runs out of three months of data taking. The systematic time offset (in nanoseconds) between the reference PMT and each other PMT is depicted. Differences between individual runs lie within expected error ranges of typically 2 ns (error bars not shown for better legibility) and do not show any tendency to drift toward any direction. Run 873 was taken during a period of high bioluminescence and therefore has worse time fits and larger errors, but was included for comparison.

In order to establish that the time differences between PMTs do not drift over time, the time calibration results from a number of randomly selected runs out of the stack were compared. An example overlay of five runs from a space of three months is shown in figure 7.7. The differences lie within the expected error ranges. Run 873 is the exception. It was a shorter run in bad sea conditions and not part of the stack, and is included only for comparison and to demonstrate the stability of the time calibration method.

7.2.3 Attempt at Photon Counting

The time over threshold, or ToT, can in theory be used to estimate the number of initial photoelectrons created at the photocathode.

The amount of electrical charge deposited in the anode per photoelectron follows a Poissonian distribution. This distribution can be measured with calibration measurements at very low light levels. This is done by placing the PMT to be investigated into a dark box and illuminating it with a light pulser – an LED or laser – properly attenuated so that only a few photons reach the PMT per light pulse. The trigger signal for the light pulser also triggers the charge measurement, the duration of which has to match the expected maximum signal length as to

minimise noise.

If it were possible to always send exactly one photon to the PMT per light pulse, it would be possible to directly measure the charge distribution caused by single photoelectrons. A photon may or may not create a photoelectron, but in any case one would either measure some charge value, or no charge at all, for each light pulse (assuming that there are no other noise sources). Then, one could do the same for two, three, etc. photons – but then, the quantum efficiency of the photocathode would already falsify the result: if there are always two photons simultaneously arriving at the photocathode, then both will individually have a probability of the QE value of creating a photoelectron, and the result will be that there is either no charge to register, or a single pe charge, or a charge that is the result of two independent photoelectrons. In other words, the result would be a superposition of the single pe charge distribution and the double pe charge distribution, with each contributing according to the probability of that configuration.

In practice, it is not possible to emit a constant, fixed number of photons, so that the measured charge distribution will always be a superposition of the charge distributions for different number of photoelectrons, mixed with the probabilities mentioned above and further randomized by the varying amount of photons that reach the photocathode during each light pulse. One therefore has to try to fit a superposition of Gauss functions, each representing the charge distribution of a certain pe multiplicity, to the total charge distribution extracted from the measurement. An example of what this might look like is given in figure 7.8, created with a simulation and analysis script written by Dr. Oleg Kalekin.

If the charge distribution of each photoelectron multiplicity is known, it would allow to state the probability that a measured charge quantity has been caused by a single photoelectron, or by two photoelectrons, or by three, etc.
The same approach was tried on the ToT distribution of PPMDOM data runs. One can safely assume that the PMT signals consist of a mixture of single, double, triple and higher photoelectron events. Therefore, a histogram of the relative frequency of each ToT value was created, and it was attempted to apply a multi-Gauss fit on this distribution. However, the first attempts at extracting meaningful results were unsuccessful, and due to time constraints this analysis was abandoned in favor of more promising analyses.
Figure 7.9 shows an example time over threshold histogram for PMT 30.

This approach was also used by another member of the KM3NET collaboration at that time. The plot that was posted to the internal KM3NET wiki in 2013[2] showed questionable results and gave evidence to the same difficulties I encountered. The consent among the people involved in the PPMDOM operation and data analysis at that time was that a proper charge separation was not feasible with the hardware integrated in the prototype optical module.

[2]At the time of this writing, that plot was no longer available on the wiki and could therefore not be included in this thesis. Neither do I remember the colleague's name.

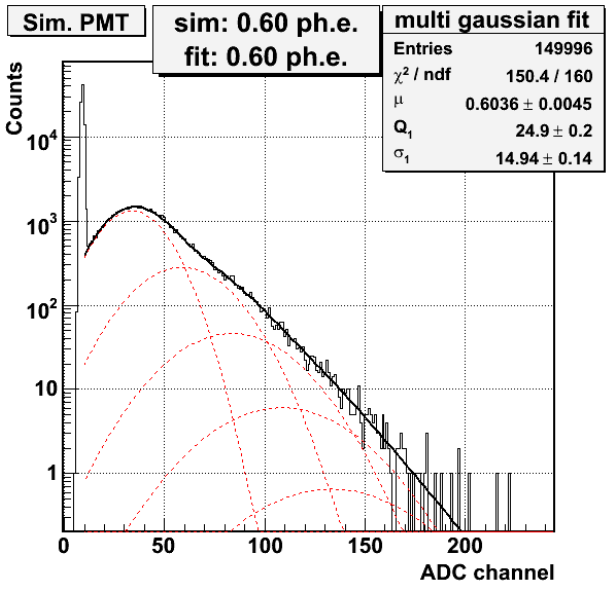

Figure 7.8: Principle of analysing charge calibration measurements. A PMT in a dark box is illuminated by a very low intensity LED or laser pulser, so that only single – or at least few – photons reach the photocathode per pulse. The electrical charge deposited in the anode is registered via an ADC. The charge distribution, when visualised in a histogram, will then look similar to the one above, with a pedestal of dark noise at small charge values (here: the sharp peak around ADC channel 10) and a mountain with a long flank produced by actual photoeletron events. In the image, the thin line is the (simulated) measured charge, the red dotted curves are the Gauss functions corresponding to the charge distribution of singe/double/triple/etc. photoelectron events, and the solid black line is a superposition of the Gauss functions, which should follow the measured charge distribution if the Gauss fits were successful.

7.3 Pointing

The fact that the photocathode area of the multi-PMT optical module is segmented into 31 individual PMTs allows for an approximate reconstruction of the direction of light sources. If a number of neighbouring PMTs is hit by photons at the same time, it is highly likely that the light comes from a single bright source, like the Cherenkov cone of a muon, a vertex shower, or one of the ANTARES calibration beacons.

Studies of the coincidence rates at different levels show that the correlation between momentary coincidence rate increases and bioluminescence bursts vanishes at the level of fivefold coincidences (see figure 7.2). Based on simulation data, Cherenkov light produced by ^{40}K decays only causes one five-fold coincidence every 10 seconds in the PMDOM, and far fewer six-fold events. Assuming a purely random single photon background of 10 kHz per PMT results in a rate of 3.2×10^{-15} Hz for level 6 coincidences with a coincidence time window of 10 ns. This already shows that the measured rate of sixfold and higher coincidences of 38 mHz (taken from

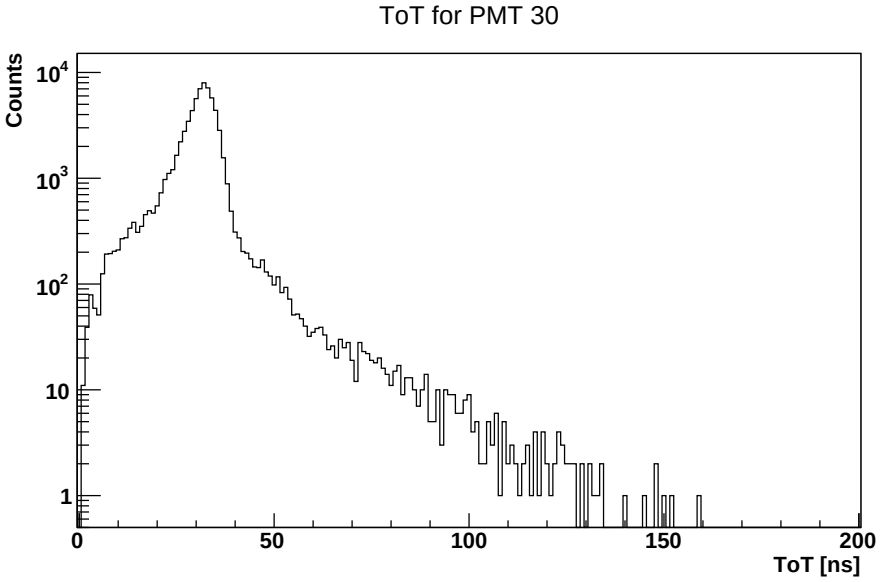

Figure 7.9: Histogram of time-over-treshold values for PMT 30 during run 627. One can see the small pedestal of sub-photoelectron noise signals at around 5 ns, and the hill of single photoelectron (spe) signals peaking around 31 ns. It proved difficult to find conclusive solutions for a multi-Gauss fit for ToTs beyond this spe peak.

the representative run 951) cannot be caused by random background. Coincidences of this level are predominantly caused by a real bright source, be it a fish or a neutrino.

The primary signal that a neutrino telescope is designed to detect is Cherenkov light from muons passing through the detector. The detected muons are predominantly of atmospheric origin, meaning they were created in interactions of charged cosmic rays with nuclei of the upper atmosphere. When conducting neutrino astronomy, atmospheric muons are yet another source of background noise, whereas in the context of my work, all muon tracks are a signal that can be well distinguished from the "low-level background noise" caused by ^{40}K, electronics and bioluminescence.

Atmospheric muons can easily reach the depths of several kilometres below sea level where our optical modules lurk. As the distance such a muon has to travel through water increases with decreasing zenith angle (defining a zenith angle of 90° as from straight above and 0° as arriving from the horizon), it is clear that atmospheric muons must arrive mainly from above. Therefore, their Cherenkov photons, emitted at an angle of approximately 42° with respect to the forward direction of the muon, will predominantly hit the PMTs that are on the upper levels of the PPMDOM. It has been established earlier that six-fold coincidences are a good criterion for signal/background separation. Figures 7.10 go into further detail on this matter. They show how many fivefold coincidences (fig. 7.10(a)), repespectively sixfold and higher coincidences (fig. 7.10(b)), each PMT was involved in during data run 945. The PMTs are numbered as in

the simulation, so that PMTs located in the same crown within the PPMDOM are depicted in blocks of six. A similar figure created by Tino Michael can be found in [32].

A comparison of the two histograms shows that the number of higher level coincidences each PMT contributes to clearly decreases the farther down in the DOM that PMT is located, as is expected if atmospheric muons are the main source. Crowns 4 and 5, located above the PPMDOM's equator, clearly see more high-level (muon-induced) coincidences than the crowns below the DOM's equator.
Conversely, lower level coincidences seem to have their origins below the OM, according to figure 7.10(a). The reason for this is not completely understood. A slight suppression of the upper crowns is to be expected, due to the fact that the PMTs in those crowns have no neighbours above them, which will lead to fewer registered coincidences. It is unclear whether the blind area of the PPMDOM completely accounts for this effect. Possibly, part of the bioluminescence background is created near the sea floor, thus contributing to a higher coincidence rate in the lower crowns.

Histogram 7.10(b) additionally shows that one or two PMTs of each crown register significantly lower photon counts. This is caused by the shadow of the storey's electronics container shown in photograph 4.3, as can be verified via the azimuthal position of the affected PMTs. It affects the upper crowns the most, as the magenta and cyan blocks testify.

A coincidence window of 10 ns was chosen for all pointing analyses. Assuming a monochromatic light front emitted in an infinitesimally short pulse, all photons thereof should arrive within a time window of about 1 nanoseconds: At a speed of light of $22\frac{\text{cm}}{\text{ns}}$ in water, photons impinging at the point of the OM closest to the front and photons just touching the side of the OM arrive with a time difference of roughly 1 ns. This time difference is too small to be resolved.
Taking into account the effects of dispersion adds a spread of about 5 ns for a Cherenkov light front traversing a distance of 100 m.
Further time differences between registered hits are introduced by the transit time spread (TTS) of the PMTs, systematic time offsets between PMTs (unless properly compensated with a time calibration), and the "depth" of the light front or the length of a pulse. The TTS of all PPMDOM PMTs have been measured to conform to the specification of less than 5 ns (see table 4.1) prior to integration. The systematic time difference introduced by the electronics has been compensated using the calibration method described above. Therefore, the shortest possible coincidence window that does not discard photons from passing muons is about 10 ns.

7.3.1 Algorithm 1: Vector Addition

If a homogeneous light front arrives at the OM, the chance for each PMT to be hit by photons is proportional to its effective area with respect to the direction of the incoming light. As a first order approximation, the effective area should be proportional to the cosine of the angle between the PMT normal and the direction the photons arrive from. It then follows that the

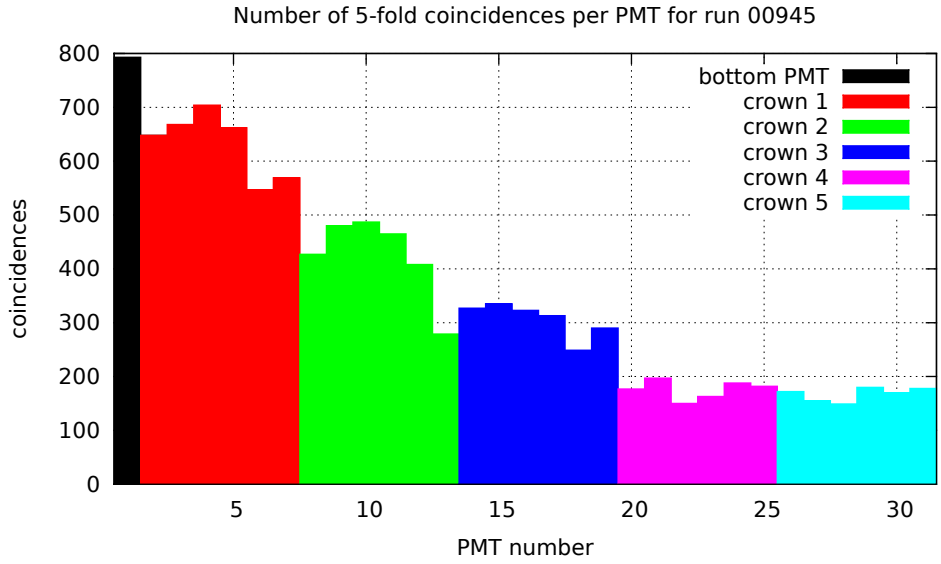

(a) 5-fold coincidences

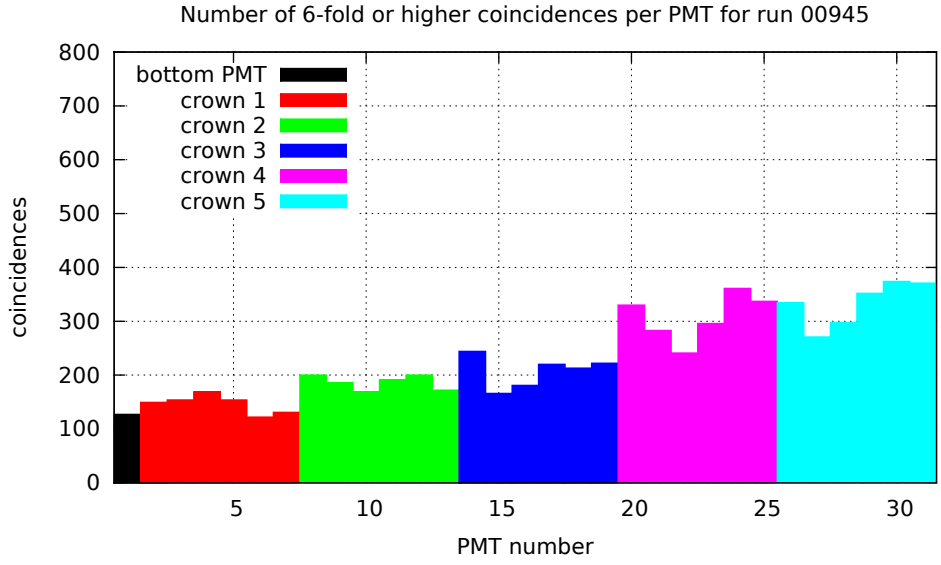

(b) 6-fold coincidences

Figure 7.10: Crown by crown comparison of the number of coincidences per PMT. The upper histogram shows the number of fivefold coincidences each PMT was part of, the lower histogram counts the number of sixfold coincidences. Data was extracted from run 945.
Sixfold coincidences, which have been shown to be independent of the background rate and thus must be caused by (atmospheric) muons, are registered significantly more often in the upper layers of the optical module. Within the upper three crowns, the shadow effect of the electronics container is visible.
Fivefold coincidences appear to originate from below the optical module. This will at least in part be caused by the blind area on top of the PPMDOM. Whether there is another reason, for example increased bioluminescence from the seafloor, is unknown.

PMTs facing the light front more directly will be more likely to register photons than PMTs oriented at an angle. The first guess at the light direction is therefore taken by looking for a cluster of neighbouring PMTs with at least one photon hit each, and averaging over the normal vectors of these PMTs. This approximation can be improved by weighting the PMTs according to the number of registered photons; however, the charge separation achievable with the current hardware and the first version of the time over threshold scheme is too poor to count photons within one PMT.

The drawback of this method is that the result is a discrete vector out of a limited set of possible directions that can be constructed from a base of 31 vectors. Even if it was possible to distinguish single photon hits from two/three/four/etc. photoelectron events and weight the PMTs accordingly, there is still a limited number of solutions. Delivering the result in the shape of a discrete vector implies a precision that does not exist, as this method does not take into account the wide field of view of each PMT. Another problem are random hits in PMTs that face away from the event. It would be necessary to identify which PMTs could realistically have contributed to an event by looking for hit clusters, checking angular distances, and excluding PMTs that do not fit well to the rest of the hits.

Figure 7.11 shows exemplary skymaps for run 945 at different minimum coincidence levels (3 and 5), both with and without ToT-based weighting. In the absence of a proper ToT-to-photoelectrons conversion, weighting was applied by multiplying each PMTs vector with the ToT value. Therefore, PMTs with a large ToT (having possibly registered two or more photons) have a larger influence on the estimated direction of the light source.

7.3.2 Algorithm 2: Probability Map

A better approach to estimate the direction of a light source is to create a probability map in spherical coordinates, based on the acceptance functions of all PMTs that registered a hit within the coincidence time window.

Due to the convex shape of the tube, refraction and reflection between the different layers of the optical module, and the light expansion cones, the effective area of the PMTs follows a complex function. It has been derived using data from a dedicated OM acceptance simulation, which used the specification of the PMTs and expansion rings that were built into the PPMDOM (compare chapter 6.1).
For the pointing algorithm, each PMT's effective area has been converted into a probability map. The resulting histograms contain the probability that a photon coming from a certain direction, given in spherical coordinates within the frame of reference of the DOM, will be registered by that PMT. The resolution was one degree each in θ and ϕ. Due to the way the algorithm works with these histograms, the lowest probability value has been fixed at 10^{-6}.
In each coincidence event, the probability maps of all PMTs that registered a photon within the coincidence window are multiplied together. The resulting map is normalised in the final step. It shows, for each possible direction (θ-ϕ-pair), how likely that direction points to the light source.

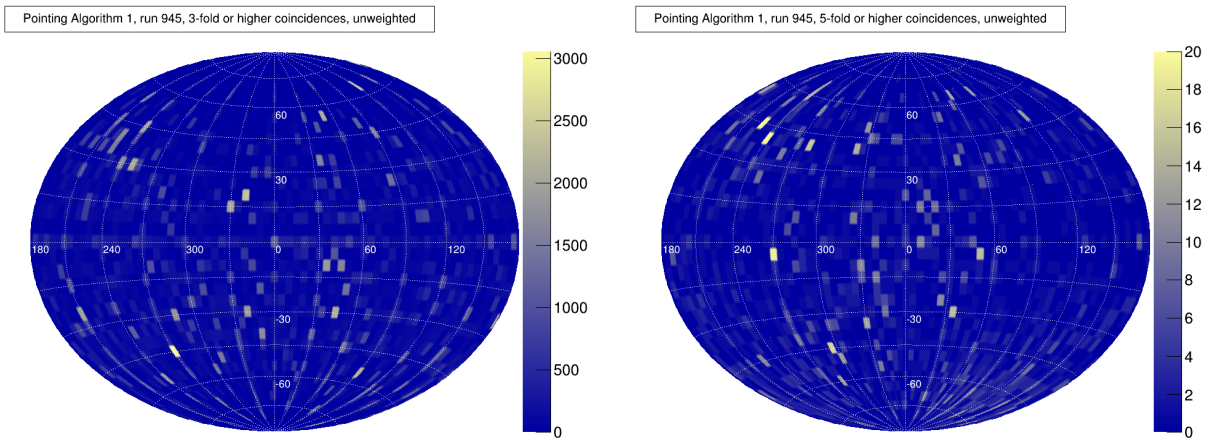

(a) threefold, unweighted

(b) fivefold, unweighted

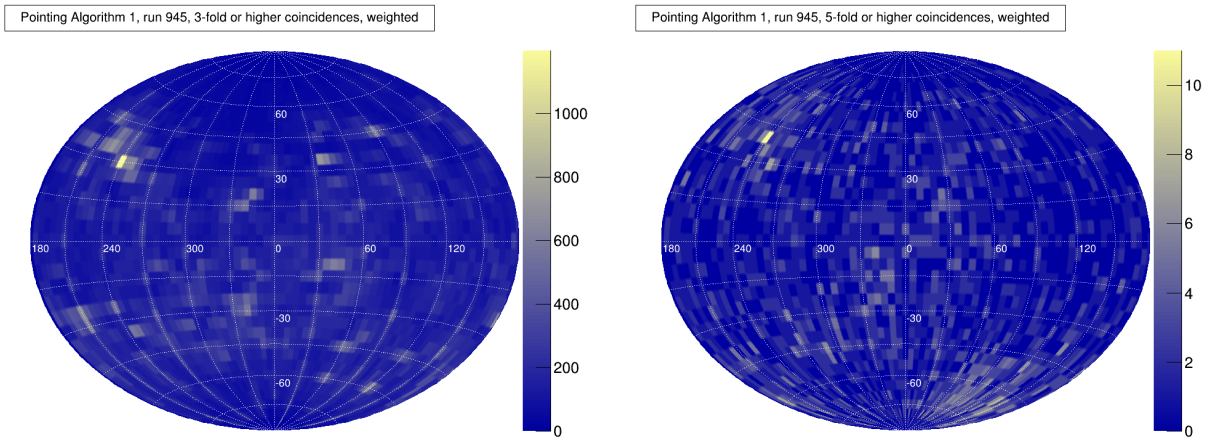

(c) threefold, weighted

(d) fivefold, weighted

Figure 7.11: Pointing examples using vector addition algorithm. In the histograms, the estimated directions of bright events at coincidence levels of three (figures a and c) and five (b and d) from run 945 have been stacked, resulting in the skymaps displayed above. The binning in θ and ϕ is 5°. Skymaps a and b were created using unweighted vector addition for each PMT. The limited number of solutions results in a few bins with a high number of entries, and many empty bins in between. The ToT weighting approach multiplies each PMT's direction vector with its ToT value. This reveals a "hot spot" at $\theta = 30°$ and $\phi = 240°$ which is visible at coincidence levels of three and five. The source is unknown. No ANTARES calibration is known to have been performed during run 945. If the source is a PMT with a high noise rate or abnormally high ToT values, it should be possible to filter it out using a refined algorithm for cluster finding. Compare also the results of the inherently more noise-resistant algorithm 2 in figure 7.13

This pointing algorithm is inherently quite robust against noise. Consider an event with four PMTs involved, of which three are neighbours or next to neighbours and the fourth is nearly at the opposite side of the OM and more than 120° removed from the others. The photon detection probability of this remote PMT for the directions of the three others is almost zero (10^{-6}). At the same time, the photon detection probability of each of the three clustered PMTs is almost zero (10^{-6}) for the direction of the lone PMT. Therefore, the contribution of the remote PMT is suppressed three times in the direction of the clustered PMTs, while the lone PMT suppresses the contribution of the three others only once. The resulting probability map will therefore still have its maximum value in the area of the clustered PMTs.

As explained above, it would be ideal to weight the contribution of each PMT with the number of photons registered by it. As that information is not availably, the probability map of each contributing PMT is weighted by its ToT value as in algorithm 1.

The pointing algorithms have been developed and tested using data taken during ANTARES calibration runs. During these, a number of light emitters, the laser or LED beacons, flash at a given frequency. The light from the beacons can be clearly seen already in the PMT rates. The resulting histogram from applying pointing algorithm 2 to a laser beacon run, in this example run 1033, is shown in figure 7.12.

The position of the beacons relative to the DOM does not vary noticeably for the duration of a beacon run, so the pointing algorithm should yield the same direction for all recorded bright events. Using the compass data from the DOM, it would be possible to point back to the beacon in absolute coordinates[3]. Lacking that, it was only possible to estimate, from the estimated elevation angle to the light source of about 30° below the OM equator and the height of the PPMDOM above the sea floor, roughly 100 metres, that the source should be around 200 metres distant. A to-scale drawing of the position of the redeployed instrumentation line relative to the other ANTARES lines was not available at the time of this analysis, but, judging from the previous position of the IL, that distance would be about right.

[3]The DAQ procedure for the PPMDOM included saving the raw compass data for each run, however, no documentation was available to convert these hex strings to meaningful data.

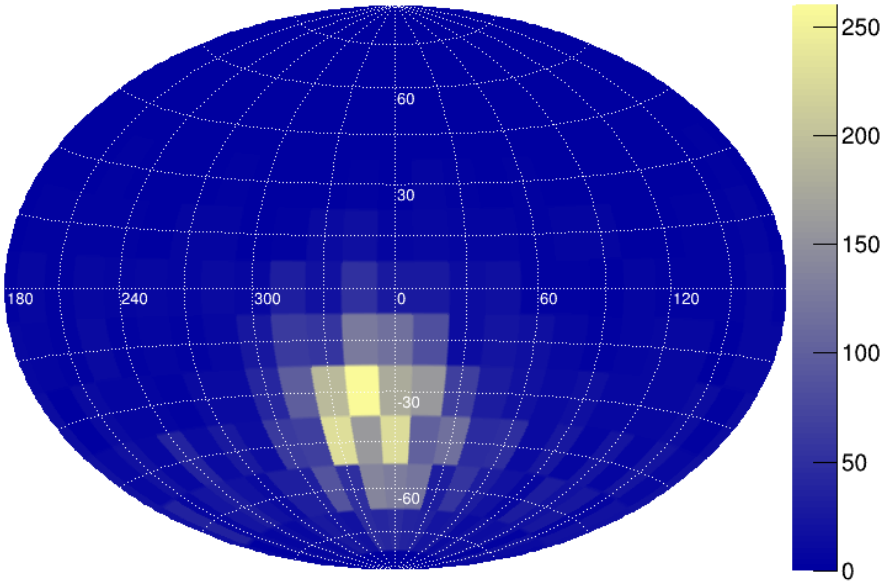

Figure 7.12: Development snapshot of the probability pointing algorithm. PPMDOM data run 1033 was taken while the ANTARES laser beacon was flashing. The depicted skymap was created using fourfold or higher coincidences, thus excluding most background coincidences. The binning was 15° in azimuth and elevation. The graph nicely shows that even with the aforementioned limitations of the hardware, a "bright" light source can be located with an uncertainty of less than 30°. With the completed KM3NET detector this pointing capability can be used to create reconstruction algorithms far superior to what is possible in ANTARES.

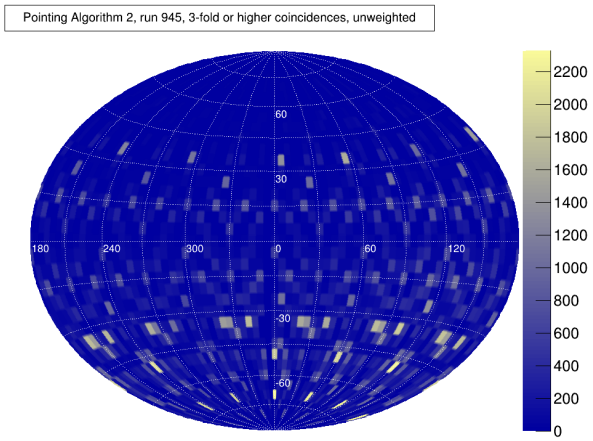

(a) threefold, unweighted

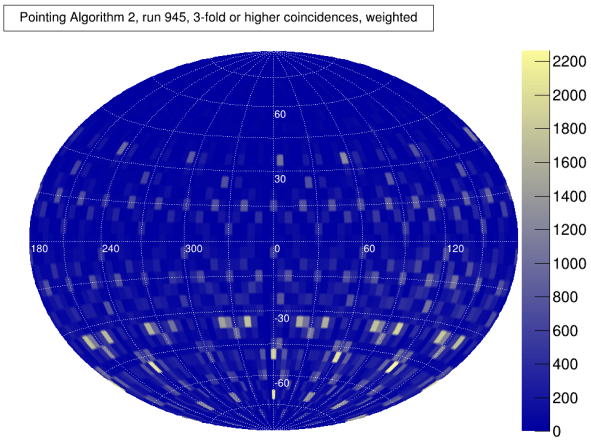

(b) threefold, weighted

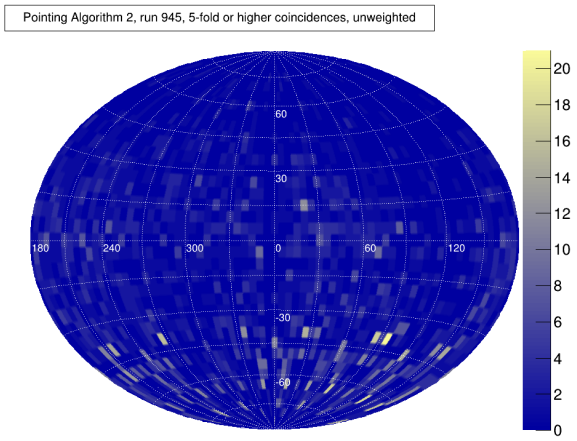

(c) fivefold, unweighted

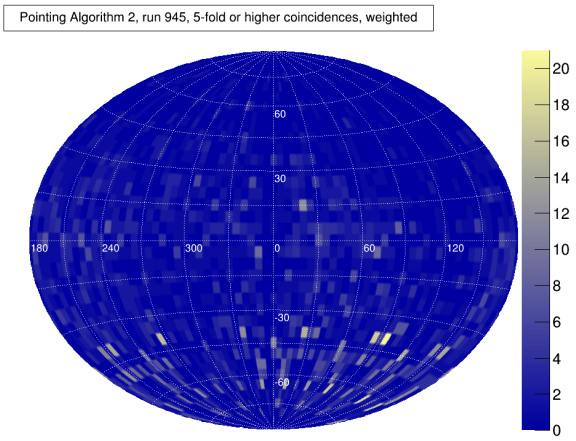

(d) fivefold, weighted

Figure 7.13: Pointing examples using probability map algorithm. In the histograms, the estimated directions of bright events at coincidence levels of three or higher (figures a and b) and five or higher (c and d) from run 945 have been stacked, resulting in the skymaps displayed above. For each analysed event, the position of the maximum value of the resulting probability map was used as the direction of the source and entered into the skymap.
The binning in θ and ϕ is 5°. Skymaps a and c were created using unweighted probability maps for each PMT. ToT weighting was applied for skymaps b and d. The resulting skymaps differ only minimally. The hot spot visible in the skymaps of algorithm 1 (compare figure 7.11) does not appear here. This is further evidence that the source of the hot spot may be a PMT with abnormally high rate and/or ToT, which is automatically suppressed in algorithm 2.

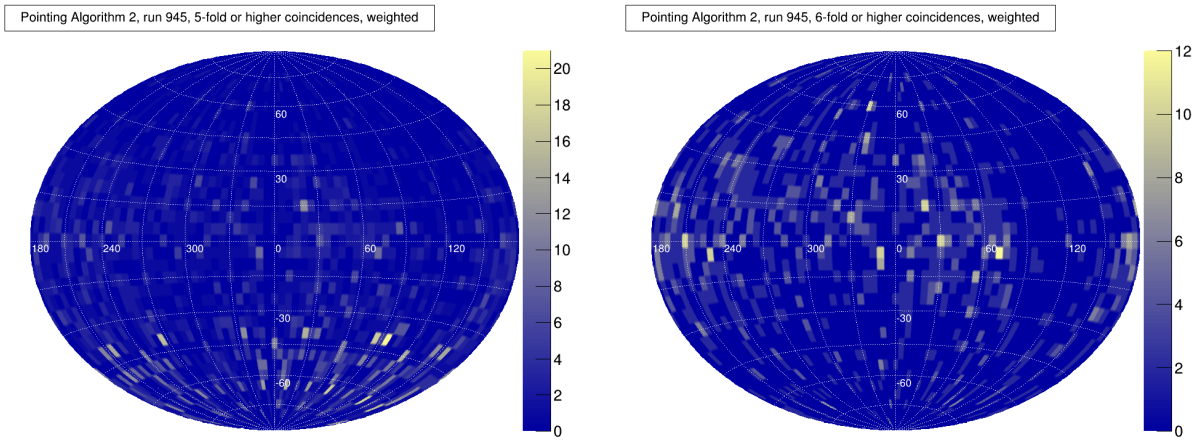

(a) fivefold, weighted (b) sixfold, weighted

Figure 7.14: Skymap of fivefold (or higher) and sixfold (or higher) coincidences in run 945, generated as in figure 7.13 with ToT weighting. Whereas fivefold coincidences, as well as the lower coincidence levels shown before, tend to have sources below the OM, sixfold events tend to originate from above. It is reasonable to assume that these bright events originate from the Cherenkov light of downgoing muons. Tino Michel has also compared the rate of expected muon events (from MC) with the rates of sixfold coincidences and the positions of these coincidences within the PPMDOM. His findings can be found in [32] and strongly hint at downgoing muons.
Note the darker area around an azimuth of 120°clearly visible in (b): It is the shadow cast onto the OM by the LCM container and support structure (compare picture 4.3.

7.4 Stacked Analysis and Data / Monte Carlo Comparison

One of the key predictions of the ^{40}K simulation was the rate and distribution of coincidences caused by nearby decays. These values can of course be extracted easily from the simulation data, which contains no other events.

The rate of single PMT events caused by ^{40}K is inaccessible in real-world data, as they are indistinguishable from the intrinsic PMT noise and from the optical background created by the still not completely understood sources of bioluminescence.
Coincidence rates for nearby ^{40}K decays can however be extracted from the data, by applying the known properties, gained from my simulation, of these events.
In principle, the coincidence rates for every possible PMT pairing have to be summed up, after having eliminated the purely random contribution. Coincidences considered are twofold and higher, where the first two hits decide for which PMT pair the coincidence is counted. As threefold coincidences are about a factor of 10 less common, the error made in counting all coincidences as potassium events – which still holds true for the majority of triple hits – is small. A simple count of threefold coincidences from data compared with the expected triple potassium hits from the simulation shows that there is an excess of typically less than 20 Hz of triple coincidences.
Quadruple or higher order hits were excluded in the analysis, as genuine ^{40}K quadruple coincidences are less likely by another order of magnitude. Events of this brightness are usually bioluminescence bursts or genuine signal events of passing muons.

The procedure used to count the coincidences is as follows. The coincidence histograms used for the time calibration form the base of the analysis. Every possible PMT pair (2 out of 31 equalling 465 combination) is considered. As before, a Gaussian function with an offset equal to the constant random background is fit to the coincidence peak. The number of ^{40}K coincidences is the area of the Gauss bell that rises above the random background. It can easily be calculated from the fit parameters as the integral over the Gauss function, or counted by summing over the histogram entries. In both cases, the random background component has to be subtracted. Both methods yielded compatible results.
Figure 7.15 shows an example fit for the PMT pair 15 and 22 with fit parameters shown in the histogram, which was used to gain the number of local ^{40}K coincidences for this pair. The time calibration has been applied for this analysis, so the peak of the Gauss is near 0 ns.

Trying this on a single run of typically ten to twenty minutes will fail due to low statistics: The larger the angle between two PMTs, the lower the rate of correlated coincidences. It has not been possible to extract coincidence counts for PMT separations of more than about 90° from the data of a single run. Therefore, a stacked analysis of all runs meeting certain quality criteria has been performed. One criterion was that the sum of PMT baseline rates had to be less than 300 kHz, to assure that only runs with low bioluminiscence activity, which creates additional unwanted coincidences, were considered. Furthermore, only runs using the same high voltage and threshold setup can be used, as the timing characteristics of a PMT depend on

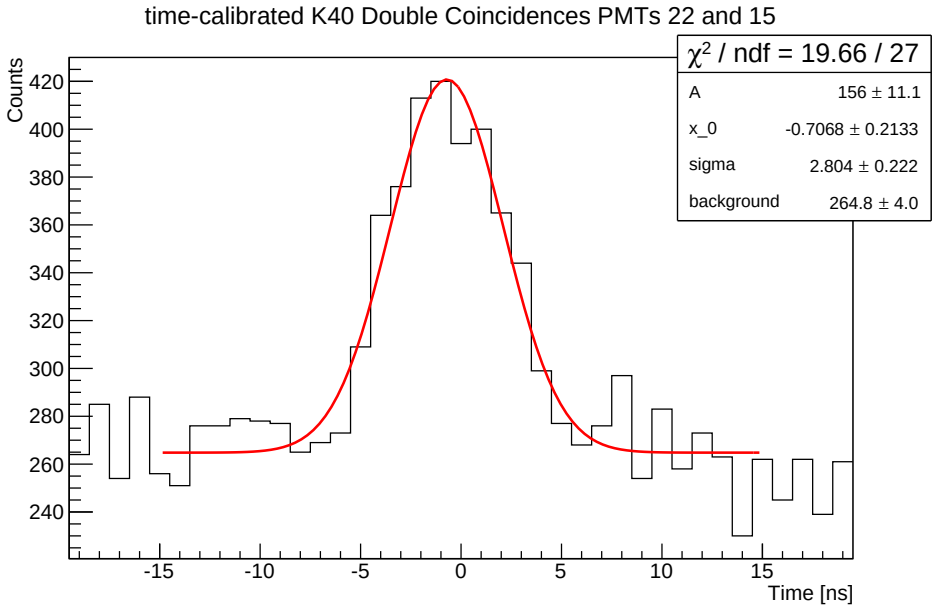

Figure 7.15: Gaussian fit to calculate the number of correlated coincidences for PMT pair 15 and 22, which are 72° apart. As this was one of the last analyses, the final time calibration has been applied, resulting in the bell curve being centred around 0 ns. The number of coincidences can be easily calculated from the parameters of the Gaussian fit or by summing the histogram values and subtracting the background.

these parameters. It is thusly ensured that the shapes and positions of the coincidence peaks are the same in all the histograms that are summed up.

In the end, the stack comprised a total of 111 runs, from run number 763 on 15th of June to run 992 on 19th of November. The aggregate run time was 111431 seconds (30 hours, 57 minutes and 11 seconds). This large statistical sample yields beautifully smooth distributions. Typical coincidence histograms for PMT separations of 32°, 60°and 120° are shown in figure 7.16. For comparison, a coincidence histogram for a PMT separation of 60° (same PMT pair as above) is shown, created using data from a single run (number 951) with a duration of 443 seconds.

7.4.1 ^{40}K Coincidence Rates

Using the method described above, the rate of coincidences caused in the PPMDOM by local ^{40}K decays was determined. As this is exactly what my simulations were about, this was the ultimate test. The results are presented in two ways:
Table 7.1 plainly shows the total coincidence rate gathered from the data stack and compares it to the expectation value gained from my simulations.
Figure 7.17 shows the coincidence rates per PMT pair. For each possible space angle between

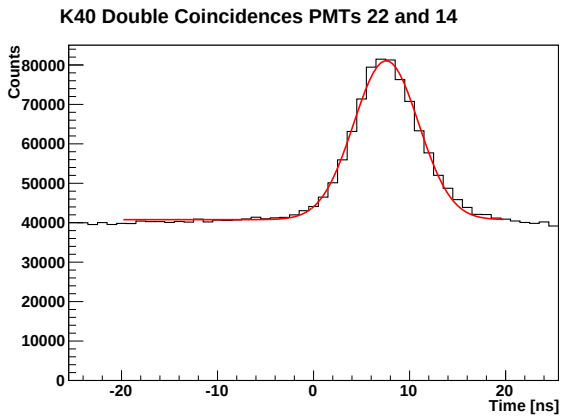

(a) stacked, PMT separation 32°

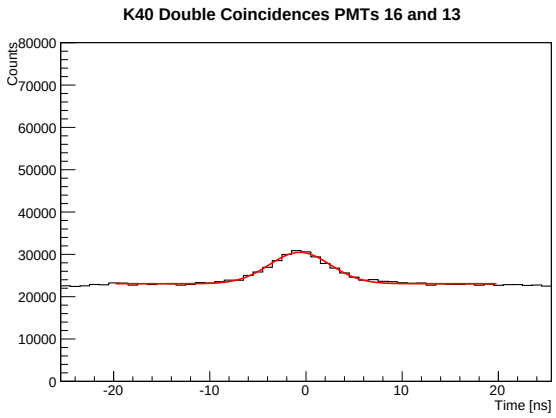

(b) stacked, PMT separation ≈ 60°

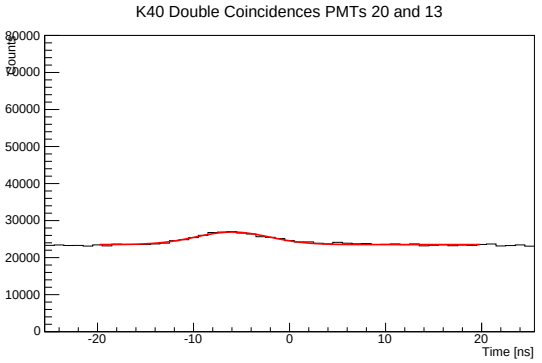

(c) stacked, PMT separation ≈ 120°

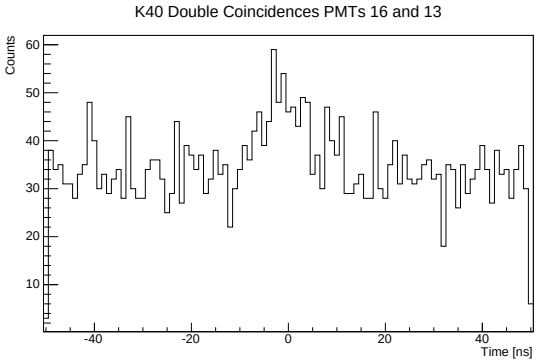

(d) single run, PMT separation ≈ 60°

Figure 7.16: Typical histograms of local ^{40}K coincidences for different PMT separations. Subfigure (d) was created from a single run, while the rest were created from a data stack of 111 runs with identical PMT operating parameters. The stack spans more than 30 hours of data taking in calm sea conditions with low bioluminescence activity. The total baseline rate of all PMTs had to be less than 300 kHz (on average 9.7 kHz per PMT) over the duration of the run for it to be included in the stack.
Only by stacking such a large number of runs was it possible to extract potassium coincidences for PMT pairs with large spatial separations. The Gaussian shaped peak of local ^{40}K coincidences is always visible above the random background contribution that is constant within the coincidence window. The number of ^{40}K coincidences is equal to the area of the Gauss bell minus the constant background.

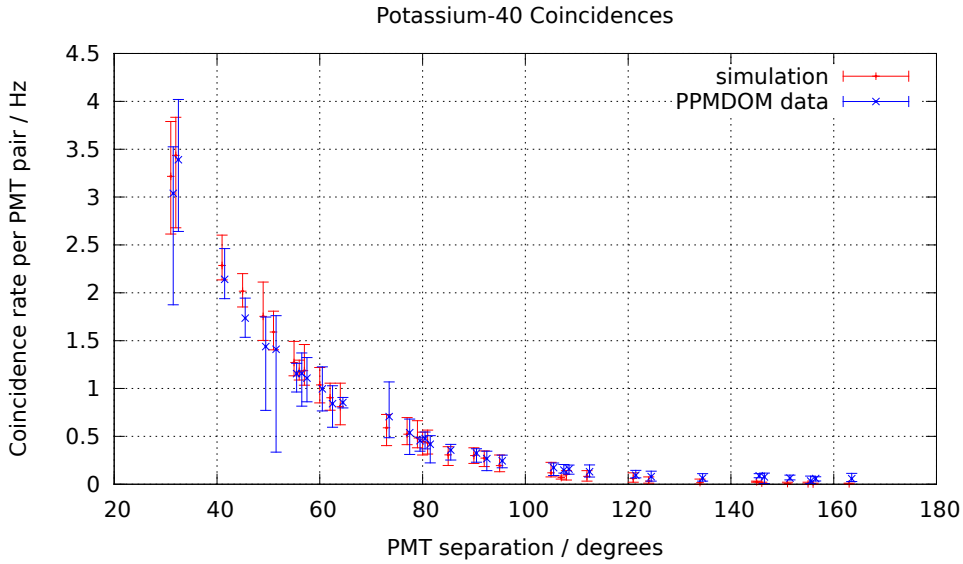

Figure 7.17: Average ^{40}K coincidence rates per PMT pair as a function of the distance between the PMTs. Simulation results are shown in red, deep-sea data is shown in blue. The good agreement confirms the validity of my simulation and its derived results.

two PMTs, the average coincidence rate was calculated and entered into a diagram. Thus, each data point shows the coincidence rate that was measured, on average, for every PMT pair with a given distance (in degrees) between them. The results of the PPMDOM data stack are depicted in blue, while the results of my simulations are shown in red.

	PPMDOM	Simulation
Local ^{40}K coincidence rate	353 ± 7 Hz	347 ± 8 Hz

Table 7.1: Comparison of coincidence rates caused by local ^{40}K decays. The left column shows the result gained from stacked data of 111 PPMDOM runs, the right column shows the corresponding value obtained with the simulation of the PPMDOM.

The result of the analysis agrees very well with the prediction from my simulation. At larger PMT separations, where the rate of potassium coincidences should be next to zero, a small amount of correlated coincidences remains. It may be that a small fraction of the constant rate bioluminescence background, assumed to be caused by bacteria, is not of a single photon nature, but consists of multiple simultaneously emitted photons, which may be detected correlatedly in two PMTs, similarly to local ^{40}K decays. Bioluminescence outbursts, which would probably be strongly correlated, have been excluded by considering only two- and threefold coincidences and by carefully choosing only good sea conditions for the data stack.

7.4.2 Trigger Rates

The selection criteria for the high quality runs used in the data stack have been described before. Figure 7.18(a) shows the total PMT trigger rate of the OM (the L0 rate of the OM) and the total baseline rate (the sum of the baseline rates of all PMTs). If the L0 rate is significantly higher than the baseline, it means that there were many bioluminescence outbursts during that run. As these outbursts can be suppressed in the analysis, the more lenient baseline rate was chosen as the quality criterion for the data stack.
In figure 7.18(a) the extracted local ^{40}K coincidence rate for each run are shown superimposed on the L0 rate. While the number of falsely counted coincidences increases with the L0 rate, it is evident that the calculated ^{40}K coincidence rate is still fairly robust against a high L0 rate. This is helped by the fact that for this run-by-run analysis, only PMT pairs with a separation of less than 90°were considered, for the reasons described above. That is also the reason why the measured ^{40}K rate is usually lower than the simulated ^{40}K rate indicated by the blue line.

7.4.3 Time Calibration

The time calibration described earlier has been performed using the high quality data stack. Due to the large statistical sample the resulting Gaussian fits are very well defined, so the errors should be negligibly small – assuming that the time offsets do not shift over time, for which there has been no indication. The time offsets are tabulated in the appendix in figure A.10 As mentioned before, this time calibration was used in analyses that required precise timing.
Figure 7.19 shows the result of the stacked time calibration overlaid with the five sample runs shown in figure 7.7.

7.4.4 Pointing

The pointing algorithm using probability maps has been used on the data stack. The resulting skymaps show how many events of a certain brightness were observed coming from every direction, observed from the frame of reference of the PPMDOM. Figure 7.20 shows a comparison of the skymaps for 3-fold to 7-fold coincidences.

As before, lower level coincidences (≤ 5) seem to arrive mainly from below the OM equator, while higher coincidence levels arrive from above.
The latter is expected, knowing that atmospheric muons create bright Cherenkov cones, whose photons arrive at the OM preferably from above the equator. The shadow of the electronics container supporting the PPMDOM is clearly visible.
For lower coincidence levels, which should be caused mainly by random coincidences, one would expect a uniform distribution over the lower OM half, with visible granularity due to the limited number of combinations and a blind area on top where the heatsink is located.
The skymap for 3-fold coincidences shows significant clustering in the area where the electronics container is located. This would be compatible with the theory that bioluminescent organisms

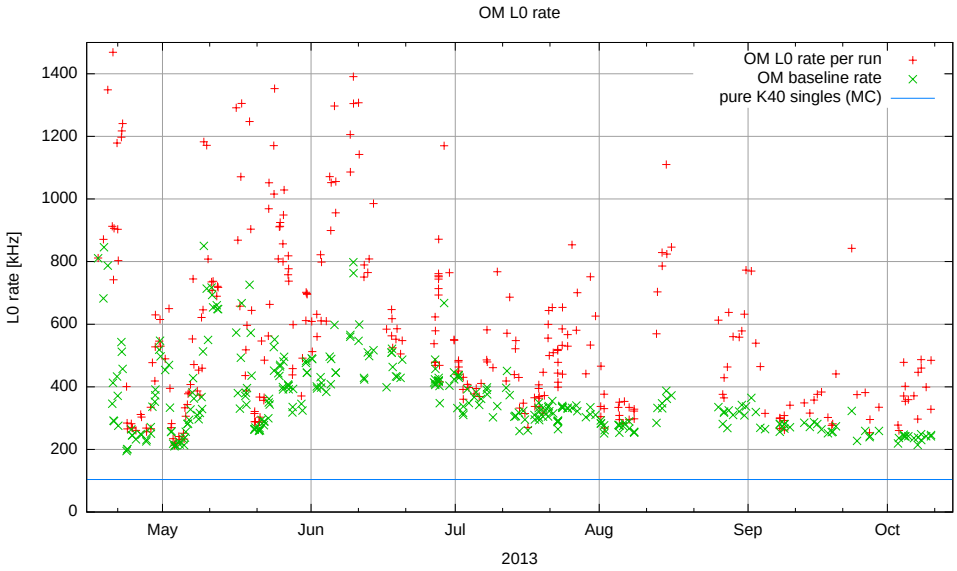

(a) L0 and baseline rate

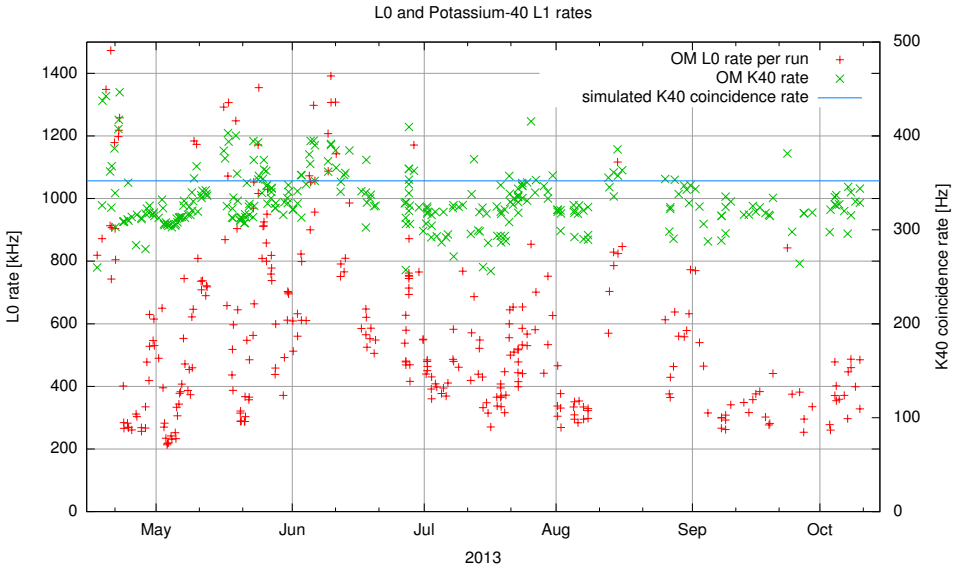

(b) L0 and K40 rate

Figure 7.18: Sea conditions during the time of my measurements. Above I show the L0 rate of the OM and the baseline rate for every run considered in my analyses. The blue line shows the expected L0 rate (rate of single PMT triggers) caused purely by ^{40}K, as obtained from my simulations.
Below I show the correlation between the L0 rate and the calculated ^{40}K coincidence rates, which are rather robust against high bioluminescence background. Due to the short run durations, only PMT pairs closer than 90° apart in the OM were considered in the coincidence count. The ^{40}K rate is therefore usually lower than the prediction.

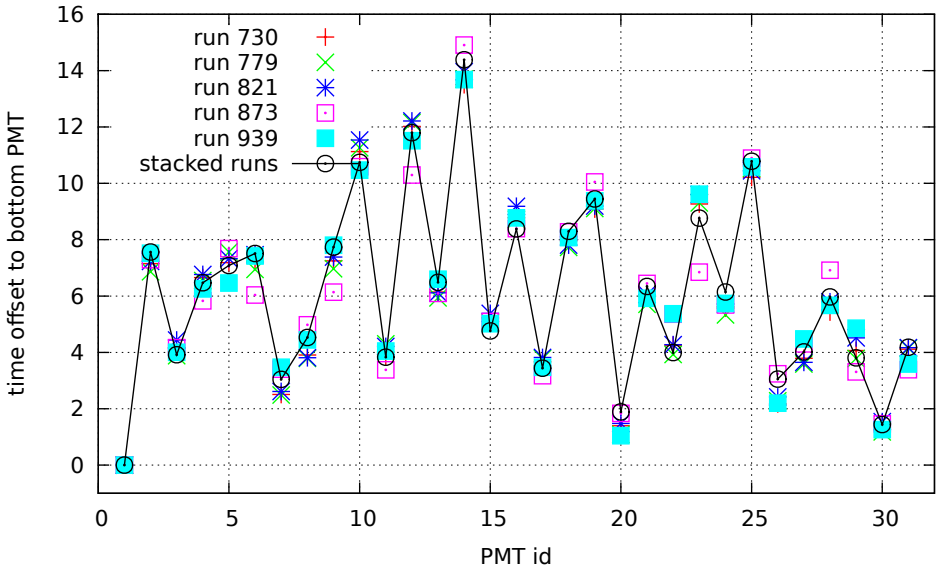

Figure 7.19: Comparison of the single run time calibrations shown earlier with the calibration created from the data stack. The results of the stacked calibration, shown in black and connected by solid lines for better legibility, lie within the expected spread of the values of the single run calibrations.

can get excited when hitting a solid structure, emitting a burst of light. The cause of the large number of 4-fold and 5-fold coincidences that seem to originate below the OM is unknown.

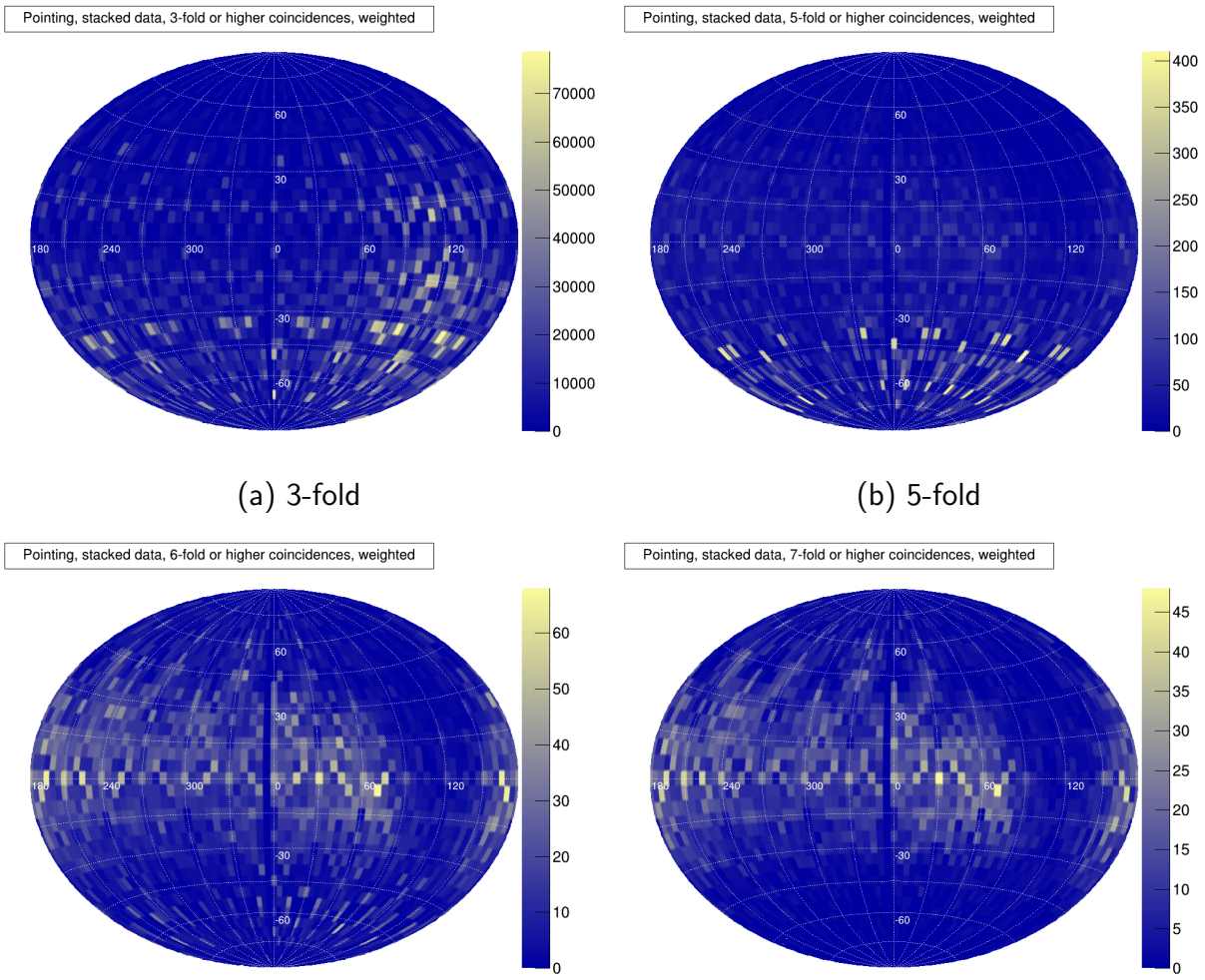

(a) 3-fold

(b) 5-fold

(c) 6-fold

(d) 7-fold

Figure 7.20: Skymaps created from the data stack for coincidences of different brightness, i.e. number of PMTs that have been triggered in coincidence. The coordinates are given from the point of view of the PPMDOM, as there was no way to determine the actual orientation of the OM.
Up to a coincidence level of 5 the sources seem to be below the OM. A lot of level 3 coincidences originate from the cable and the electronics box, which is consistent with a theory based on observations in ANTARES that bioluminescent organisms emit light when they hit a solid structure. Level 6 and 7 coincidences arrive from above, consistent with the expected Cherenkov light from atmospheric muons. The shadow of the electronics container is clearly visible.
The distribution of level 4 coincidences is very similar to that of level 5 and has been omitted for clarity.

Chapter 8

Summary

8.1 Neutrino Telescopes

Neutrino "telescopes" are particle detectors constructed with the goal to detect neutrinos of extra-terrestrial origin. To this end they have to be able to record the arrival direction and the kinetic energy of each neutrino.
Neutrinos are created wherever protons or nuclei interact with photons or matter. Possible sources may be supernova remnants, active galactic nuclei, or the GZK effect. Neutrinos are highly penetrating and only rarely interact with matter, in which case they are usually destroyed (i.e. changed into another particle). This means that neutrinos that reach Earth point back to their point of creation. If the kinetic energy of a neutrino is high enough and it interacts close to the detector, it may be detected and its arrival direction observed. With a somewhat lower precision, the energy of the neutrino can be estimated.
Detected neutrinos can be visualised as points on a skymap, which is a projection of the sky where each direction as seen from Earth is mapped to a point in the skymap. After sufficient exposure time, the experimenters will (hopefully) arrive at a skymap that shows neutrino sources (points in the sky from which a sufficient number of neutrinos have arrived so that it is unlikely that this can happen by random chance), and have an energy spectrum that fits theoretical predictions.

Neutrino telescopes need to be built into a transparent medium like water or ice. They need a very large instrumented volume, so natural bodies of water or ice are needed. They need to be dark, thus they have to be built deep enough within the water or ice that no daylight can reach them. And they have to be shielded against natural and cosmic radiation, especially the muons created in the atmosphere, which again means that they have to be built deep, and if possible accompanied by veto detectors.

In this summary I will concentrate on neutrino telescopes built in the deep sea, having been a member of the ANTARES collaboration operating the first deep sea neutrino telescope, and of the KM3NeT collaboration, currently building a successor to ANTARES.

Deep sea neutrino telescopes are three-dimensional grids of highly sensitive optical sensors placed on the bottom of the sea. The detector grid is realised by buoy-topped cables anchored to the seafloor at a depth of several kilometres, with the cables reaching up by several hundred metres. In ANTARES/ KM3NeT jargon, the cables are called "lines" or "detection units". The distance between neighbouring lines is around 60 metres in ANTARES.
The cables carry the sensors, called optical modules (OMs), at regular intervals, starting from a certain height above the seafloor in clean water. The line thus has a given number of "storeys" or "floors". The optical modules basically consist of photomultiplier tubes (PMTs, sensors able to detect single photons) placed inside a glass sphere built for high external pressure. Auxiliary electronics can be integrated in the sphere or in an external container.
Sometimes a neutrino with a high kinetic energy interacts with matter in or near the neutrino telescope. The result is always a charged lepton (electron, muon or tauon, or their antiparticles) travelling at relativistic speed. The interaction can also cause localized electromagnetic showers. All this leads to the emission of light, mostly via the Cherenkov effect, at the interaction point and/or along the trajectory of the lepton. The optical modules detect this light. By timing the arrival of photons at different points in the detection grid, the position and trajectory of the light source can be calculated ("reconstructed"). For this to work, the data acquisition has to be able to provide nanosecond time resolution.
Apart from the desired but rare signal of neutrino interactions, a lot of background light from various sources is present even in the darkness of the deep sea. The most prominent and varied source is bioluminescence. A number of microscopic and macroscopic lifeforms that live in the deep emit light. Depending on the circumstances and season, the magnitude of this background can vary from a low and constant source of single, uncorrelated photons that are easy to filter out, to wildly varying photon rates high enough that the detector has to be shut down in order to preserve the photomultipliers.
More predictable background light comes from the decay of long-lived radioactive isotopes of the various salts dissolved in sea water. The most important one is the β-decay of ^{40}K with an activity of about 13 Bq per litre. The emitted electrons possess a kinetic energy of up to 1.3 MeV, which is more than sufficient to create Cherenkov light.
Another source of Cherenkov light are atmospheric muons that can easily reach several kilometres deep into the earth or sea. Even though these are detected in the same way as a muon neutrino would be, in the context of neutrino astronomy these muons have to be considered as background. They do have their use as a means to calibrate the detector and develop reconstruction techniques.
The intrinsic noise of the PMT is of less importance, partly because it is relatively easy to filter out, but also because the PMTs are specifically developed and chosen for a low dark rate.

The existing ANTARES neutrino telescope, located around 40 km to the south of Toulon and 2.4 km below the surface, uses optical modules consisting of a single large photomultiplier tube. Each storey has three of these modules arranged around a central electronics container. For the future KM3NeT, a new, slimmer design has been chosen. Each storey will only house a single optical module, which will also incorporate all the auxiliary electronics. The module will

have 31 small PMTs within a glass sphere of 43 cm diameter. This multi-PMT optical module has several advantages. The sensitive area is more than twice as large as with the previous solution, and its segmentation opens up new possibilities for background suppression and the reconstruction of tracks and localized light sources.

8.2 Goals of my Thesis

Simulation

My thesis started out as a simulation project to determine the signature of ^{40}K background in the new optical module. While the photon rate in each PMT caused by ^{40}K can be calculated, the more interesting piece of information is the correlation between photons caused by a single decay. When a ^{40}K decay occurs close to the OM, it is very likely that several photons from that one decay arrive at (almost) the same time and trigger multiple PMTs. If these coincidences create a typical pattern, it is possible to use that for background filtering and in-situ calibration.

To generate this information, I created first a simplefied, then a very detailed computer model of the optical module, using the particle physics simulation toolkit GEANT 4. All available data on the optical properties of sea water (among others from measurements at the ANTARES site), as well as those of the glasses and contact gel found in the optical module, have been entered into the simulation.
Depending on the simulation parameters, it was possible to take a look at the big picture, which is the total background rate induced by ^{40}K decays, or run detailed simulations of decays occurring close to the optical module.
A derivative of the main simulation was used for detailed sensitivity studies of the virtual OM.

Data Taking and Analysis

In April 2013 the first pre-production model of the multi-PMT digital optical module (PPMDOM) was integrated into the auxiliary instrumentation line of the ANTARES detector. Until October I was part of the small group that operated the PPMDOM, performed measurements and analysed the data. My primary goal was to use the results of my simulations to develop an internal time calibration, which included a comparison of my predictions to real-world data. I also took first steps towards making use of the segmented sensitive area to point back to the source of a light pulse.

8.3 Simulation Results

Two sets of final simulations were run. One set simulated the final version of the OM that will be used in the construction of KM3NeT, feeding information to the larger-scale sensitivity studies. The other set specifically recreated the PPMDOM, which has PMTs and therefore a smaller sensitive area.

Trigger Rates

The expected background photon rate caused by ^{40}K is 128 kHz for the final version of the OM, or 4.1 kHz per PMT. For the PPMDOM with a slightly smaller sensitive area, the predicted single photon rate is 97 kHz for the whole module or 3.1 kHz per PMT.

Hit Patterns and Coincidence Rates

The ^{40}K coincidence rate for each PMT pair can be readily extracted from the simulation. Simply put, the closer two PMTs are together in the OM, the more coincidences from nearby decays occur in them.
Due to the short distance a β-electron travels in water, all its Cherenkov light emanates from virtually a single point. Taking into account the dimensions of the module, all photons from a nearby decay arrive nearly simultaneously, less than 1 ns apart. The most common case is two photons registered in two directly neighbouring PMTs. The farther apart the two PMTs are, the less common the coincidences become. Coincidences with three or more PMTs are about an order of magnitude less common and have been treated as a two-fold coincidence, where the first two PMTs that were triggered dictated the pair.
For the final OM version, the rate of coincidences caused by nearby ^{40}K decays, which generate a signal that can be used for calibration, is predicted at 564 Hz. In the PPMDOM, I expect 347 Hz.

Sensitivity of the Optical Modules

Due to high level of detail of my simulation, it was possible to determine the sensitivity of each PMT within the OM as a function of the direction of incoming light. This information was necessary for my pointing trials.

8.4 Measurement Results

Trigger Rates

The single photon hit rates from ^{40}K cannot be separated from the trigger rate caused by bioluminescence and internal PMT noise. The total background rate varies greatly according to sea conditions and has been observed between 240 kHz on a calm day and more than 1 MHz in bad conditions.

Hit Patterns and Coincidence Rates

The PPMDOM lacked a proper time synchronisation between the PMTs, which meant that each PMT had a certain fixed time offset, which was shown to be up to 15 ns between two PMTs. Using the knowledge that ^{40}K photons arrive simultaneously, it was possible to perform a relative time calibration between all PMTs. This is necessary for advanced analyses, where the coincidence window has to be as short as possible to minimize noise influences. Furthermore, the rate of coincidences for each PMT pair can be extracted from the same analysis.
The final analysis, which was performed on a large data stack taken in good sea conditions, yields a coincidence rate of 353 Hz from nearby ^{40}K decays, which compares very well to the corresponding rate of 347 Hz from the simulation. The spatial distribution agrees very well with the prediction. I therefore considered my simulation validated and went on to the next step.

Pointing

Using the sensitivity of each PMT as a function of the direction of incoming light, I devised a pointing algorithm that could estimate the direction from the OM to a light source. If a sufficient number of photons, i.e. more than for a common random coincidence, arrives at the OM within a few nanoseconds, the hit pattern can be used to create a probability map for the direction of the light source. This scheme should work well for short flashes of light, like the Cherenkov cone of a passing muon.
Only limited development and testing could be accomplished within the short time available to me. Using data from when the ANTARES calibration beacons were flashing, my analysis clearly shows that it is possible to point at a bright light source using even the PPMDOM hardware. With the production model of the OM, significant refinements could be possible. At the very least, the pointing algorithm can provide a solid set of starting parameters for higher-level track reconstruction algorithms, which may improve the speed and quality of those analyses.

Appendix A

Additional Tables and Figures

A.1 Simulation Parameters

The optical properties of the simulated sea water are taken from the reference document of the KM3NeT simulation working group [5]. Absorption and scattering lengths are found there in tabulated form, while for the refractive index a parameterisation has been given:

$$n(\lambda) = a_0 + a_1 P + \frac{1}{\lambda}(a_2 + \frac{1}{\lambda}(a_3 + \frac{1}{\lambda}a_4)) \tag{A.1}$$

where λ is the photon wavelength, P is the water pressure in bar, and the coefficients are as follows: $a_0 = 1.3201$; $a_1 = 1.4 \times 10^{-5}$; $a_2 = 16.2566$; $a_3 = -4383.0$; $a_4 = 1.1455 \times 10^6$. For all simulations in the context of this thesis, the refractive index has been calculated for a pressure of 350 bars, which corresponds to the depth at the Capo Passero site.
Table A.1 lists the absoption and scattering lengths given in [5] and part of the calculated refractive indices at a number of wavelengths. For the simulation, n has been calculated in steps of 10 nm over the range of 290 – 720 nm. A graphical representation is given in figure 6.5.

The quantum efficiency of the PMTs, used in the analysis step, is also defined in the simulation reference document. It is listed in table A.3 and shown in figure 6.6. These values are based on measurements conducted in the photodetection laboratory at the Erlangen Centre for Astroparticle Physics.

λ / nm	E_γ / eV	n	L_{abs} / m	L_{sc} / m
290	4.28	1.376	0.0	16.6
310	4.00	1.370	11.9	20.2
330	3.76	1.366	16.4	23.8
350	3.54	1.363	20.6	27.6
370	3.35	1.360		
375	3.31		29.5	32.5
390	3.18	1.357		
410	3.02	1.355		
412	3.01		48.5	40.2
430	2.88	1.354		
440	2.82	1.353	67.5	46.2
450	2.76	1.352		
470	2.64	1.351		
475	2.61		59.0	53.9
488	2.54		55.1	56.8
490	2.53	1.350		
510	2.43	1.349	26.1	61.8
530	2.34	1.348		
532	2.33		19.9	66.8
550	2.25	1.347		
555	2.23		14.7	72.1
610	2.03	1.345		
650	1.91	1.344	2.8	94.2
670	1.85	1.343		
676	1.83		2.3	100.3
690	1.80	1.343		
710	1.75	1.343		
715	1.73		1.0	109.4
720	1.72	1.342	0.0	109.4

Table A.1: Optical properties of the simulated sea water. Listed are refractive index n, absorption length L_{abs} and scattering length L_{sc} associated with each wavelength λ or photon energy E_γ. GEANT 4 uses a cubic spline interpolation between the data points given for any material property. Note that not all interpolated values of n are shown here.

Element	Fraction / %
Oxygen	85.84
Hydrogen	10.82
Chlorine	1.94
Sodium	1.08
Magnesium	0.1292
Sulfur	0.091
Calcium	0.04
Potassium	0.04
Bromine	0.0067
Carbon	0.0028

Table A.2: Composition of the simulated sea water. Fractions are given in mass percentages. Carried over from the ^{40}K simulation by Daniel Goering [31]. No source can be given, as the original source code and the report by D. Goering is no longer available to the author. Supposedly, the data came from analysis of sea water samples taken at the ANTARES site. Several such surveys were conducted by the ANTARES and KM3NeT collaborations at the ANTARES site and the candidate sites for KM3NeT.

λ / nm	QE / %	λ / nm	QE / %
290	3.1	470	21.1
300	9.8	480	19.6
310	17.5	490	18.5
320	23.2	500	17.2
330	26.5	510	15.4
340	28.1	520	12.1
350	28.1	530	9.3
360	29.1	540	7.2
370	30.1	550	6.2
380	30.4	560	4.6
390	30.1	570	3.6
400	29.9	580	2.8
410	29.3	590	2.1
420	28.6	600	1.3
430	27.5	610	0.8
440	26.5	620	0.5
450	25.0	630	0.3
460	23.2	640	0

Table A.3: Quantum efficiency of the simulated PMTs as used in the analysis, taken from [5].

photon energy / eV	n	λ / m
1.722	1.47	0
2.034	1.47	0.53
2.068	1.47	0.54
2.103	1.47	0.58
2.139	1.47	0.65
2.177	1.47	0.75
2.216	1.47	0.73
2.256	1.47	0.65
2.298	1.47	0.63
2.341	1.47	0.60
2.386	1.47	0.60
2.433	1.47	0.58
2.481	1.47	0.58
2.532	1.47	0.50
2.585	1.47	0.42
2.640	1.47	0.40
2.697	1.47	0.38
2.757	1.47	0.35
2.820	1.47	0.36
2.885	1.47	0.36
2.954	1.47	0.35
3.026	1.47	0.45
3.102	1.47	0.59
3.181	1.47	0.61
3.265	1.47	0.60
3.353	1.47	0.30
3.446	1.47	0.55
3.545	1.47	0.40
3.649	1.47	0.20
3.760	1.47	0.10
3.877	1.47	0.05
4.002	1.47	0.03
4.136	1.47	0.01
4.276	1.47	0.00

Table A.4: Index of refraction n and absorption length λ of the glass of the OM sphere. These values have been taken from a simulation of the ANTARES OM by Heide Constatini, sent to author by email. The manufacturer of the glass shells used for KM3NeT did not reply to requests for detailed data.

photon energy / eV	n	λ / m
1.722	1.404	0
2.034	1.404	0.975
2.13	1.404	0.975
2.18	1.404	0.966
2.22	1.404	0.935
2.25	1.404	0.890
2.3	1.404	0.898
2.34	1.404	0.876
2.43	1.404	0.844
2.53	1.404	0.786
2.67	1.404	0.727
2.79	1.404	0.674
3.1	1.404	0.566
3.28	1.404	0.485
3.56	1.404	0.360
3.77	1.404	0.220
4.136	1.404	0.220
4.276	1.404	0

Table A.5: Index of refraction n and absorption length λ of the optical gel. These values have been taken from a simulation of the ANTARES OM by Heide Constatini, sent to author by email. No detailed information on the gel actually used in KM3NeT could be procured.

Physics Process	e^-	e^+	γ	Photon	Ion
Photoelectric Effect			+		
Compton Scattering			+		
Pair Production			+		
Rayleigh Scattering			+		
Electron Scattering	+	+			
Ionisation	+	+			
Bremsstrahlung	+	+			
Annihilation		+			
Cherenkov Radiation	+	+			
Radioactive Decay					+
Absorption				+	
Scattering (custom)				+	
Boundary				+	

Table A.6: List of physics processes enabled in the ^{40}K simulation, and to which particle each process or process archetype applies. For details to each process, please refer to the GEANT 4 documentation [1]. The physics list module used in the ^{40}K simulation is based on examples supplied with the GEANT 4 distribution.

wavelength / nm	transmission / %
290	0
360	0
367	1.3
371	4
374	6.6
380	19
386	50
391	70
395	80
400	86.4
406	90
416	92.2
450	92.3
720	92.3

Table A.7: Transmission versus wavelength of a 2 mm piece of PMMA used for the simulation of the reflectors. These values have been derived from measurements by C. Joram [9] and cross-correlated to measurements at the ECAP by Lew Classen and Jonas Reubelt. The absorption length L(λ) required as input for GEANT 4 was calculated from the transmission T(λ) thusly: $L(\lambda) = \frac{2\,mm}{log\,\frac{92.4}{T(\lambda)}}$.

$\cos\phi$	A_{eff}/mm^2
-1.0	7100
-0.95	6589
-0.9	5876
-0.85	5212
-0.8	4597
-0.75	4096
-0.7	3685
-0.65	3347
-0.6	3042
-0.55	2791
-0.5	2549
-0.45	2294
-0.4	2067
-0.35	1831
-0.3	1608
-0.25	1402
-0.2	1193
-0.15	996
-0.1	806
-0.05	626
0.0	459
0.05	311
0.1	184
0.15	85
0.2	18
0.25	0

Table A.8: Results of my acceptance simulation that were used as input for other simulations. It shows the effective area A_{eff} of a generic PMT with light collecting collar within the DOM, as a function of the cosine of the angle of incidence ϕ. A cosine of -1 corresponds to a head-on incidence.

A.2 PpmDOM Characteristics

PMT	θ / rad	ϕ / rad	θ / °	ϕ / °	PPMDOM ID
1	π	-	180	-	22
2	2.582	0	147.9	0	14
3	2.582	$^1/_3\,\pi$	147.9	60	18
4	2.582	$^2/_3\,\pi$	147.9	120	26
5	2.582	π	147.9	180	24
6	2.582	$^4/_3\,\pi$	147.9	240	25
7	2.582	$^5/_3\,\pi$	147.9	300	19
8	2.162	$^1/_6\,\pi$	123.9	0	13
9	2.162	$^3/_6\,\pi$	123.9	60	17
10	2.162	$^5/_6\,\pi$	123.9	120	20
11	2.162	$^7/_6\,\pi$	123.9	180	28
12	2.162	$^9/_6\,\pi$	123.9	240	29
13	2.162	$^{11}/_6\,\pi$	123.9	300	21
14	1.872	0	107.3	0	12
15	1.872	$^1/_3\,\pi$	107.3	60	16
16	1.872	$^2/_3\,\pi$	107.3	120	27
17	1.872	π	107.3	180	30
18	1.872	$^4/_3\,\pi$	107.3	240	23
19	1.872	$^5/_3\,\pi$	107.3	300	15
20	1.270	$^1/_6\,\pi$	72.8	0	10
21	1.270	$^3/_6\,\pi$	72.8	60	11
22	1.270	$^5/_6\,\pi$	72.8	120	1
23	1.270	$^7/_6\,\pi$	72.8	180	2
24	1.270	$^9/_6\,\pi$	72.8	240	3
25	1.270	$^{11}/_6\,\pi$	72.8	300	6
26	0.980	0	56.1	0	9
27	0.980	$^1/_3\,\pi$	56.1	60	7
28	0.980	$^2/_3\,\pi$	56.1	120	5
29	0.980	π	56.1	180	0
30	0.980	$^4/_3\,\pi$	56.1	240	4
31	0.980	$^5/_3\,\pi$	56.1	300	8

Table A.9: Positions of the PMTs in the KM3NeT Digital Optical Module, taken from [5]. The spherical coordinates give the direction into which each tube points, within the frame of reference of the OM, in which $\theta = 0$ points upwards. The final column shows the DAQ ID of each PMT in the PPMDOM.

PMT	Δt / ns
1	0
2	7.6
3	3.9
4	6.5
5	7.1
6	7.5
7	3.0
8	4.5
9	7.7
10	10.7
11	3.8
12	11.8
13	6.5
14	14.4
15	4.8
16	8.4
17	3.4
18	8.3
19	9.4
20	1.9
21	6.3
22	4.0
23	8.8
24	6.1
25	10.8
26	3.1
27	4.0
28	6.0
29	3.8
30	1.4
31	4.2

Table A.10: Results of the time calibration derived from the stacked data set. The time delay of each PMT with respect to the downward-pointing reference PMT is shown. The PMT numbering is the same as in the simulation (see table A.9 above).

Appendix B

Calculations

B.1 Cherenkov Spectrum

The spectrum of Cherenkov photons as a function of the wavelength can be derived from the Frank-Tamm formula (formula 2.2 in chapter 2). Starting from

$$\frac{\mathrm{d}E}{\mathrm{d}x} = \frac{e^2}{c^2}\int\left(1-\frac{1}{\beta^2 n^2}\right)\omega\ \mathrm{d}\omega$$

one substitutes λ for ω

$$\begin{aligned}\omega &= \frac{2\pi c}{\lambda}\\ \Rightarrow \frac{\mathrm{d}\omega}{\mathrm{d}\lambda} &= -\frac{2\pi c}{\lambda^2}\\ \mathrm{d}\omega &= -\frac{2\pi c}{\lambda^2}\,\mathrm{d}\lambda\end{aligned}$$

The resulting minus sign can be eliminated because the upper and lower limit of the integral are swapped if one integrates from a lower to a higher wavelength. Therefore, the result of the substitution is

$$\begin{aligned}\frac{\mathrm{d}E}{\mathrm{d}x} &= \frac{e^2}{c^2}\int\left(1-\frac{1}{\beta^2 n^2}\right)\frac{2\pi c}{\lambda}\cdot\frac{2\pi c}{\lambda^2}\,\mathrm{d}\lambda\\ \frac{\mathrm{d}E}{\mathrm{d}x} &= 4\pi^2 e^2\int\left(1-\frac{1}{\beta^2 n^2}\right)\frac{1}{\lambda^3}\,\mathrm{d}\lambda\\ \Rightarrow \frac{\mathrm{d}^2E}{\mathrm{d}x\mathrm{d}\lambda} &= 4\pi^2 e^2\left(1-\frac{1}{\beta^2 n^2}\right)\frac{1}{\lambda^3}\end{aligned}$$

As a side note, the term $1-\frac{1}{\beta^2 n^2}$ is often expressed as $\sin^2\theta$ in literature.
The number of emitted photons $\mathrm{d}N$ within the wavelength interval $[\lambda;\lambda+\mathrm{d}\lambda[$ is calculated by

dividing the emitted energy dE by the energy E_{photon} of a single photon of the wavelength λ:

$$\begin{aligned} E_{photon} &= \frac{hc}{\lambda} \\ \rightarrow dN &= \frac{dE \cdot \lambda}{hc} \\ \Rightarrow dE &= \frac{dN \cdot hc}{\lambda} \end{aligned}$$

This leads to

$$\frac{d^2N}{dx d\lambda} = \frac{4\pi^2 e^2}{hc}\left(1 - \frac{1}{\beta^2 n^2}\right)\frac{1}{\lambda^2}$$

and, using the fine structure constant $\alpha = \frac{e^2}{\hbar c} = \frac{2\pi e^2}{hc}$, yields the final shape of the equation:

$$\frac{d^2N}{dx d\lambda} = 2\pi\alpha\left(1 - \frac{1}{\beta^2 n^2}\right)\frac{1}{\lambda^2}$$

B.2 Coincidence Rates and Error Propagation

In chapter 6, section 6.2.5, I list the rate of coincidences of different levels (2 to 5-fold) derived from the simulation. These rates were calculated under the hypothesis that the majority of the ^{40}K Cherenkov light arrives at the optical module in an uncorrelated manner, purely random in time and space. Only the number of hits that were counted in each PMT (on average) was used for this calculation.
Comparing these figures with the actual coincidence rates and patterns quickly disproves this random background theory. However, in a real neutrino telescope, there are several sources of purely random background noise, e.g. electronic noise and bioluminescence (the latter of which also has non-random correlated components). Therefore, the calculations of coincidence rates from random background sources are detailed here.

The calculation of the average PMT rate is trivially done by taking the total number of registered hits in the OM N_{OM}, and dividing this figure by the number of PMTs (31) and the duration T of the data run or simulation run. This of course assumes that all PMTs are created equal. For the simulation, this assumption is certainly warranted. In the real detector, quality assurance of the PMTs and regular calibration of the PMTs in situ will also ensure that the PMT rates are approximately equal, at least within a single OM.

The rate of twofold coincidences can then be calculated thusly (compare section 6.2): where $N_{PMT} = \frac{1}{31} \times N_{OM}$ is the average number of hits per PMT and Δt_c is the length of the coincidence window.

$$R_{2\times} = \frac{1}{T} \times 31 \times N_{PMT} \times \frac{1}{T} \times 30 \times N_{PMT} \times \Delta t_c = \frac{31 \times 30}{T^2} \times N_{PMT}^2 \times \Delta t_c,$$

Gaussian error propagation yields an uncertainty of

$$\Delta R_{2\times} = \frac{2 \times 31 \times 30}{T^2} \times \Delta t_c \times N^{\frac{3}{2}},$$

where the uncertainty of the number of hits per PMT ΔN_{PMT} is equal to its square root $\sqrt{N_{PMT}}$.

The rate of threefold coincidences is equal to the rate of double coincidences multiplied by the chance that another random photon hit occurs within the remaining coincidence window. The arrival times of the second photons of twofold coincidences are distributed uniformly within the coincidence window. Therefore, on average, the third photon has a remaining window of half the length of the coincidence window:

$$\begin{aligned} R_{3\times} &= R_{2\times} \times \frac{29 \times N_{PMT}}{T} \times 0.5\Delta t_c \\ &= \frac{31 \times 30}{T^2} \times N_{PMT}^2 \times \Delta t_c \times \frac{29 \times N_{PMT}}{T} \times 0.5\Delta t_c \\ &= \frac{31 \times 30 \times 29}{T^3} \times N_{PMT}^3 \times 0.5\Delta t_c^2 \end{aligned}$$

From this, the uncertainty is calculated as

$$\Delta R_{3\times} = \frac{3 \times 31 \times 30 \times 29}{T^3} \times 0.5\Delta t_c^2 \times N^{\frac{5}{2}}.$$

For each further photon, the remaining coincidence window will be – on average – half again the remaining coincidence window of the previous photon. Consequently, the expected rates of fourfold and fivefold coincidences from a purely random background are:

$$\begin{aligned} R_{4\times} &= \frac{31 \times 30 \times 29 \times 28}{T^4} \times N_{PMT}^4 \times \frac{1}{4 \times 2}\Delta t_c^3 \\ \Delta R_{4\times} &= \frac{4 \times 31 \times 30 \times 29 \times 28}{T^4} \times \frac{1}{4 \times 2}\Delta t_c^3 \times N^{\frac{7}{2}} \\ R_{5\times} &= \frac{31 \times 30 \times 29 \times 28 \times 27}{T^5} \times N_{PMT}^5 \times \frac{1}{8 \times 4 \times 2}\Delta t_c^4 \\ \Delta R_{5\times} &= \frac{5 \times 31 \times 30 \times 29 \times 28 \times 27}{T^5} \times \frac{1}{8 \times 4 \times 2}\Delta t_c^4 \times N^{\frac{9}{2}}. \end{aligned}$$

Bibliography

[1] http://geant4.cern.ch/

[2] http://geant4.web.cern.ch/geant4/support/datafiles_origin.shtml

[3] http://commons.wikimedia.org/wiki/User:Harp

[4] L. Fülöp, T. Biró, Cherenkov Radiation Spectrum. International Journal of Theoretical Physics, Vol. 31, No. 1, 1992

[5] Reference Document of the KM3NeT simulation working group, KM3NeT internal document KM3NeT_SIM_2014_001-Simulations_and_Astrophysics_WorkingDocument_v3.2.pdf

[6] D. Saltzberg, P.W. Gorham et al., Observation of the Askaryan Effect, RADHEP-2000, accessible at http://www.physics.ucla.edu/~moonemp/radhep/proc/proc.html

[7] F. Halzen, S. R. Klein, Astronomy and astrophysics with neutrinos; Physics Today 61(5), 29 (2008); doi: 10.1063/1.2930733

[8] The ANTARES Collaboration, ANTARES: the first undersea neutrino telescope; arXiv:1104.1607 [astro-ph.IM]

[9] C. Joram, Transmission curves of plexiglass (PMMA) and optical grease, CERN PH-EP Technical Notes, https://cds.cern.ch/record/1214725/files/PH-EP-Tech-Note-2009-003.pdf

[10] Refractive index database, information on PMMA at http://refractiveindex.info/?group=PLASTICS&material=PMMA

[11] M. Anghinolfi, H. Costantini, K. Fratini, M. Taiuti, Simulations of the ^{40}K noise in the ANTARES environment with GEANT 4, ANTARES Internal Note ANTARES-PHYS-2008-001

[12] http://baikalweb.jinr.ru/

[13] D. E. Groom, N. V. Mokhov, and S. Striganov, Muon Stopping Power and Range Tables 10 MeV—100 TeV, Atomic Data and Nuclear Data Tables, Vol. 76, No. 2, July 2001

[14] https://icecube.wisc.edu

[15] http://km3net.org/

[16] http://cc.in2p3.fr

[17] KM3NeT, Conceptual Design for a Deep-Sea Research Infrastructure Incorporating a Very Large Volume Neutrino Telescope in the Mediterranean Sea, KM3NeT consortium, May 2008

[18] KM3NeT, Technical Design Report for a Deep-Sea Research Infrastructure in the Mediterranean Sea Incorporating a Very Large Volume Neutrino Telescope, KM3NeT consortium, April 2010

[19] Laura Mgrdichian, AMANDA's First Six Years, http://phys.org/news123497018.html

[20] Conference proceedings of the VLVνT 2013 (Very Large Volume Neutrino Telescope), available at http://agenda.albanova.se/conferenceDisplay.py?confId=3930

[21] R. Bormuth, L. Classen, Oleg Kalekin, H. Peek, J. Reubelt, D. Samtleben, E. Visser, and KM3NeT collaboration , Characterization of the ETEL and HZC 3-inch PMTs for the KM3NeT project , AIP Conference Proceedings 1630, 114 (2014); doi: 10.1063/1.4902785

[22] S. Aiello, L. Classen, V. Giordano, Oleg Kalekin, E. Leonora, H. Peek, J. Reubelt, D. Samtleben, E. Visser, and KM3NeT collaboration, Characterization of the 80-mm diameter Hamamatsu PMTs for the KM3NeT project, AIP Conference Proceedings 1630, 118 (2014); doi: 10.1063/1.4902786

[23] Ulrich F. Katz and KM3NeT Collaboration, News from KM3NeT, AIP Conference Proceedings 1630, 38 (2014); doi: 10.1063/1.4902767

[24] IceCube Collaboration, First observation of PeV-energy neutrinos with IceCube, arXiv:1304.5356v2 [astro-ph.HE], doi: 10.1103/PhysRevLett.111.021103

[25] IceCube Collaboration, Evidence for High-Energy Extraterrestrial Neutrinos at the IceCube Detector, arXiv:1311.5238v2 [astro-ph.HE], doi: 10.1126/science.1242856

[26] IceCube Collaboration, Observation of High-Energy Astrophysical Neutrinos in Three Years of IceCube Data, arXiv:1405.5303v2 [astro-ph.HE], doi: 10.1103/PhysRevLett.113.101101

[27] Hamamatsu Photonics K. K., Photomultiplier Tubes, Basics and Applications, Third Edition (Edition 3a), retrieved on 2015-06-04 from https://www.hamamatsu.com/resources/pdf/etd/PMT_handbook_v3aE.pdf

[28] Hamamatsu Photonics, https://www.hamamatsu.com

[29] B. Herold, O. Kalekin, PMT characterisation for the KM3NeT project, 10.1016/j.nima.2010.04.129, Nucl. Instrum. Meth. A **626-627**, S151 (2011)

[30] H. Constatini, source code for simulation of ANTARES optical module, received via email on 2009/06/19

[31] D. Goering, student's project work, source code for simulation of ^{40}K decay in water, received from R. Shanidze in October 2008 as starting point for author's studies.

[32] The KM3NeT Collaboration, Deep sea tests of a prototype of the KM3NeT digital optical module; arXiv:1405.0839v2 [astro-ph.IM]

[33] `https://root.cern.ch/`

[34] C. Kopper, source code for optical scattering process for GEANT 4, received via email on 2011/01/25

[35] C. L. Cowan, F. Reines, F. B. Harrison et al., Detection of the Free Neutrino: A Confirmation; Science, 124:103, 1956

[36] Particle Physics Booklet 2016, extracted from the Review of Particle Physics, C. Patrignani et al. (Partice Data Group), Chin. Phys. C, 40, 100001 (2016)

[37] Ulrich F. Katz, Christian Spiering, High-Energy Neutrino Astrophysics: Status and Perspectives; arXiv:1111.0507 [astro-ph.HE], 2011/11/02

[38] Claudio Kopper, Performance Studies for the KM3NeT Neutrino Telescope, dissertation thesis, University of Erlangen-Nuremberg, Chair for Astroparticle Physics, 2010

[39] S. B. Samat, S. Green, A. H. Beddone, The 40K activity in one gram of potassium, Phys Med Biol. 1997 Feb;42(2):407-13, PMID: 9044422

[40] D. A. Webb, The Sodium and Potassium Content of Sea Water, Journal of Experimental Biology 1939 16:178-183

Closing Words

I have had a really great time at ECAP and I would like to summarily thank every one for the good working atmosphere, the fun off-duty activities and the interesting journeys we were allowed to take. I am fortunate to have had such a workplace that, for a while, was also half home to me. Sadly, all good things must come to an end. After I had had to leave university, it was difficult to find the necessary time and concentration to finish my thesis. In the end, I am pleased with what I was able to achieve, and extremely grateful that this part of my life journey is almost over, with just one more hurdle to take.

Special thanks go to

- Eichhörnchen, for greatly improving my life, and for motivating and supporting me during the long stretch to the finish,
- Cerberus for proofreading and occasionally kicking me in the butt,
- Griesgram for philosophising with me during our walks in the park,
- Kathrin for helping me through difficult times,
- Kampfkoloss for all the space battles we fought,
- Kerstin for running to gold with me, and for the sweets and the Burns,
- Susanne for helping me putting the pieces together,
- Lew for the fun we had in and on 333,
- Gerhart for valuable input and support,
- Club Mate and Red Bull, for providing such tasty sources of caffein.

Zuletzt möchte ich meiner Mutter und meinem Vater dafür danken, daß sie mir den Weg bereitet haben, durch die guten Gene, die Schulbildung, und die Unterstützung meiner technischen Interessen. Danke, daß Ihr mir das Studium ermöglicht habt. Bis auf die Sache mit den Genen gilt mein Dank auch Harald. Ihr seid klasse!